ACCURATE THREE-DIMENSIONAL CHARACTERIZATION OF THE NONLINEAR MATERIAL CONSTITUTIVE PROPERTIES FOR LAMINATED COMPOSITE MATERIALS

by

JULIA CLINE

Presented to the Faculty of the Graduate School of
The University of Texas at Arlington in Partial Fulfillment
of the Requirements
for the Degree of

DOCTOR OF PHILOSOPHY

THE UNIVERSITY OF TEXAS AT ARLINGTON
August 2015

Dedicated to my family,

especially Gido, Mom, Dad, Patti, Lindsay, and Rob.

Acknowledgements

I must extend my sincerest gratitude to my research advisor, Dr. Andrew Makeev for providing me with interesting and challenging projects to work on. In Dr. Makeev, I found a caring advisor who provided me with the support, encouragement, and reassurance needed to successfully complete my degree and more importantly, gain confidence in my abilities as an engineer. For that, I thank him.

I am grateful to Dr. Erian Armanios for all he has done to ensure that I complete this program, for being my mentor, and for the helpful advice he provided to me throughout this journey. I enjoyed the opportunity to work with Dr. Armanios as his graduate teaching assistant for solid mechanics for two semesters and thank him for the opportunity to refine my teaching skills and learn from him.

Thank you to my committee members, Dr. Kent Lawrence, Dr. Wen Chan, and Dr. Yuri Nikishkov for dedicating their time to be on my committee and review my dissertation. Thank you to everyone at AMSL: to Dr. Guillaume Seon for his invaluable contributions to the FEM analysis in this work and for teaching me all I know about ABAQUS; to Brian Shonkwiler for patiently teaching me so that I grew confident in my abilities as a experimentalist and to my friends: Katya, Sarvi, Bastiaan, and Md for their support and help. I will miss our daily lunches together.

This work is sponsored by the U.S. Army and Navy Vertical Lift Research Center of Excellence (VLRCOE). Such support is gratefully acknowledged. Thank you to Mr. Edward Lee at Bell Helicopter Textron and Mr. Steven Grohman at Triumph for manufacturing the test specimens. I gratefully acknowledge the financial support received from the Department of Mechanical and Aerospace Engineering and Office of Graduate Studies during my time at the University of Texas at Arlington.

Thank you to my family and friends for their insistence that I finish my degree; without their support, I would have undoubtedly left for the greener pastures of the working world by now. Thank you to Kay Haynes for professionally editing my thesis. Thank you to my sisters, Patti and Lindsay, for always being there. Thank you to my Gido for instilling in me the importance of education. Thank you to my fiancé, Rob, for supporting me unconditionally; for enduring 4 years living apart to allow me to complete my degree; for editing my dissertation and for encouraging me to be a more curious and thoughtful engineer.

Finally, there are not words to express the thanks I owe to my parents, Janice and Robin, for everything they have given me. I could not have done this without their love and support. Everything I do in life is to make them proud.

July 29, 2015

Abstract

ACCURATE THREE-DIMENSIONAL CHARACTERIZATION OF THE NONLINEAR MATERIAL CONSTITUTIVE PROPERTIES FOR COMPOSITE MATERIALS

Julia Elaine Cline, PhD

The University of Texas at Arlington, 2015

Supervising Professor: Andrew Makeev

Accurate and efficient full three-dimensional characterization of mechanical properties of composite materials, including stress-strain curves and strength characteristics, is essential for understanding complex deformation and failure mechanisms of composites and optimizing material qualification efforts. Non-contact, full-field deformation measurement techniques such as digital image correlation (DIC) allowing for assessment of all surface strain components on the entire specimen surface, enable simpler experimental setups and material specimen designs for more efficient and accurate material characterization.

This work presents a new method enabling simultaneous assessment of the shear stress-strain curves in all three principal material planes. The method uses a small rectangular plate torsion specimen. The method is relying on digital image correlation to capture deformation including the out-of-plane strain components and on finite element model (FEM)-based stress calculation. Material properties measured using short-beam shear tests are used as initial approximations of the material model in the FEM stress analysis.

Iterative FEM updating methods are used to assess the shear nonlinear stress-strain relationships of composite materials. A stress convergence method is developed to assess the interlaminar shear stress-strain curves by updating material properties until the stress state at the maximum point converges. Results for the interlaminar stress-strain curves are presented.

A full-field optimization method is developed to assess the nonlinear shear behavior in all principal material planes simultaneously based on the minimization of the error between FEM-predicted strains and DIC-measured strains. The use of the full-field data significantly reduces the number of FEM iterations compared to the stress convergence method and allows for the investigation of nonlinear material coupling among shear and tensile modes in the large strain regime. The short-beam shear method is expanded to construct an initial approximation based on full-field strain measurements.

Results include the in-plane and two interlaminar shear stress-strain curves simultaneously captured for IM7-carbon/8552-epoxy material system. Dependency of the in-plane and interlaminar shear response on axial and transverse stresses in the nonlinear regime is discussed.

Table of Contents

List of Illustrations

List of Tables

Chapter 1

Introduction

1.1 Motivation

Fiber-reinforced polymer (FRP) matrix composites are quickly replacing conventional materials for primary structural components in aerospace applications due to their high strength-to-weight ratio and their fatigue and corrosion resistance. Composite materials have additional complexity over traditional materials due to their inhomogeneity and anisotropic behavior. Current composite structures are engineered with a fail-safe approach leading to overly conservative designs. However, to achieve the greatest benefit of composites, a damage-tolerant approach should be used. This requires accurate and reliable structural analysis models that are able to predict the effect of manufacturing defects and accumulated damage on the material behavior; and determine the length of time the part can operate in the damaged state prior to repair. The structural analysis models need to capture the physics of material behavior, including complex deformation and failure mechanisms [1-3] to generate realistic failure predictions; therefore accurate three-dimensional material characterizations are required as the basis of the models.

Historically, standard practices for assessing material stress-strain constitutive relations have been based on resistance strain gage measurements [4]. A strain gage measures the average strain over the gage area; therefore, it is necessary to achieve a uniform strain distribution within the gage area, which imposes constraints on the specimen design. In-plane tensile, compressive and shear stress-strain curves for composite materials are measured using different specimen types and test configurations. The out-of-plane material properties needed for a structural analysis are not typically measured but are assumed based on the in-plane properties [4]. While the in-plane constitutive properties and strength characteristics are sometimes sufficient, certain critical applications such as composite helicopter rotor structures [5,6], where the through-the-thickness stress effects cannot be ignored, may require a full 3D material characterization to capture failure initiation.

Additionally, characterization of the nonlinear shear behavior up to failure is essential for accurate structural analysis and realistic failure predictions [7,8]. Interlaminar shear failure (delamination) is a common failure mode for laminated composites. The shear response is governed by the matrix, and polymeric matrices are highly nonlinear [9,10], most likely due to the formation of microcracks within the matrix [11]. This nonlinearity exists even at low strain values and varies depending on the material [12]. The lack of knowledge of interlaminar material behavior, including the nonlinear shear stress-strain relations, is a major hindrance to accurate fatigue life and failure predictions. It has been shown that failure predictions for thick composites with wavy plies are improved by improving the accuracy of material properties used during structural analysis [13]. Instead of making assumptions about the interlaminar behavior, it is worthwhile to develop methods capable of assessing the full three dimensional material response, including nonlinear behavior.

One major advancement to the field of material characterization is the development of digital image correlation (DIC), an accurate non-contact, full-field deformation measurement technique that uses a sequence of images to measure deformation on the surface of a specimen by tracking the motion of a random speckle pattern throughout its loading history [14]. Deformation measurements are obtained over the entire specimen surface, yielding a full-field assessment of all components of the strain in the plane being observed. Using DIC, large deformation and strain gradients can be measured, allowing for greater flexibility in the design of test configuration and specimen geometry. Particularly, DIC enables the development of methods that can measure multiple stress-strain relations from a single test specimen with multi-axial strain distributions. This would greatly increase the efficiency of material characterization through reduced time and material required for testing. The accuracy of DIC-based strain measurement has been demonstrated on many occasions. For example, Totry et al [15] show DIC strains matching conventional strain gage data in American Society for Testing and Materials (ASTM) D7078 v-notched rail shear testing of carbon/epoxy tape laminates. In Ref [5] conventional strain gage measurements were compared with DIC for ASTM D3039 tensile tests. DIC measurements (averaged to the strain gage scale) agreed with strain gage measurements, resulting in a 0.3% difference in measured tensile modulus and a 1% difference in Poisson's ratio.

In pursuit of a method to accurately and efficiently characterize the three dimensional material behavior of composite materials, Makeev et al [16] coupled a short-beam shear (SBS) test, modified from ASTM D2344 [17], with DIC strain measurement and developed a methodology capable of assessing multiple material properties from a single square cross-section, short-beam test specimen, based on closed-form analytical expressions derived from simple beam theory. Specimens can be manufactured so that the surface strain components for the in-plane (1-2) and interlaminar (1-3 and 2-3) principal material planes can be assessed as illustrated in Figure 1. The fiber direction is denoted as 1 (zero-degree), the in-plane transverse direction as 2 (90-degree), and the laminate thickness direction as 3 (the interlaminar principal material direction).

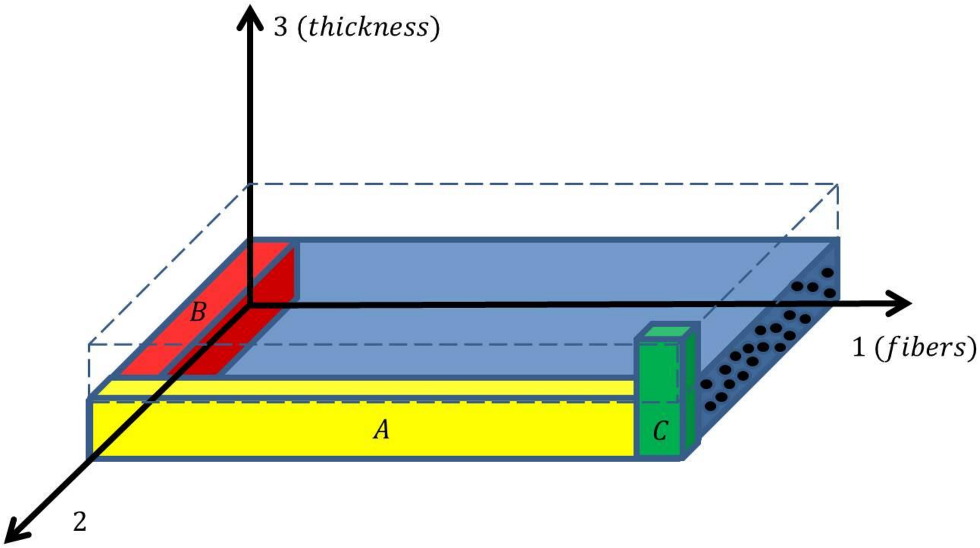

Figure 1. Material specimens are cut from a unidirectional panel in the zero-degree (A), 90-degree (B), and through-thickness (C) directions for assessment of in-plane and interlaminar properties.

Using the modified SBS method, Makeev et al were successful in capturing the axial behavior in all three principal material planes and the nonlinear shear behavior in the 1-2 and 1-3 principal material planes; however, the method cannot capture the nonlinear shear behavior for the

2-3 interlaminar principal material plane. Due to low transverse tensile strength of polymer matrix composites, the short-beam coupons machined in the 90-degree plane fail in tension before the shear stress-strain response becomes nonlinear [16,18]. It is conceivable that, until the specimens exhibit a shear failure, they will continue to exhibit a nonlinear shear response that needs to be characterized.

1.2 Objective and Approach

This work presents developments toward a method to accurately and efficiently characterize the full three-dimensional constitutive model for composite materials, including the 2-3 nonlinear stress-strain relations. A new methodology is developed based on a small-plate torsion test coupled with DIC that is capable of achieving significant nonlinearity in all three principal material planes simultaneously.

Small-plate torsion specimens are manufactured from a unidirectional panel, and load is applied to two diagonal corners of the small-plate specimen, while the opposite corners are simply supported (Figure 2). The specimen is subject to a multi-axial stress due to combined twisting and bending deformation, which yields large deformation on all three principal material planes. Three synchronized DIC systems are used to capture the deformation for the in-plane (1-2) and interlaminar (1-3 and 2-3) principal material planes simultaneously. This setup, as shown in Figure 2, provides all strain components necessary to characterize the nonlinear constitutive model.

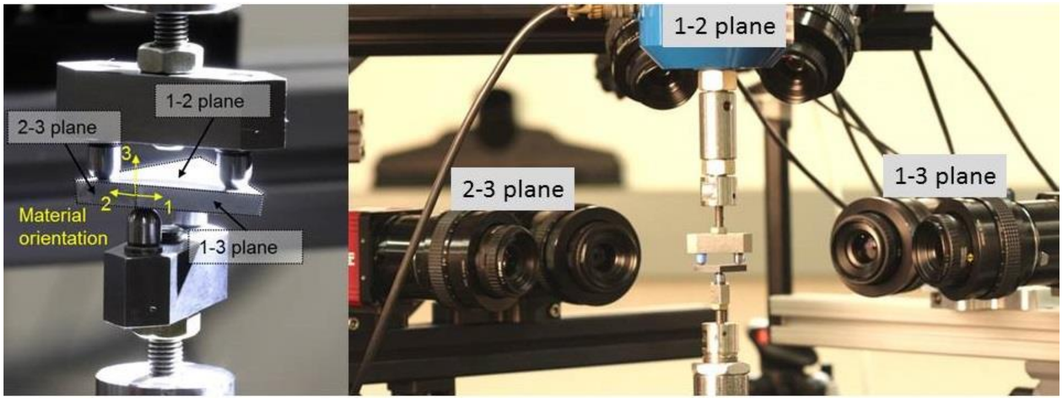

Figure 2. A small-plate torsion experimental setup with custom test fixture and three synchronized 16-megapixel stereo camera systems for simultaneous monitoring of the surface strain in all principal material planes.

Unlike the SBS coupon, the stress state for the small-plate torsion specimen is not geometric. No simple closed form solutions are available; therefore, a finite element model (FEM) will be used to calculate the stresses for the small-plate torsion specimen [19]. The dependency of the stresses on the material properties requires a good initial approximation of the material constitutive model, which can be obtained from the SBS test.

Iterative inverse methods which compare experimental data with FEM-predicted data to determine the optimal material properties best representing the material behavior are used to determine the constitutive model for IM7/8552 carbon/epoxy material system.

The outcome of this work is an iterative method for assessment of the shear nonlinear stress-strain relationships of composite materials using the full-field strain data generated in the small-plate torsion test specimens. Full-field strain measurements on the three principal material planes (surfaces) of the small-plate torsion specimen include large strain gradients and allow for an efficient simultaneous determination of both linear and nonlinear material parameters, using a limited number of DIC images generated during specimen-loading history. This test method allows for the confirmation of the assumption of transverse isotropy for unidirectional IM7/8552 and investigation of material couplings.

Chapter 2

Background

2.1 Short-Beam Shear (SBS) Method

2.1.1 Experimental Description

A short-beam shear test is defined in ASTM D2344 [17] to measure shear strength of fiber-reinforced composite materials. A prismatic rectangular specimen with recommended width-to-thickness ratio of two and span-to-thickness ratio of four to five is loaded in three-point bend until a shear failure occurs. A typical short-beam shear loading configuration is shown in Figure 3.

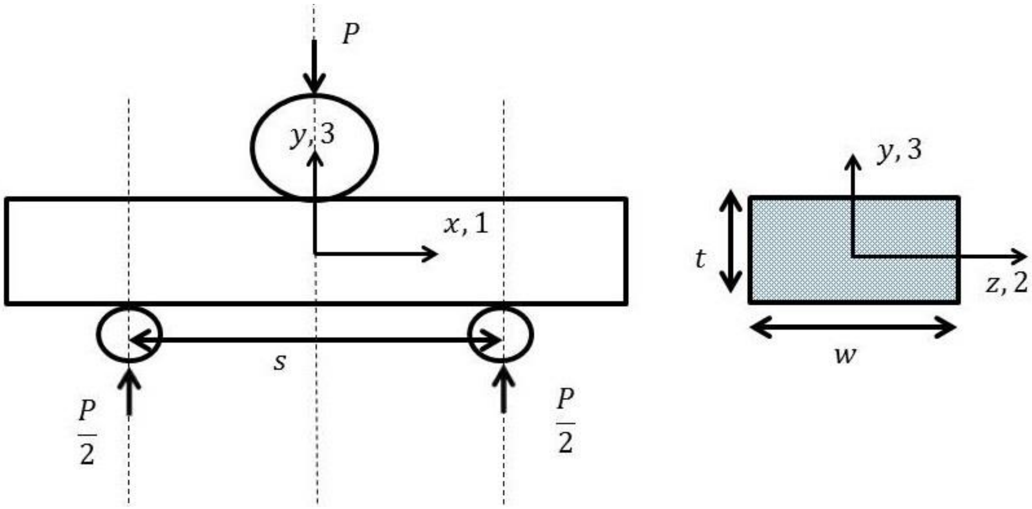

Figure 3. ASTM D2344 short-beam shear test configuration for a specimen loaded in the 1-3 principal material plane.

The specimen rests upon cylindrical supports of 0.125 in (3.175 mm) diameter and load is applied using a 0.25 in (6.35 mm) cylindrical loading nose. The dimensions of the supports and loading nose are recommended for use in Reference [17].

Makeev et al [16] introduced a modified short-beam method relying on DIC for measuring material shear stress-strain curves and tensile/compressive constitutive properties. Figure 4 shows a test setup, a specimen with applied speckle pattern, and an example of DIC-based strain contour plots. The reader is referred to Ref [14] for a more general description of the DIC technique; and to Refs [15,19] for more specific details pertinent to this work.

Material specimens are cut from a unidirectional panel in the zero-degree, 90-degree, and through-thickness material planes as shown in Figure 1. Zero-degree specimens are cut such that the fibers are parallel with the length and load is applied perpendicular to the fibers, and used to assess the 1-2 and 1-3 principal material planes. 90-degree specimens have their length perpendicular to the fiber direction and are used to assess the 2-3 principal material plane. Specimens can also be cut through-the-thickness from a thick panel and tested to assess interlaminar properties.

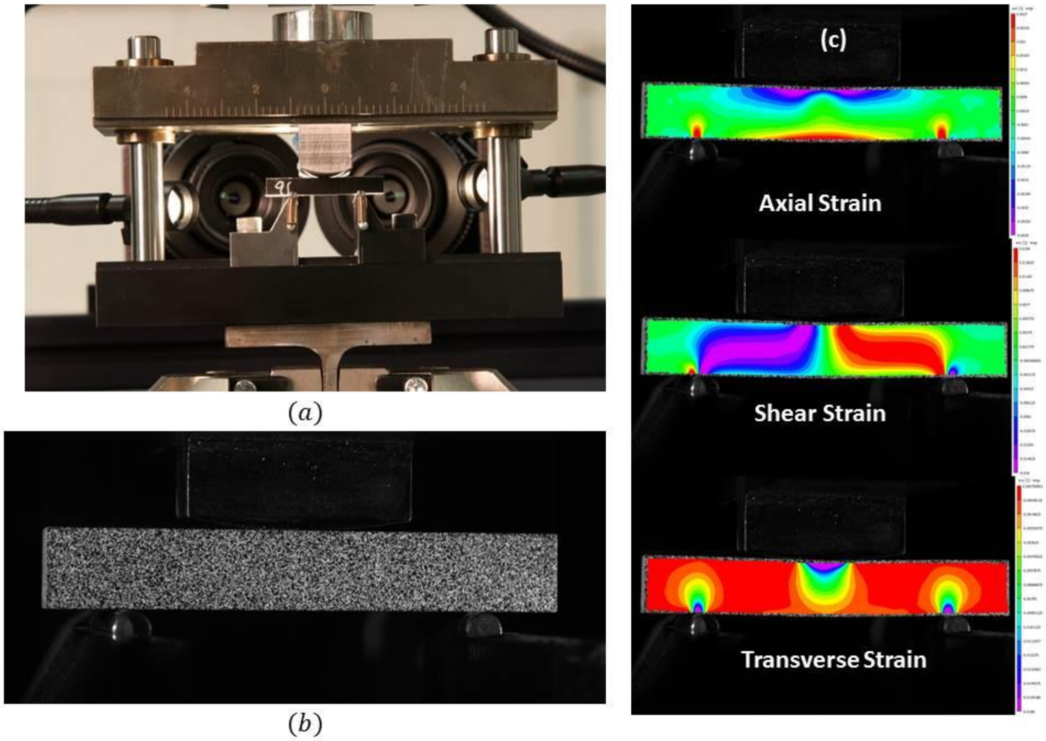

Figure 4. (a) Short-beam shear experimental setup, (b) Applied surface speckle pattern for DIC strain assessment, and (c) Typical axial, shear, and transverse strain distributions.

By applying monotonic quasi-static load in the 1-2 (in-plane), 1-3 (interlaminar), and 2-3 (interlaminar) principal material planes, all surface strain components (axial, transverse normal, and shear) can be assessed. Multiple material constitutive properties can be determined from a single specimen based on closed form analytical expressions, which will be described in the subsequent section.

The specimen geometry is modified from ASTM D3044 standard dimensions [17]. The short-beam coupons have a square cross-section to achieve a more uniform strain distribution through the width away from the support [16]. Shear failures of unidirectional short-beam specimens and tensile failures of 90-degree (2-3 plane) specimens and interlaminar tensile short-beam specimens allow for the assessment of matrix-dominated material shear and tensile strength [5, 16, 18, 20, 21].

ASTM D2344 [17] only recommends the short-beam shear method to measure shear strength because the high strain gradients prohibit the use of strain gages to capture deformation [4]. The use of non-contact, full-field DIC strain monitoring overcomes this challenge and enables the use of the SBS method for assessment of the strain state throughout the plane in which load is applied.

2.1.2 Failure of Short-Beam Shear Specimens

The failure mode of a composite short-beam specimen varies depending on the fiber direction, support length-to-thickness ratio and loading nose/support diameter. Figure 5 shows examples of representative failure modes. Current test parameters are chosen such that SBS specimens loaded in the 1-2 and 1-3 planes will fail in shear. 90-

degree specimens fail in tension in the middle of the specimen on the opposite side as the loading nose [16], due to low transverse tensile strength.

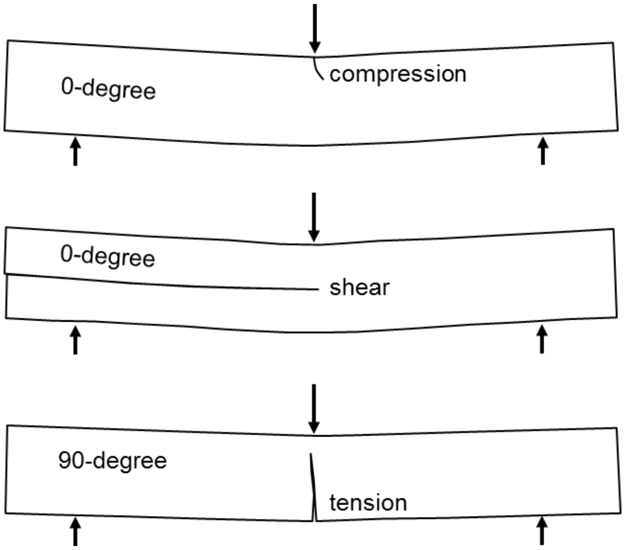

Figure 5. Failure of short-beam specimens.

Compression failure in a unidirectional short-beam specimen is currently an undesirable mode related to undersized loading nose causing excessive contact stress concentration [16, 20]. As the standard use of the short-beam shear test is to assess the interlaminar shear strength of a material, it is necessary that a shear failure be achieved. Though the focus of this work is the characterization of material constitutive properties, not strength, it is still worth noting previous efforts to avoid compressive failure in three-point bend tests. Wisnom [22] used varying loading nose sizes with rubber cushioning pads to avoid compressive failure and investigated the influence of differing span-to-thickness ratios on fracture stability. Xie and Adams [23, 24] found that as the span-to-thickness ratio is decreased, the maximum stress experienced in the material is less than the value of shear stress predicted by classical beam theory, which results in an overestimation of shear strength. Cui, Wisnom and Jones [25] found that compressive damage under the loading nose resulted in underestimated shear strength as the compressive damage reduces effective specimen thickness. In their finite element analysis, Cui and Wisnom [26] show that contact length increases with increased loading nose diameter, illustrating that the largest possible loading nose should always be chosen. They also performed a comprehensive study on the effect of specimen size in Reference [27]. Note, however, that none of these efforts were aimed at measuring material stress-strain properties.

For the custom SBS tests, Makeev et al [16] increased the upper support (loading nose) diameter from the ASTM D2344 [17] recommended 0.25 in (6.35 mm) to 4.0 in (10.16 cm) for carbon/epoxy specimens to reduce compressive damage under the loading nose before shear failure. The standard lower support diameter of 0.125 in (3.175 mm) is used [17] and can be increased to 0.25 in (6.35 mm) if compression failure at the lower supports becomes an issue. Figure 6 shows zero- and 90-degree specimen failures in the designed modes.

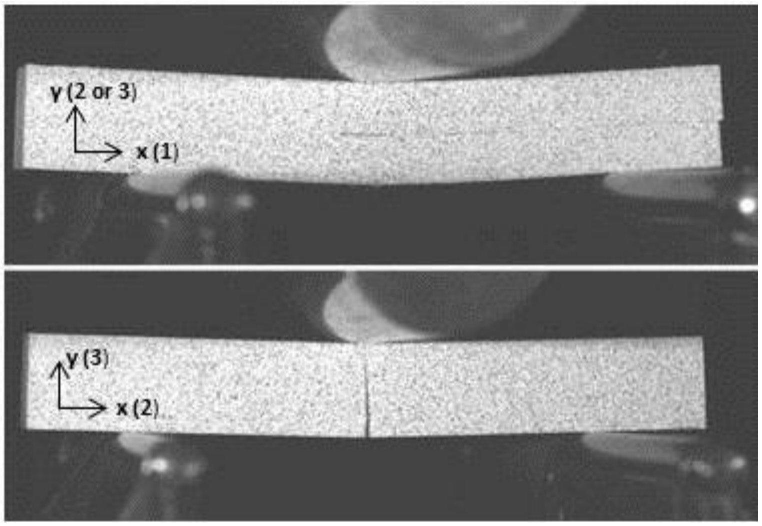

Figure 6. Shear failure of a unidirectional short-beam specimen cut in the fiber direction (zero-degree); and tensile failure of another short-beam specimen cut in the 90-degree direction and loaded in the 2-3 plane.

90-degree specimens fail prematurely in tension before the 2-3 shear stress-strain response becomes nonlinear [16], limiting the SBS method for the assessment of the 2-3 shear stress-strain response up to failure. This can be overcome by adding a significant number of zero-degree plies as reinforcement; however, this causes significant residual stresses during the curing process. Previous attempts to use ASTM D5379 [28] v-notched beam method to measure 2-3 shear stress-strain relations using specimens cut in the 90-degree principal material plane also failed to achieve significant shear nonlinearity before failure. A tensile failure occurred in the vicinity of the v-notches at 2-3 shear strain slightly exceeding 1% [12]. Thus, using the SBS method, only the linear shear stress-strain relation for the 2-3 plane can be observed.

2.1.3 Closed-Form Approximations for the Axial and Shear Material Properties

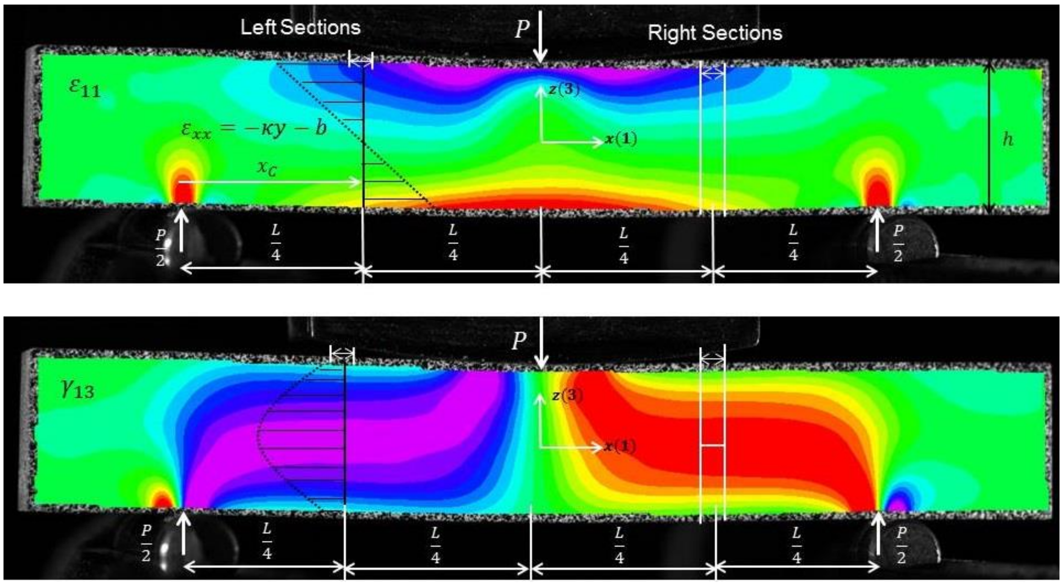

Figure 7. Typical axial and shear strain distributions from DIC measurement. The linear distribution of the axial strain is shown in (a) and in (b) the maximum shear strain occurs at the neutral plane. Regions used for strain evaluation are shown.

Observations from DIC-based strain distributions in the short-beam coupons enable a rigorous derivation of simple geometric (material independent) closed-form approximations for the axial normal and shear stresses [16].

As shown in Figure 7, linear axial strain distributions through the thickness halfway between the loading nose and lower supports agree with classical beam theory and allow the formulation of the axial tensile and compressive modulus values [16] as shown in equation (1)

$$E_{T,C} = \frac{M}{\kappa \frac{wh^3}{12}(1 \mp a)^2}, \quad a = \frac{2}{h}\frac{b}{\kappa} \qquad 1$$

where $M = \frac{PL}{8}$; P is the applied load, and w, h are the width and thickness, respectively. The constants, κ and b, are the slope and intercept of the linear axial strain distribution, $\varepsilon_{xx} = -\kappa y - b$ through the specimen thickness $\left(-\frac{h}{2} \leq y \leq \frac{h}{2}\right)$ away from the supports. Note that the above formulation is not limited to a single cross-section, but can be normalized over a 2 mm long gage area as the material properties do not depend on the x location. The bending moment M, slope, κ, and intercept b of the linear axial strain approximation are all linear with respect to x [16].

The equationss for the linear axial strain distribution through the thickness over a gage length, typically 0.08 in (2.0 mm), can be generalized as

$$\varepsilon_{xx}\frac{x_C}{x} = -\kappa_C y - b_C \qquad 2$$

where

$$x_C = \frac{L}{4}, \quad \kappa_C = \frac{\kappa}{x}x_C, \quad b_C = \frac{b}{x}x_C,$$

It follows then that the expression for the tensile and compressive modulus would be

$$E_{T,C} = \frac{M_C}{\kappa_C\frac{wh^3}{12}(1\mp a)^2}, \quad a = \frac{2}{h}\frac{b_C}{\kappa_C} \qquad 3$$

where $M_C = \frac{Px_C}{2}$. κ_C and b_C then become the slope and intercept of the normalized axial-strain distribution, $\varepsilon_{xx}\frac{x_C}{x}$, away from the loading nose and support regions.

For assessment of the shear properties, it has been shown in Reference [16] that the maximum shear stress distribution midway between the support and loading nose is given by

$$\tau_{ij}{}^{max} = \frac{3}{4}\frac{P}{A},\ A = wh. \tag{4}$$

This is the same expression used in ASTM D2344 [17] to evaluate short-beam shear strength. An area of shear develops between the loading nose and lower supports with the maximum shear strain occurring at the neutral plane as shown in Figure 7, close to the mid-plane of the SBS specimen. In the DIC software Vic-3D [29], a 2-mm-long line average along the neutral plane, at the midpoint between the loading nose and lower support is used to extract the average maximum shear strain per load. A line average is used to reduce the influence of noise at low strain levels. The Ramberg-Osgood equation [30]

$$\gamma_{ij} = \frac{\tau_{ij}}{G_{ij}} + \left(\frac{\tau_{ij}}{K_{ij}}\right)^{\frac{1}{n_{ij}}} \tag{5}$$

is used to approximate the nonlinear shear response for the $i, j = 1{,}2\ and\ 1{,}3$ planes. In equation (5), G_{ij} is the linear shear modulus, and K_{ij} and n_{ij} are the secant-intercept modulus and exponent, respectively. A summary of the loading configurations and corresponding material properties calculated from the measured strain data and the above equations is shown in Figure 8.

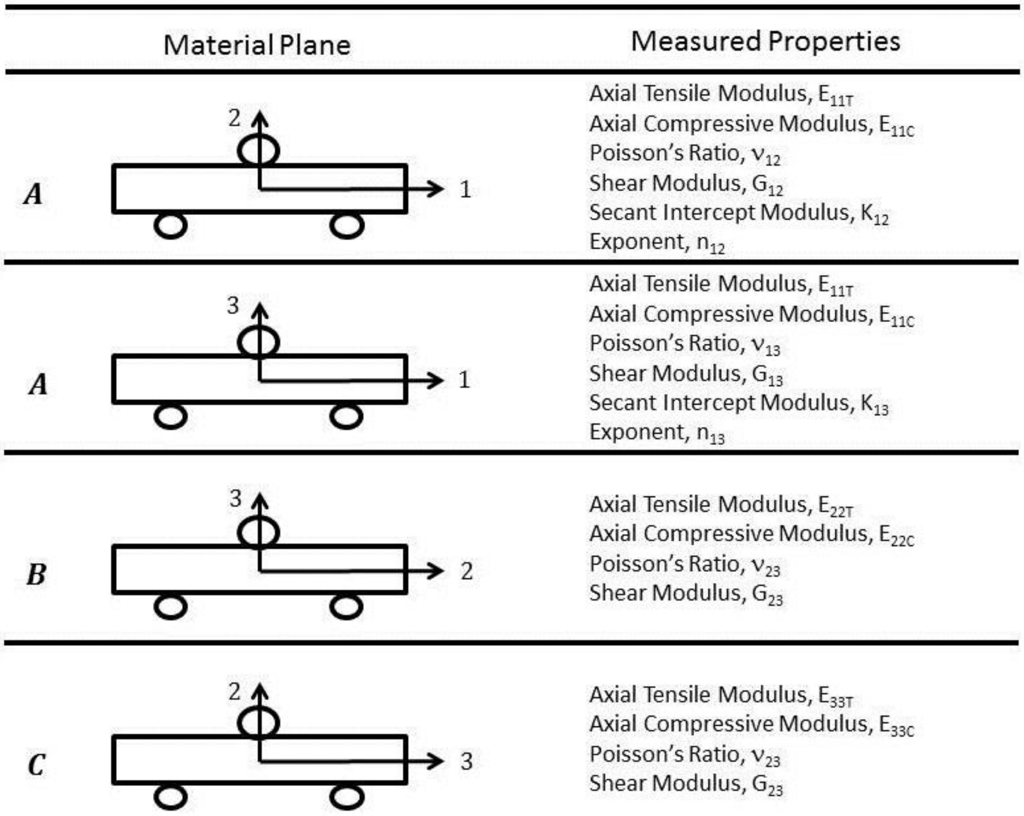

Material Plane	Measured Properties
A	Axial Tensile Modulus, E_{11T} Axial Compressive Modulus, E_{11C} Poisson's Ratio, ν_{12} Shear Modulus, G_{12} Secant Intercept Modulus, K_{12} Exponent, n_{12}
A	Axial Tensile Modulus, E_{11T} Axial Compressive Modulus, E_{11C} Poisson's Ratio, ν_{13} Shear Modulus, G_{13} Secant Intercept Modulus, K_{13} Exponent, n_{13}
B	Axial Tensile Modulus, E_{22T} Axial Compressive Modulus, E_{22C} Poisson's Ratio, ν_{23} Shear Modulus, G_{23}
C	Axial Tensile Modulus, E_{33T} Axial Compressive Modulus, E_{33C} Poisson's Ratio, ν_{23} Shear Modulus, G_{23}

Figure 8. Measured material properties based on loading configuration for SBS specimens (1-fiber direction, 2-transverse direction, and 3-thickness direction).

Results for the 1-2 in-plane and 1-3 interlaminar shear stress-strain curve, 2-3 interlaminar shear modulus, as well as zero-degree and 90-degree tensile/compressive moduli have been published in Ref [16]; and results for the interlaminar tensile strength and modulus material properties have been presented in Refs. [18,21]. Note that only small regions of the full-field strain distribution are used in the formulation of material constitutive relations.

This method was extended to assess the out-of-plane interlaminar tensile modulus (ILT) [18,21]. Specimens were cut from a thick unidirectional panel and loaded in the 2-3 principal material plane as shown in Figure 8. Analysis of the DIC surface strains was performed as outlined previously. A comparison of the ILT SBS method and ASTM D 6415 curved beam results showed a less than 1% difference in ILT modulus [18]. ILT SBS specimens are far simpler to manufacture than curved-beam specimens, require less material, and are not as prone to manufacturing defects such as porosity.

Carbon/epoxy composites exhibiting high shear strength in a highly nonlinear region of the corresponding shear stress-strain curve, resulted in up to 15% error in shear strength calculation; and therefore required FEM-based calculation of shear stresses [31]. An iterative FEM-based process was developed for calculating stresses [31] and applied to practical glass/epoxy and carbon/epoxy tape material systems. The FEM analysis showed that the result of the nonlinear shear behavior was to reduce the maximum shear stress achieved in regions away from the loading nose and supports – i.e. the predicted value of maximum shear stress from classical beam theory is never fully reached [31]. At low stress/strain levels, the difference between the stresses from the closed form approximation and FEM are negligible. This difference, however, becomes more pronounced as the nonlinearity in the shear stress-strain response becomes significant. Stress analysis confirmed that FEM-based correction of shear stress in short-beam coupons was still geometric, and allowed for closed-form approximations [20,32]. A bilinear model is used to correct the closed form approximation and ensure the difference between shear stresses is less than 5% for all load levels [20] for the typical span-to-thickness ratio of 5.

$$\tau_{ij} = \begin{cases} \frac{3}{4}\frac{P}{A} & \frac{3}{4}\frac{P}{A} \leq \tau_0 = 6.8\ ksi \\ 0.8\left(\frac{3}{4}\frac{P}{A} - \tau_0\right) + \tau_0 & \frac{3}{4}\frac{P}{A} > \tau_0 = 6.8\ ksi \end{cases} \qquad 6$$

where i,j =1-2 or 1-3. No correction is expected for the 2-3 plane shear stress.

In an effort to improve the accuracy of the shear stress analytical model, Carpentier et al [33] looked at the variation of span-to-thickness ratio with respect to accuracy of the closed-form shear stress approximation given by simple beam theory. It was found that for specimens with a span-to-thickness ratio of 10, the closed-form stress solution was within 5% of the FEM-based stress calculation, however, undesirable compression failures occurred for a span-to-thickness ratio greater than 6 [33]. The bilinear model was generalized for various span-to-thickness ratios in Ref [33].

$$\tau_{ij} = \begin{cases} \frac{3}{4}\frac{P}{A} & \frac{3}{4}\frac{P}{A} \leq \tau_0 = 6.8\ ksi \\ \left((0.03(s/t) + 0.6)\left(\frac{3}{4}\frac{P}{A} - \tau_0\right)\right) + \tau_0 & \frac{3}{4}\frac{P}{A} > \tau_0 = 6.8\ ksi \end{cases}. \qquad 7$$

FEM-based stress analysis confirms that the stress distributions in short-beam specimens are insensitive to material properties [19,31,32], meaning that the short-beam method provides an excellent first approximation of the material constitutive relations. The FEM-calculated stresses will exhibit an accurate trend throughout the coupon, and is insensitive to the initial guess provided to the FEM. The surface strain components, measured using DIC, can be coupled with the calculated surface stresses (three out of six stress components are zero at free surfaces) to uniquely determine the material properties relating three surface stresses and strains in the plane of loading.

Despite the fact that deformation measurements are collected for the entire specimen surface up to failure, only small regions of the full field, corresponding to the location of maximum shear stress and strain midway between the loading nose and supports, have been used to assess the 3D material properties. Most of the strain data collected was ignored.

2.1.4 Assessment of the 2-3 Plane Nonlinear Interlaminar Properties

Unfortunately, the SBS method fails to capture the nonlinear shear stress-strain relations in the 2-3 interlaminar principal material plane [16] due to premature tensile failure, as discussed in Section 2.1.2 The 1-3 interlaminar shear strength of practical glass/epoxy and carbon/epoxy tape composites corresponds to at least 3% engineering shear strain [20] and similar values are expected for the 2-3 principal material plane.

2.2 Small-Plate Torsion Test Method

Historically, small-plate torsion (plate-twist) tesst of small rectangular specimens have been used to measure in-plane shear response as a uniform shear stress distribution can be achieved over a significant region of the specimen without difficulty. The method consists of applying load to diagonal corners of a flat-plate specimen while the other two corners are simply supported as shown in Figure 9. The initially flat-plate twists into a saddle shape with large deflections possible at low loads. A significant region of the specimen is in a shear-dominated stress state. Principal directions of the material are aligned normal to the specimen edges.

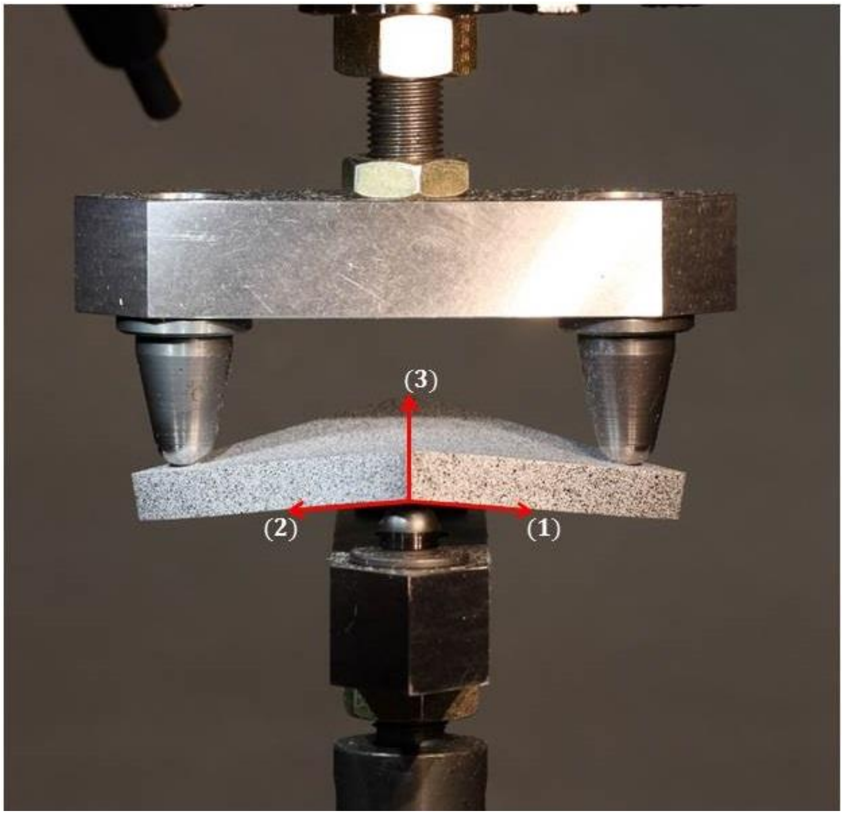

Figure 9. Generic loading configuration for a flat-plate twist test.

The plate twist test is a standard method (ASTM D3044 [34] and ISO 15310 [35]) for assessing in-plane shear properties of wood and wood-based panels [36] and has also been applied to fiber-reinforced polymer (FRP) composites [37-41] and more recently, sandwich composite laminates [42]. The plate-twist test is also used to identify mode III fracture toughness [43].

The focus of the previous work has been to determine the in-plane shear response using measured load-displacement (or torque-twist) data combined with analytical expressions. Deflections of the loaded corners are typically measured with respect to the center of the specimen and the shear modulus is determined from the load-deflection data.

The first published work with respect to a flat-plate twist specimen to be used to determine the in-plane shear modulus of FRP composites was by Hennessey et al [38] using the angular deflection as a function of applied torque for thin rectangular plates. Later, Tsai [37] used the plate-twist method with unidirectional plates to reliably determine elastic properties for a glass/epoxy composite. Most recently, Morais *et al.* [41] identified the flat-plate torsion test as satisfying the criteria for an ideal test to determine the in-plane, 1-2 nonlinear shear stress strain curve for a carbon/epoxy composite using a load-displacement curve. They observed that the in-plane shear stress-strain curves obtained showed significant nonlinearity, but the work is only focused on characterizing the linear-shear modulus. They note that the unidirectional flat-plate torsion test is only considered appropriate for measuring in-plane shear modulus, G_{12}. To date, the small-plate torsion test has not been used to measure the interlaminar material behavior. Also, none of the previous work with small-plate torsion specimens utilized full-field strain measurement.

A literature review reveals that difficulty arises in placing the loading/support points precisely at the corners of the small-plate torsion specimen, which affects experimental results [37,38]. Thus, a variety of configurations are proposed for loading/support application. Tsai [37] left three of four corners fixed and applied load on the free corner, which allowed the use of crosshead displacement in material property calculations. Sims et al [39] proposed a correction factor to traditional relations if alternate loading points were used. This work led to the development of ISO 15310 [35], which moved load/support points inward toward the center of the plate. The loading points are placed at a span equal to 0.95 of the diagonal length. ASTM D3044 [34] requires the application of metal plates over the corners with point loading and support at the corners. Farshad [43] and Gommers [44] simplified the experimental setup in ISO 15310 by introducing cylindrical rollers for load application instead of the traditional hemispherical loading points. Avilies [42] found that the use of flat circular cross-section pins caused less indentation than hemispherical pins.

In this work, the initial test configuration is developed based on the fixture and specimen geometry used by Morais' *et al* [41].

2.3 Inverse Methods to Determine Material Properties based on Full-Field Measurements

Determining the constitutive relationship for a composite material is an inverse problem because the relationship between applied stress and resulting strain is not known. Where a direct problem would compute displacement/strain and stresses from known load, geometry, and material constitutive properties; an inverse method determines the material properties based on geometry, load, and experimentally measured displacements/strains. Closed-form, analytical solutions only exist for a few cases, so numerical methods are commonly used.

The basic principle of the inverse method is to minimize, in a least squares sense, the discrepancy between experimentally measured quantities and numerical quantities computed from a numerical analysis (such as an FE model) by updating the parameters of the constitutive model [45]. Generally, gradient-based optimization methods are used for the minimization problem. A cost function for the minimization is defined based on the difference to be minimized [45]. The condition to minimize the cost function is that its partial derivatives with respect to the material properties are zero. Since there is no a priori explicit relationship between the numerical quantities and the experimentally measured quantities, the minimization cannot be solved analytically. Instead, iterative procedures are required. Convergence of the model can be defined based on the relative change in parameter update, stress state, or cost function, whichever is most appropriate. This method is commonly referred to as Finite Element Method Updating (FEMU) [46]. Use of the FEMU approach does not require full-field measurements. For example, the iterative stress update procedure used in Reference [31], uses data from only the maximum stress/strain point to determine the material constitutive properties for a carbon/epoxy composite. Convergence is achieved when the relative change in the shear stress is below a small tolerance [31].

A topical review of inverse problems in linear elasticity is presented in Reference [45], and more recently, an extensive overview of full-field methods for identification of material properties is given in Reference [47]. Among strategies developed to solve the inverse problem of determining material constitutive properties using full-field information, FEMU has been the most common approach and the virtual fields method (VFM) the most recent alternative.

The VFM method relies on the principle of virtual work. Virtual fields are chosen such that the material parameters are the only unknowns, resulting in a system of equations that can be solved directly for the material parameters. The advantage of the VFM is that no costly iterative FEMs are required; however, the choice of virtual fields is based on an assumed constitutive model.

Most of the existing work using inverse methods and full-field measurements for material characterization of composites has been focused on the identification of elastic properties such as orthotropic material constants or rigidities of laminated plates [48-50]. Full-field measurements coupled with VFM were used in Reference [51] to determine the nonlinear shear behavior of a glass-epoxy composite based on double V-notched shear tests. However, only in-plane shear properties were identified and some restrictions inherent to the VFM approach, such as the complexity in choosing suitable virtual fields for arbitrary specimen configuration and test setup, could be mentioned.

Avril and Pierron [52] performed a statistical comparison of FEMU to VFM to evaluate the robustness of the FEMU method, and found that the two methods are equivalent when the appropriate virtual fields are chosen. Grediac [46] reviews the use of full-field measurement techniques with FEMU and VFM, including notable advantages and disadvantages of each method.

Chapter 3

Determination of the Interlaminar Shear Properties Using a Stress Update Method

In this chapter, an inverse method based on the maximum shear stress/strain relationship is developed and applied to find the interlaminar shear stress-strain curves for an IM7-carbon/8552-epoxy composite material system based on the small-plate torsion test explained in Section 2.2.

3.1 Experimental Description

To enable simultaneous assessment of the interlaminar shear stress-strain curves in the 2-3 and 1-3 principal material planes in this work, 11 small rectangular specimens were machined from a 36-ply 0.25 in (6.35 mm) thick IM7/8552 carbon/epoxy unidirectional tape panel cured at 350 degrees Fahrenheit (F) per prepreg manufacturer's specifications [53]. The specimen length, L, and width, w, are 2.5 in (63.5 mm). Note that the specimen thickness was chosen to be the same as the typical 0.25 in (6.35 mm) thickness of short-beam coupons machined from the same unidirectional panel. Figure 9 shows the small-plate torsion experiment setup and loading conditions.

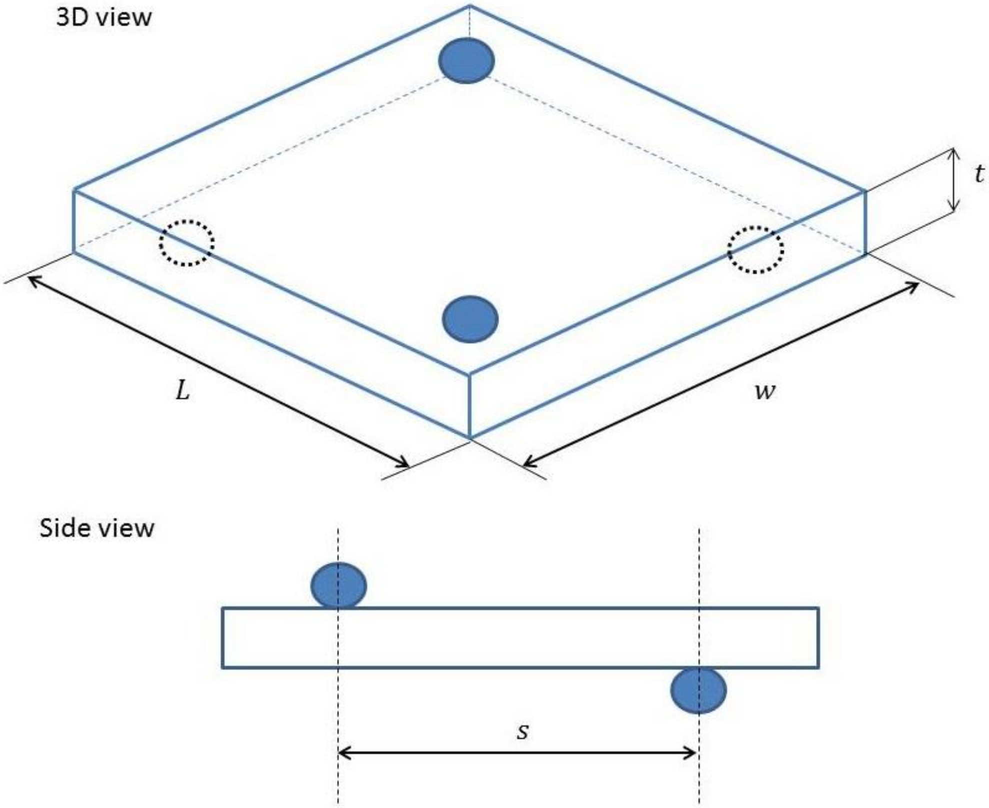

Figure 10. Schematic diagram of the small-plate torsion specimen geometry with $L = w = 2.5\ in,\ \ t = 0.25\ in,\ \ s = 2.0\ in$.

The small-plate specimens were placed in a custom test fixture with 0.375 in (9.525 mm) diameter hemispherical supports; and loaded in a servo-hydraulic load frame at a constant 0.05 in/min (1.27 mm/min) crosshead displacement rate until failure. The support length, s, is 2.0 in (5.08 cm) as shown in Figure 10.

The cross beams of the fixture are oriented at 90 degrees to one another using an alignment tool as shown in Figure 11. The locking washers at the base of the fixture are left loose in the test frame until all loading noses and supports are aligned in the jig. They are then tightened to ensure the fixture stays aligned during testing.

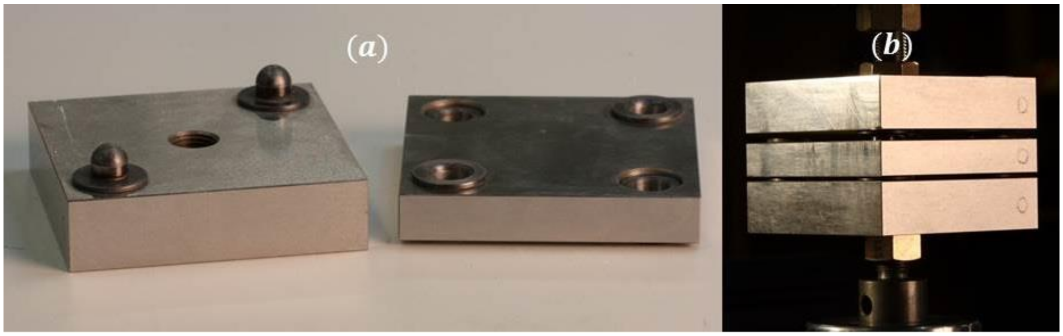

Figure 11. Torsion alignment jig pictured with (a) the top half of the torsion fixture and (b) installed in the fixture.

The tests were conducted at 72 degrees F room-temperature, ambient conditions. All specimens failed away from support locations as shown in Figure 12.

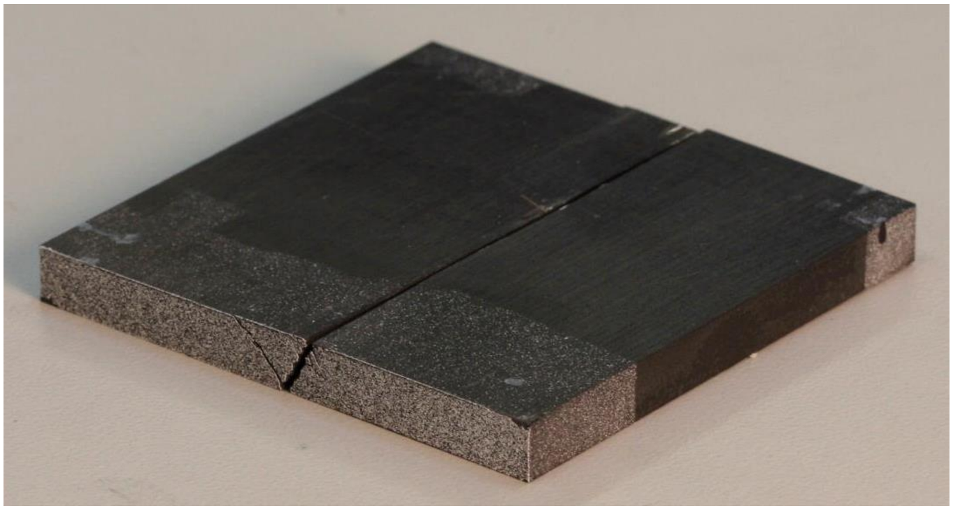

Figure 12. Typical failure of a unidirectional small-plate torsion specimen.

DIC was used to assess the interlaminar strain components. One 16-megapixel stereo camera system monitored interlaminar strain in the 2-3 principal material plane for 5 out of 11 unidirectional small-plate torsion specimens; and two 16-megapixel stereo camera systems monitored the interlaminar strain in both 2-3 and 1-3 principal material planes for the remaining 6 specimens. All coupons exhibited similar behavior. Figure 13 shows a setup for simultaneously monitoring surface strain in the 2-3 and 1-3 principal material planes.

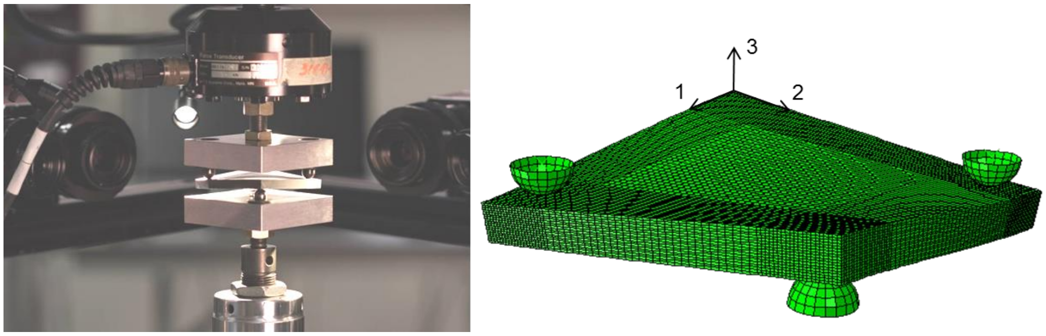

Figure 13. A setup for simultaneously monitoring surface strain in the 2-3 and 1-3 principal material planes, using two stereo camera systems; and a three-dimensional finite element model of a unidirectional small-plate torsion specimen.

Figure 14 shows typical engineering shear strain components measured before failure using the DIC technique and generated with the VIC-3D software [29]. The DIC strain analysis used a subset (data point) size of 45×45 pixels, corresponding to approximately 0.0007 in^2 (0.47 mm^2) for these particular tests. Data was obtained on 9 pixel centers, resulting in approximately 20,000 data points per load case.

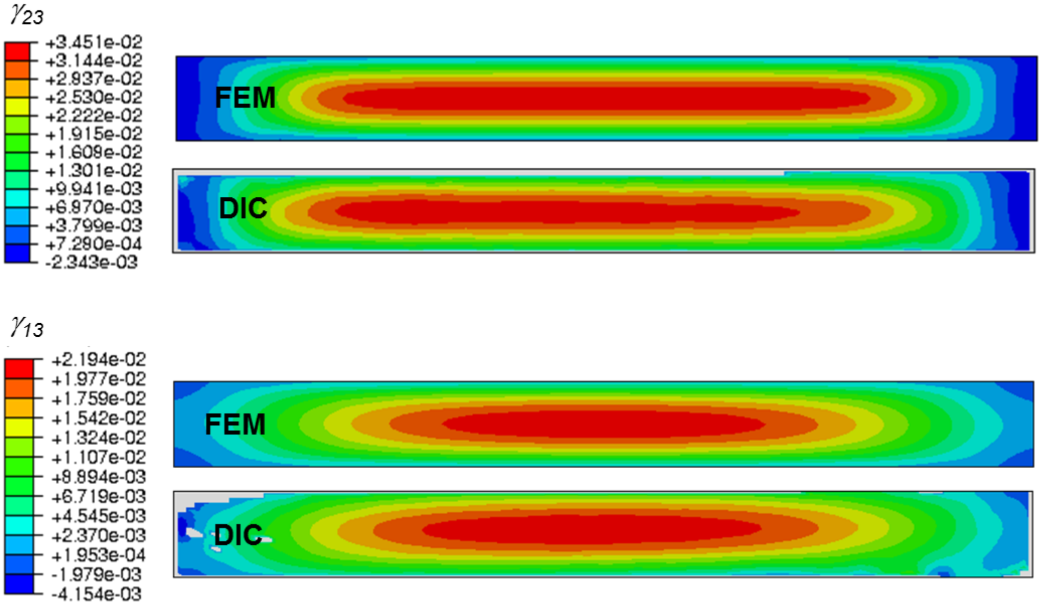

Figure 14. Comparison of measured interlaminar strain distribution (DIC) and predicted interlaminar strain distribution (FEM) in the 2-3 and 1-3 principal material planes of a unidirectional carbon/epoxy small-plate torsion specimen at 995 lb (95% failure) load.

A region of uniform maximum shear strain develops at the mid-surface of the specimen away from the supports, as illustrated in Figure 14 for the 2-3 and 1-3 material planes. Strain values along a small line measuring 0.5 in (12.7 mm) along the mid-surface axis are used in this work to average the maximum shear strain for each load level, similar to the procedure used for extracting the maximum shear strains in short-beam specimens [16, 20, 31]. Maximum interlaminar shear strains greater than 3% are observed in the 2-3 principal material plane before failure. Shear strains greater than 2% are also obtained in the 1-3 principal material plane, which allows for assessment of the nonlinear interlaminar shear properties in that plane and verification of the method by comparison with short-beam test results. The axial and transverse longitudinal strains are an order of magnitude lower than the corresponding maximum shear strain in this region.

3.2 Finite Element Stress Analysis

A three-dimensional finite element model (FEM) was developed for stress calculation in small-plate torsion specimens, using commercial finite element modeling software ABAQUS [54]. Figure 13 shows a typical finite element mesh including approximately 95,000 first-order three-dimensional incompatible mode solid elements (C3D8I). Incompatible modes elements are well-suited for the torsion/bending problem considered in this work because the additional incompatible deformation modes, added to the element formulation, eliminate parasitic shear stresses and stiffening usually found in the bending response of regular first-order elements [54]. The supports are assumed to be rigid and are modeled as rigid analytical spherical surfaces. Frictionless contact conditions are assigned between the specimen surfaces and the support points. A surface-to-surface contact formulation is selected in ABAQUS in order to avoid local indentation stresses at contact points. The FEM accounts for geometric nonlinearity; and the material shear nonlinearity for IM7/8552 carbon/epoxy is implemented via a user subroutine UMAT. Nonlinear shear stress-strain relations are characterized by the log-linear Ramberg-Osgood equation.

Initial guesses of the nonlinear shear stress-strain relations are provided for all the three principal material planes in Table 1. The nonlinear material properties generated based on short-beam tests [31] are used to define shear material behavior in the 1-2 and 1-3 principal material planes.

Table 1. Initial Approximation of the Material Constitutive Properties for FEM Analysis

Shear Properties

$$G_{12} = G_{13} = 0.737\ Msi\ (5.08\ GPa)$$

$$K_{12} = K_{13} = 36.1\ ksi\ (0.249\ GPa)$$

$$n_{12} = n_{13} = 0.248$$

Axial Properties

$$E_{11} = 22.7\ Msi\ (157\ GPa)$$

$$E_{22} = E_{33} = 1.3\ Msi\ (8.96\ GPa)$$

$$\nu_{12} = \nu_{13} = 0.32$$

$$\nu_{23} = 0.50$$

Transverse isotropy has been assumed for the initial approximation of the shear modulus in the 2-3 principal material plane

$$G_{23} = \frac{E_{22}}{2(1+\nu_{23})} = 0.433\ Msi\ (2.99\ GPa)., \qquad 8$$

The initial approximations for the 2-3 plane nonlinear material shear properties in this work are shown in Table 2. In the first approximation, denoted as (A), the secant-intercept modulus K_{13} value from the short-beam method [31] has been scaled using the G_{23}/G_{13} shear modulus ratio. In the second approximation, denoted as (B), K_{23} is assumed to be equal to K_{13}. In both cases, the exponent is assumed to be $n_{23} = 0.248$.

Table 2. Initial Approximations for the Secant-Intercept Modulus K_{23}

A	$K_{23} = K_{13}\frac{G_{23}}{G_{13}} = 21.3\ ksi\ (1.47\ GPa)$ $n_{23} = 0.248$
B	$K_{23} = K_{13} = 36.1\ ksi\ (0.249\ GPa)$ $n_{23} = 0.248$

A mesh refinement sensitivity study was performed to ensure that proper stress convergence is achieved. At least 16 elements in the thickness direction were required to ensure convergence of the maximum shear stress and correctly capture strong stress gradient. Subsequent mesh refinements in the contact region under supports were required. The final converged finite element model had approximately 1,450,000 degrees of freedom.

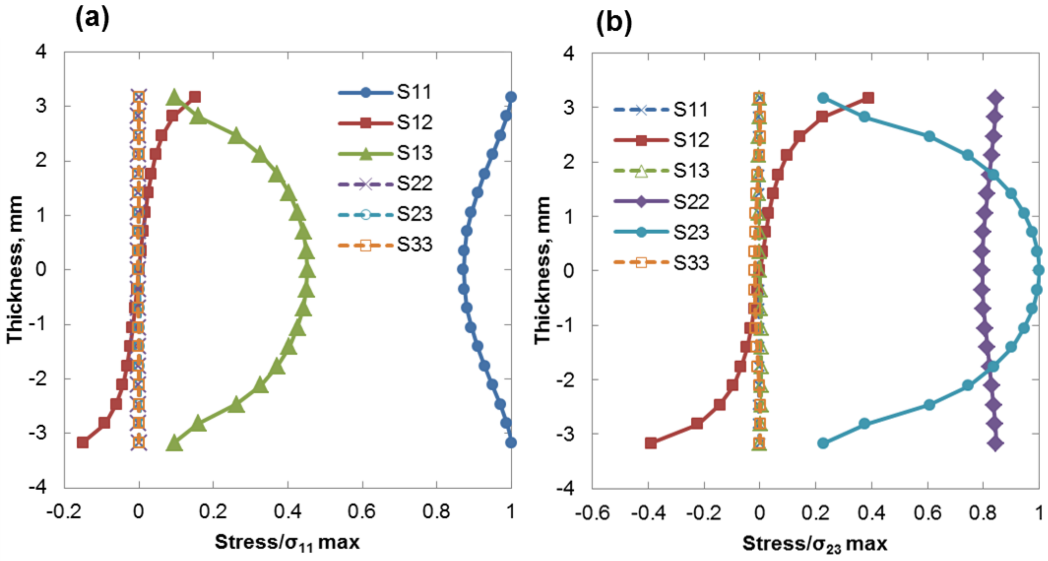

Figure 15. Typical normalized through-the-thickness stress distributions for a specimen at the cross-section center in (a) the 1-3 material surface plane and, (b) the 2-3 material surface plane at 95% failure load.

A typical through-the-thickness distribution of stresses in the center of the specimen cross-sections corresponding to the 1-3 and 2-3 principal material planes is presented in Figure 15 at 95% failure load. The stress components in the 1-3 and 2-3 material planes are normalized by the maximum values of σ_{11} and σ_{23}, respectively.

A sensitivity analysis showed that shear stresses in the small-plate torsion specimens are not sensitive to Young's moduli and Poisson's ratios. The results of the sensitivity analysis are summarized in Table 3, which lists relative changes in shear stresses corresponding to a 20% reduction of each elastic material constant. Results are presented for a typical 35% failure load (360 lbs) corresponding to a 0.6% γ_{13} interlaminar shear strain and 1% γ_{23} interlaminar shear strain representing linear response (a); and for a typical 95% failure load (995 lbs) corresponding to 2% γ_{13} interlaminar shear strain and 3% γ_{23} interlaminar shear strain representing highly nonlinear stress-strain behavior (b).

Table 3. Sensitivity of Maximum Interlaminar Shear Stresses to a 20% Reduction of Values of Elastic Properties in the Linear Regime (a) and Nonlinear Regime (b).

(a)

Material Constant (Δ = - 20%)	$\Delta\sigma_{23}$	$\Delta\sigma_{13}$
E_{11}	0.03%	0.05%
E_{22}	0.56%	-2.38%
E_{33}	-0.05%	-0.11%
v_{12}	-0.03%	-0.02%
v_{13}	0.00%	0.00%
v_{23}	0.00%	-0.09%
G_{12}	7.79%	9.95%
G_{13}	0.10%	-7.52%
G_{23}	-8.43%	0.11%

(b)

Material Constant (Δ = - 20%)	$\Delta\sigma_{23}$	$\Delta\sigma_{13}$
E_{11}	-0.04%	0.17%
E_{22}	0.78%	-1.20%
E_{33}	-0.21%	-0.15%
v_{12}	-0.23%	-0.15%
v_{13}	-0.11%	-0.07%
v_{23}	-0.10%	-0.11%
G_{12}	1.32%	3.28%
G_{13}	-0.05%	-3.97%
G_{23}	-3.42%	-0.08%

3.3 Results and Verification

Six unidirectional IM7/8552 small-plate torsion specimens are used to generate the interlaminar shear stress-strain curve in the 1-3 principal material plane; and the results are compared with the material properties generated based on the short-beam method [31].

For each small-plate torsion specimen, the FEM-based maximum shear stress (which is in the region of the maximum shear strain) is extracted and plotted versus the corresponding maximum DIC-based shear strain for the load values at which digital images were generated. The updated log-linear, stress-strain curve is generated using least-squares approximation. The shear properties are subsequently updated in the FEM, and the stress analysis is repeated. The procedure continues until the change of stress state is negligible. At iteration k, the change of stress state is tracked by a normalized root-mean square error ε, using the stress state at iteration k - 1:

$$\epsilon = \sqrt{\frac{1}{N}\sum_{i=1}^{N}\left(\frac{\sigma_i^{[k]}-\sigma_i^{[k-1]}}{\sigma_i^{[k-1]}}\right)^2} \qquad 9$$

where N represents the number of load steps at which digital images were generated and σ_i are the maximum shear stress values at each step.

A 3% maximum change of stress between subsequent iterations was used as the threshold to stop the iterative procedure. For the stress-strain curves in the 1-3 material plane, convergence was typically achieved after one or two iterations. Once convergence has been established, the strain distribution obtained with the new material properties is compared to the DIC-based strains for verification. Figure 14 shows a typical comparison of the FEM-based computed strains and the DIC-based measured strains illustrating excellent agreement. All six small-plate torsion verification test specimens exhibit similar behavior.

Results for all six specimens are summarized in Table 4. The scatter in the listed log-linear parameters, G_{13}, K_{13}, and n_{13}, is small as indicated by lower than 3% coefficients of variation (COV).

Table 4. Updated Interlaminar Shear Stress-Strain Constitutive Properties

for IM7/8552 Small-Plate Torsion Specimens.

(a) 1-3 principal material plane

Specimens	G_{13}, Msi (GPa)	$K_{13,}$ ksi (MPa)	n_{13}
1	0.754 (5.20)	44.9 (310)	0.304
2	0.742 (5.12)	43.9 (303)	0.300
3	0.758 (5.23)	45.4 (313)	0.308
4	0.731 (5.04)	44.5 (307)	0.308
5	0.734 (5.06)	44.7 (308)	0.309
6	0.737 (5.08)	287 (41.7)	0.290
AVG	**0.743 (5.12)**	**44.2 (305)**	**0.303**
COV	**1.50%**	**2.99%**	**2.33%**

(b) 2-3 principal material plane

Specimens	G_{23}, Msi (GPa)	$K_{23,}$ ksi (MPa)	n_{23}
1	0.407 (2.81)	32.1 (222)	0.219
2	0.409 (2.82)	31.1 (215)	0.219
3	0.478 (3.30)	31.1 (214)	0.213
4	0.473 (3.27)	26.3 (181)	0.177
5	0.440 (3.04)	37.1 (256)	0.236
6	0.440 (3.03)	34.7 (239)	0.226
7	0.455 (3.13)	33.2 (229)	0.208
8	0.424 (2.92)	34.2 (236)	0.221
9	0.456 (3.14)	33.2 (229)	0.212
10	0.431 (2.97)	32.0 (221)	0.212
11	0.435 (3.00)	33.4 (231)	0.212
AVG	**0.441 (3.04)**	**32.6 (225)**	**0.214**
COV	**4.68%**	**5.30%**	**3.72%**

Figure 16 compares average 1-3 plane interlaminar shear stress-strain curves from the small-plate torsion tests and the short-beam tests in Reference [31]. The stress-strain curves obtained by the two methods are in excellent agreement. In particular, the difference in average shear modulus G_{13} is below 1% and the two curves match closely at large strains. The average K_{13} and n_{13} values obtained from the small-plate torsion test differ almost 20% from the average results found in short-beam tests. However, the difference in the stress values between the two average curves is less than 4.5% at all strain levels. Therefore, the change in stress state should be considered in the interpretation of the results, rather than the difference in the numerical values of the average secant-intercept modulus and the exponent in the Ramberg-Osgood equations.

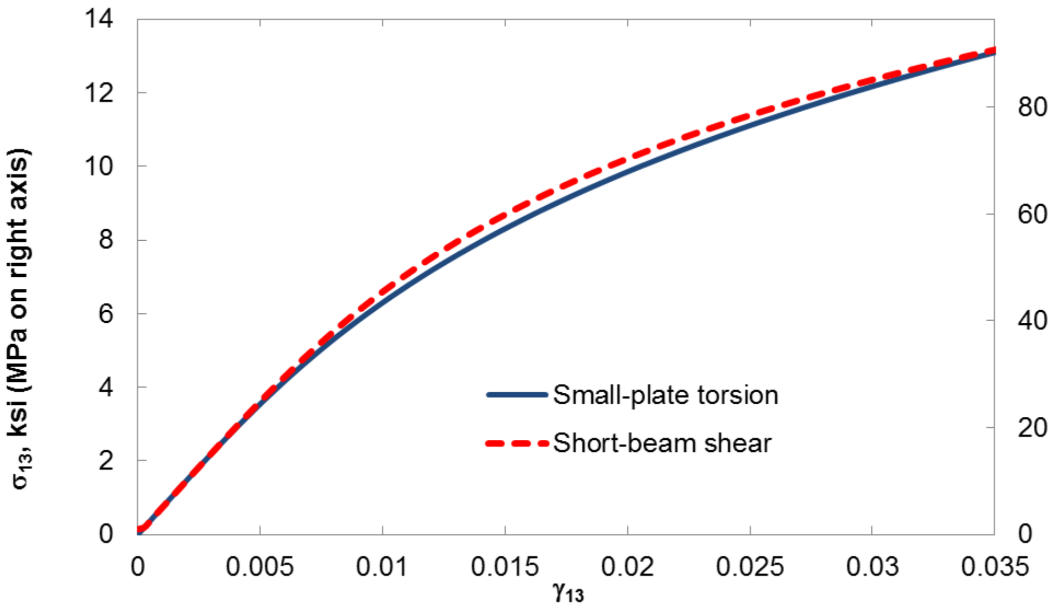

Figure 16. Average shear stress-strain curves obtained from small-plate torsion tests compared to initial approximation from SBS in the 1-3 material plane.

All 11 unidirectional small-plate torsion coupons tested in this work were used for to assess the interlaminar shear stress-strain curve in the 2-3 material plane. The initial material properties used in the FEM are defined in Tables 1 and 2 and equation (8) describing the transverse isotropic approximation for the 2-3 shear modulus.

Similar to the procedure described in the previous paragraph, the maximum FEM-based, 2-3 plane interlaminar shear stress and maximum DIC-based, measured 2-3 plane interlaminar shear strain are extracted at each load step. The interlaminar shear material properties are updated using the calculated stresses until convergence of the stress state has been achieved.

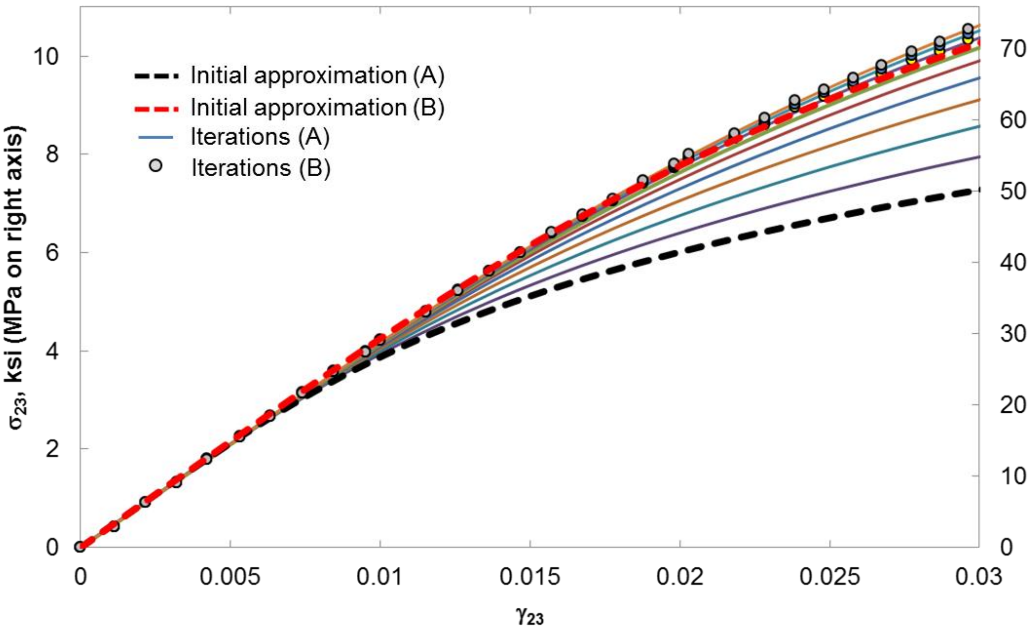

Figure 17. Typical iterations for 2-3 interlaminar shear stress-strain response, corresponding to the two initial approximations (A) and (B) of the secant intercept modulus K_{23}.

A typical example of the iterative procedure corresponding to initial approximations (A) and (B) of the secant-intercept modulus K_{23} is shown in Figure 17 for one of the specimens. It is demonstrated that with both initial approximations, the iterative process of generating stress-strain curves converges to the same result. Approximation (B) with $K_{23} = K_{13}$ is significantly more accurate compared to (A), with only 3 iterations required to establish convergence, compared to 9 iterations for approximation (A).

To assess the accuracy of the converged material constitutive properties, the FEM-based, computed strain distribution is compared with the DIC-based, measured strain distribution. Figure 14 shows a typical comparison between the FEM strains and DIC strains immediately before the specimen failure. Excellent agreement between the FEM-computed and the DIC-measured strains was found for all the specimens tested.

The individual 2-3 plane, interlaminar shear stress-strain curves for all IM7/8552 carbon/epoxy specimens tested in this work are presented in Figure 18. Figure 18 also shows the average stress-strain curve and provides comparison with the initial approximation (B) of the 2-3 plane interlaminar shear stress-strain curve. The average converged stress-strain response values for G_{23}, K_{23}, and n_{23} are listed in Figure 18.

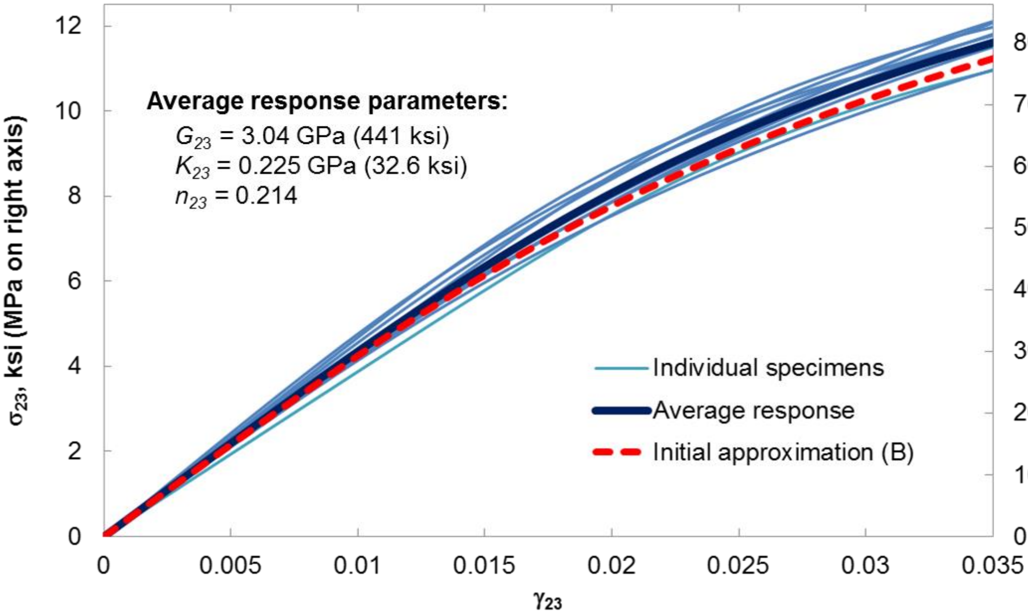

Figure 18. Individual 2-3 plane interlaminar shear stress-strain curves for the 11 IM7/8552 specimens, average response, and the initial approximation (B) with $K_{23} = K_{13.}$

Log-linear parameters for the 10 specimens tested are summarized in Table 4(b). A reasonable variability in G_{23}, $K_{23,}$ and n_{23} values is demonstrated, with the maximum variability in the K_{23} secant-intercept modulus (COV 5.3%). The average linear shear modulus G_{23} is consistent with the transverse isotropy assumption, with less than 1% difference. It is found that the secant-intercept modulus and exponent values obtained for the 1-3 plane also represent a good approximation for characterization of the matrix-dominated nonlinear interlaminar shear behavior in the 2-3 principal material plane, which is a meaningful result as similar interlaminar shear nonlinearity in both 1-3 and 2-3 principal material planes can be anticipated.

Chapter 4

Determination of the Three-Dimensional Material Characterization from Full-Field Measurements

It was shown in the last chapter that the interlaminar shear stress-strain relations could be obtained using a stress-update procedure in which the material properties in the FEM were updated until the change in the maximum FEM-based shear stress became negligible. However, the technique used only small regions of the test specimen surfaces, approaching line segments or points, in the material characterization. In order to take full advantage of the full-field measurement, all DIC surface strain data must be utilized. Furthermore, the method only assessed the interlaminar shear behavior and considered each plane independent of the others. Within this chapter, a methodology is developed to measure 3D material properties by utilizing DIC measurement from the entire surface for both in-plane and interlaminar shear behavior [55,56]. This method considers the deformation on all planes simultaneously; therefore significantly reducing the number of FEM iterations compared to previous methods, handling one plane at a time.

The method is divided into two stages. In the first stage, the SBS method is used to construct the initial approximation of the material constitutive model for use in stage two, in which the more complex loading configuration of the small-plate torsion specimen requires an accurate initial guess of the material parameters to generate meaningful stress calculations. Within both stages, an iterative FEMU-inverse method is used to determine the optimal material properties.

4.1 Inverse Problem Formulation

Determining the constitutive properties for the full-field SBS and small-plate torsion specimens is not a direct problem – i.e., the constitutive model relating the stress and strain is not known [46]. Therefore, determining the properties becomes an inverse problem that must be solved iteratively. Material properties are treated as unknowns. Each iteration of the FEM will calculate stresses at the location of strain measurement. The strains calculated using FEM are compared with the DIC-measured strains using a squared error function, with the least error corresponding to the best agreement. The nonlinear material properties are calculated in each iteration using a nonlinear least squares approximation and the material model is rederived. The sensitivity matrix (Jacobian) of derivatives of strains with respect to the material parameters will be generated. A gradient-based optimization algorithm, the

Levenberg-Marquardt (L-M) method [57], is used to determine the optimal material relation.

4.1.1 Optimization Algorithm

The FEMU method used in this work for assessment of the material constitutive properties of composites, including nonlinear shear behavior, is based on a least squares optimization procedure. The objective error function, $C(p)$, for the optimization problem is defined as the sum of the weighted squares of the differences between DIC-measured and FEM-computed strains, as shown in the following equation:

$$C(p) = \sum_{i=1}^{N} \left[\sum_{j=1}^{M} w_{jj} \left(\varepsilon_j^{DIC} - \varepsilon_j^{FEM}(p) \right)^2 \right]_i \qquad 10$$

where p represents the set of unknown material parameters; M is the number of spatial grid points for evaluation of experimental and numerical strains; N the number of load steps at which digital images are generated; ε_j^{DIC}, ε_j^{FEM}, and w_{jj} are the DIC strains, FEM strains and weighting factor at spatial grid point j, respectively.

In matrix notation, equation (10) can be expressed as:

$$C(p) = \left(\varepsilon^{DIC} - \varepsilon^{FEM}(\boldsymbol{p}) \right)^T \boldsymbol{W} \left(\varepsilon^{DIC} - \varepsilon^{FEM}(\boldsymbol{p}) \right) \qquad 11$$

where ε^{DIC} and ε^{FEM} are the measured and computed strain vectors of order $M \times N$, respectively. $\boldsymbol{p}$ is the vector of unknown material parameters and $\boldsymbol{W}$ is the weight matrix such as:

$$\boldsymbol{W} = \left[W_{ij}\right]_{MN} \text{ with } W_{ij} = \begin{cases} w_{ii} & if\ i = j \\ 0 & if\ i \neq j \end{cases}. \qquad 12$$

Ideally, the weighting factors in the objective function should be determined using the variance, σ_j^2, in the experimental strain measurement at grid point j:

$$w_{jj} = \frac{1}{\sigma_j^2}. \qquad 13$$

The confidence margin output parameter available in the DIC software is calculated from the covariance matrix of the correlation function [14] and is used in this work to estimate σ_j in equation (10). Weighted residuals used in the definition of the objective function allow reducing the sensitivity of the optimization algorithm to measurement noise, since the contribution of noisy data points with high variance is scaled down by the inverse of their variance.

The advantage of using strains in the expression of the objective function instead of using another quantity such as displacements, is that the exact knowledge of the boundary conditions is less important and the sensitivity (or Jacobian) matrix used in the optimization procedure can be efficiently approximated without resorting to using costly evaluation methods such as finite differences, as will be discussed later in this paper. It is worth noting that it might be necessary to consider a number N load steps throughout the loading history of the specimen all the way to failure, in order to capture material nonlinearities. For simplifying purposes, only one strain component ε is used in the expression of the objective function, $C(p)$. For simultaneous assessment of multiple constitutive relations, all strain components involved in the stress-strain relationships need to be accounted for [55, 56].

No explicit relationship exists between FEM-computed strain components and the unknown material parameters; therefore the optimization problem has to be solved iteratively. The L–M algorithm [57] is used to solve for the optimum material parameters that minimize the weighted least squares objective function. At iteration k, the material parameters are updated such as:

$$p^k = p^{k-1} + \Delta p^k$$

$$\Delta p^k = [\boldsymbol{J}^{\boldsymbol{T}}\boldsymbol{W}\boldsymbol{J} + \lambda^k diag(\boldsymbol{J}^{\boldsymbol{T}}\boldsymbol{W}\boldsymbol{J})]^{-1}\boldsymbol{J}^{\boldsymbol{T}}\boldsymbol{W}\boldsymbol{J}\Big(\varepsilon^{DIC} - \varepsilon^{FEM}(\boldsymbol{p}^k)\Big) \qquad 14$$

where Δp^k, $\boldsymbol{J}$, and λ^k are, respectively, the vector of parameter updates, the Jacobian or sensitivity matrix and the L-M damping parameter at iteration k. The Jacobian matrix $\boldsymbol{J}$ is defined as the matrix of partial derivatives of the FEM-computed strain components with respect to the material parameters and is updated at each iteration k.

$$\boldsymbol{J} = \boldsymbol{J}^k = \left[\frac{\partial \varepsilon^{FEM}{}_i}{\partial p_i}\right]_{MN \times P} \qquad 15$$

with P indicating the number of material parameters.

The optimization variables are used to represent the nonlinear shear behavior in the three principal material planes using the Ramberg-Osgood model. There will be three optimization variables for a SBS analysis and nine variables for a small-plate torsion analysis. To be physically acceptable, the Ramberg-Osgood parameters must be positive. However, it was not necessary to explicitly introduce constraints in the optimization algorithm. Normalized parameters based on the physical initial approximations as given in Table 1 and an appropriate initial value for the L-M damping parameter λ were sufficient to keep the optimization variables within the physical domain. The initial value chosen for the L-M damping factor was $\lambda^0 = 1.0$. Lower initial values could allow for faster convergence at the beginning of the optimization process; however, a step too long with a lower L-M damping factor could reach unacceptable, non-physical negative values for the parameters. Using $\lambda^0 = 1.0$ allowed for good performance of the L-M algorithm, while eliminating the likelihood of out-of-bound variations of the parameters.

The L-M method is an optimum compromise between the Gauss-Newton optimization algorithm and the steepest descent algorithm. If the value of the damping parameter λ is small, then the L-M algorithm becomes close to the Gauss-Newton method. For large values of λ, the parameters step updates are taken approximately in the direction of the gradient and the L-M method becomes equivalent to the steepest descent. As proposed by Marquardt, the damping parameter should be updated by comparing the new objective function $C(p^k)$ to the objective function at the previous iteration $C(p^{k-1})$ to ensure an optimum convergence of the L-M algorithm. The gain factor Q is introduced, as proposed in Reference [57]:

$$Q^k = \frac{C(\boldsymbol{p}^{k-1}) - C(\boldsymbol{p}^k)}{2\Delta\boldsymbol{p}^{k^T}\left(\lambda^k\Delta\boldsymbol{p}^k + \boldsymbol{J}^T\boldsymbol{W}\left(\varepsilon^{DIC} - \varepsilon^{FEM}(\boldsymbol{p}^k)\right)\right)}. \qquad 16$$

If the gain factor Q is negative, then the condition of a decreasing objective function is not met. The parameters update $\Delta\mathbf{p}$ is not accepted and the L-M damping factor is increased to get closer to the steepest decent direction and reduce the step length. If Q is larger, then the step is accepted and the damping parameter is reduced to get closer to the

Gauss-Newton direction in the next iteration. For small positive values of Q, the step is accepted, but it might be beneficial for convergence purposes to use a larger damping parameter in the next iteration. The update strategy of the L-M damping parameter and the vector of unknown parameters can be summarized as follows:

$$\begin{array}{ll} Q > 0 & \boldsymbol{p}^k = \boldsymbol{p}^{k-1} + \Delta\boldsymbol{p}^k \\ Q \leq 0 & \boldsymbol{p}^k = \boldsymbol{p}^{k-1} \\ Q < q_1 & \lambda^k = \beta\lambda^{k-1} \\ Q > \ q_2 & \lambda^k = \dfrac{\lambda^{k-1}}{\mu} \\ q_1 \leq Q \leq q_2 & \lambda^k = \lambda^{k-1} \end{array} \qquad 17$$

where $0 < q_1 < q_2 < 1$ and $\mu, \beta > 0$ are user-specified parameters. The values of these parameters used in this work are: q_1 = 0.25, q_2 = 0.75, β = 9.0, μ = 11.0. These values, provided with good overall performance of the L-M algorithm although using different values, had little effect on the final solution [55,56].

The L-M iterative procedure is stopped when the either maximum normalized error in parameter update or the reduction in objective function at iteration k is less than a user-defined threshold ε:

$$max\left|\frac{\Delta p_i}{p_i}\right| \leq \varepsilon\ for\ i = 1\ \ldots.P \tag{18}$$

or

$$\frac{C(p^{k-1}) - C(p^k)}{C(p^{k-1})} \leq \varepsilon\ at\ iteration\ k \tag{19}$$

4.1.2 The Jacobian Matrix

Table 5. Derivatives of the In-Plane Shear Component with Respect to Parameters of the In-Plane Ramberg-Osgood Equation.

Derivative	G_{12}	K_{12}	n_{12}
$\frac{\partial \gamma_{12}^{FEM}}{\partial p}$	$-\frac{\tau_{12}^{FEM}}{{G_{12}}^2}$	$-\frac{1}{K_{12}n_{12}}\left(\frac{\tau_{12}^{FEM}}{K_{12}}\right)^{\frac{1}{n_{12}}}$	$-\frac{1}{{n_{12}}^2}\left(\frac{\tau_{12}^{FEM}}{K_{12}}\right)^{\frac{1}{n_{12}}} \ln\left(\frac{\tau_{12}^{FEM}}{K_{12}}\right)$

By assuming that the variation of stress with respect to the material parameters is small, equations can be used to derive an analytical expression of the Jacobian matrix defined in equation (15). For instance, the analytical expressions of the derivatives of the in-plane shear strain component γ_{12} with respect to the in-plane Ramberg-Osgood parameters (G_{12}, K_{12}, n_{12}) are given in Table 5. At each iteration, the Jacobian matrix is updated using the computed stresses and material parameters from the previous accepted step of the L-M algorithm. This formulation allows for a very efficient computation of the Jacobian matrix, since no additional FEM-based analysis is required.

The order of magnitude of the different material parameters used in the constitutive model derived in equation (11) can vary significantly. For instance, shear modulus for carbon/epoxy materials are typically on the order of 10^6 psi (10^9 Pa), whereas the n exponent is in the order of 10^{-1}. Due to these orders of magnitude differences, the computation of the Jacobian matrix and the inverse matrix in equation (15) can be affected by experimental and numerical noise and largely reduce the accuracy of the L-M optimization procedure. To overcome such difficulties, the material parameters are scaled using the initial approximation $\boldsymbol{p_0}$ of the material parameters vector and the sensitivities are computed with respect to the normalized parameters:

$$\overline{p_J} = \frac{p_j}{p_{0\,j}}$$

$$\frac{\partial \varepsilon^{FEM}{}_i}{\partial \overline{p_J}} = p_{0\,j}\,\frac{\partial \varepsilon^{FEM}{}_i}{\partial p_j}. \qquad 20$$

The Jacobian matrix is computed for the number of material parameters p_i included in the optimization; 3 for each SBS specimen, corresponding to the Ramberg-Osgood (G,*K,n*) parameters in the material plane considered, and 9 for the small-plate torsion, corresponding to the Ramberg-Osgood (G,K,n) parameters in all three principal material planes Analytical approximations of the sensitivity terms in the Jacobian matrix are obtained by substituting equation (5) in equation (15) and assuming that the variation of stress with respect to the material parameters is negligible. An exact computation of the Jacobian matrix is typically not required in least squares optimization methods; however, approximations that are too far from the exact solution will most likely lead to a very slow convergence of the algorithm. In this work, convergence was achieved within 4-6 iterations, which is acceptable and supports the argument that the variation of the stress with respect to the material parameters can be neglected. To consolidate the argument, the Jacobian matrix was computed using the finite differences techniques with a forward difference scheme and compared to the results with data obtained from the analytical approximation that neglects stress variation. The Jacobian calculated from the finite difference technique remains an approximation of the Jacobian matrix, however, no assumption is made on the variation of stress with respect to the parameters.

The stress-strain relations obtained by finite differences for a typical specimen were in close agreement with the results based on the analytical approximation of the sensitivities. However, nine additional FEM analyses at each iteration of the optimization procedure are required to compute the Jacobian matrix in finite differences method. No additional costly FEM calculation is needed with the analytical approximation of the Jacobian matrix, since sensitivities are computed from the same FEM analysis used for evaluation of the objective function.

4.2 Full-Field Strain Measurement

4.2.1 Short-Beam Shear

For this work, 15 SBS specimens were manufactured from a 34 ply 0.25 in (6.35 mm) thick unidirectional IM7/8552 carbon/epoxy tape panel, cured at 350 degrees F per prepreg manufacturer’s instructions [53]. A total of 10 specimens were cut along the 0-degree plane for assessment of the 1-2 and 1-3 surface strain distributions; 5 specimens were cut along the 90-degree plane to test in the 2-3 plane. Note that the specimens used in this work were cut from three different panels manufactured by different manufacturers years apart. The width is 0.25 in (6.35 mm); and the specimen length is 1.75 in (4.45 cm).

A standard test fixture, as specified in ASTM D2344 [17], with adjustable span and interchangeable loading noses is used for these tests. A loading nose diameter of 4.0 in (10.16 cm) is used for the 1-2 and 1-3 plane tests, to reduce compressive damage underneath the loading nose and ensure a shear failure. A 2.0 in (5.08 cm) loading nose is used for the 2-3 plane tests. A standard lower support diameter of 0.125 in (3.175 mm) is used for all specimens.

A span of 1.2 in (3.048 cm) is used for all tests, resulting in a 4.8 span-to-thickness ratio, which is within the range specified by ASTM D2344 [17]. To ensure the alignment of the test configuration, an alignment tool, with width such that the span is set to the desired value, is used to center the loading nose with respect to the supports as shown on the right side of Figure 19. Once centered, the bolts securing the supports to the fixture are tightened so that they will not move during the duration of the tests. Alignment jigs can be manufactured for any span-to-thickness ratio, if so desired.

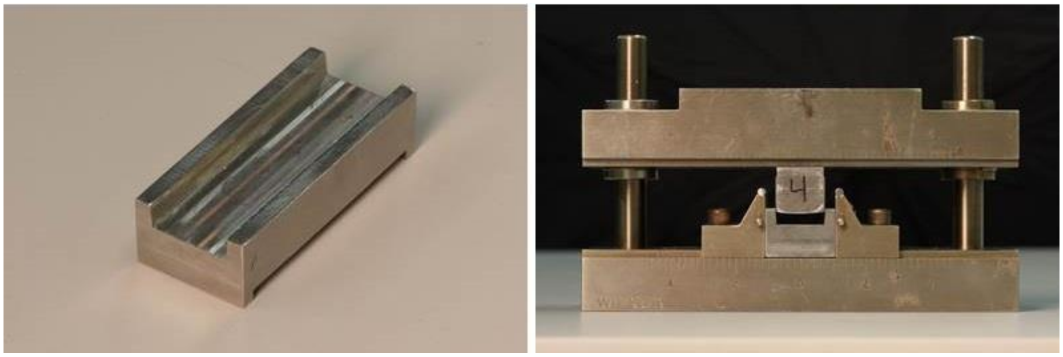

Figure 19. Alignment jig used for centering the loading nose between the supports for a short-beam shear test.

The fixture is installed in a servo-hydraulic test frame with a 2,000-lb (8896 N) capacity load cell and monotonic load is applied to the specimen at a 0.05 in/min (1.27 mm/min) crosshead displacement rate until failure occurs. Specimens tested in the 1-2 and 1-3 principal material plane failed in shear. No compression cracks under the loading nose were recorded. Specimens tested in the 2-3 principal material plane failed in tension.

DIC is used to assess the surface strain components throughout the duration of the test. Two 16 megapixel (MP) stereovision digital cameras capture images of the specimen surface as load is applied. VIC3D-7 [29] is used to analyze the images and generate the full-field strain measurements based on a subset size of 35 x 35 pixels corresponding to a physical area of approximately 0.001 in^2 (0.67 mm^2).

The displacement data was obtained on 7 pixel centers resulting in 24,500 data points per load level. Engineering strains are obtained by numerically differentiating the displacement field using the strain computation algorithm in the VIC-3D software. A Gaussian smoothing filter of size 15 pixels is used to reduce any noise from the displacement field.

A representative of the full-field strain distributions obtained from testing for the 1-2, 1-3, and 2-3 plane are shown in Figures 20 through 22, respectively. Average maximum shear strains of 8% and 3.5% are observed in the 1-2 and 1-3 planes, respectively. All 2-3 specimens failed in tension under the loading nose at maximum shear strains of 0.5%. The axial and transverse strains for all planes were an order of magnitude lower than the shear strains.

In this work, the full-field strain data is used, including regions underneath the loading nose, which exhibit a fully populate strain state. Full-field data for each load level (i.e., image) is exported for comparison with FEM-predicted strains.

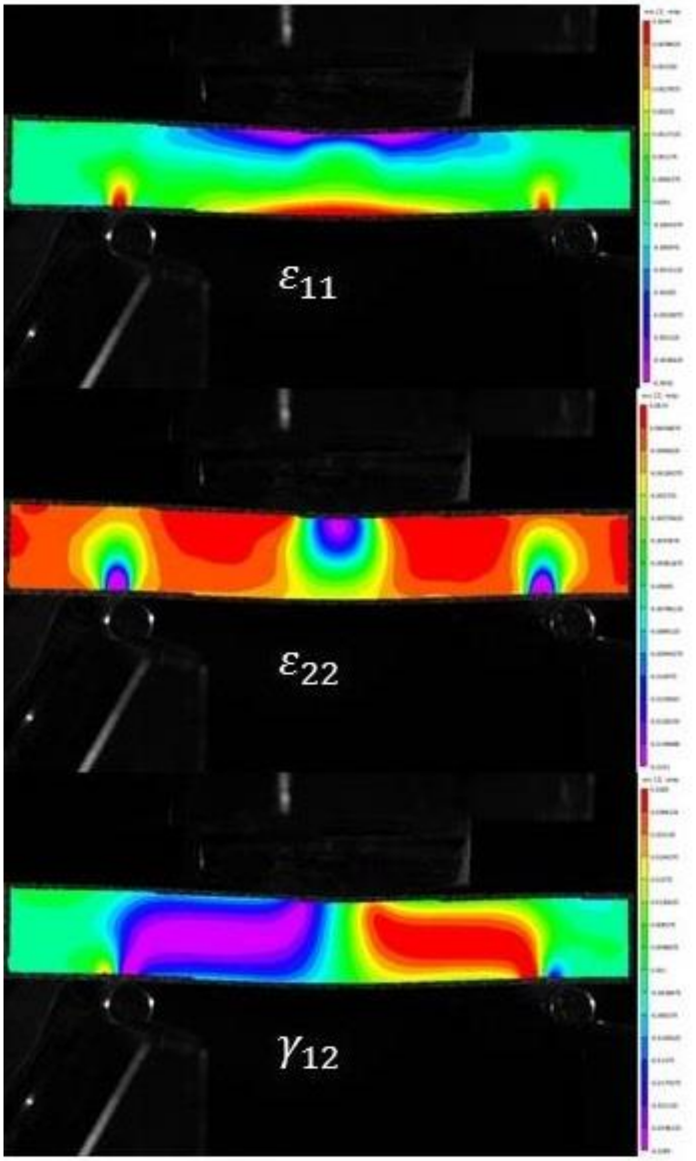

Figure 20. Full-field strain distribution for short-beam specimens loaded in the 1-2 principal material plane at 67% failure load.

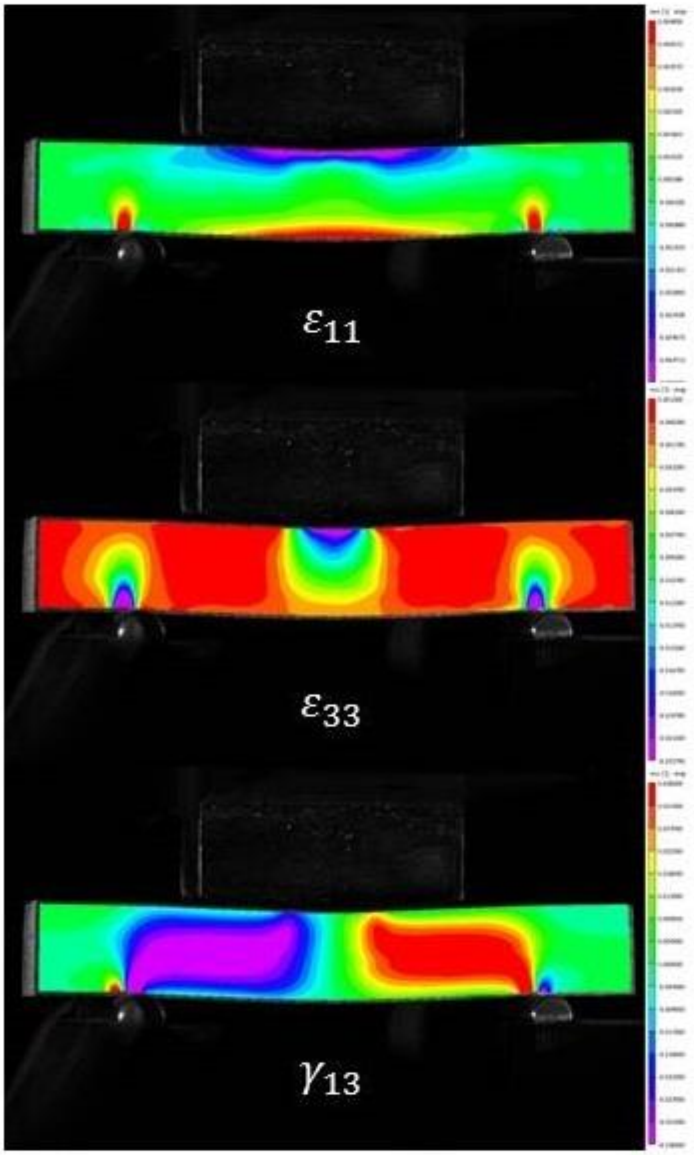

Figure 21. Full-field strain distributions for short-beam specimens loaded in the 1-3 principal material plane at 99% failure load.

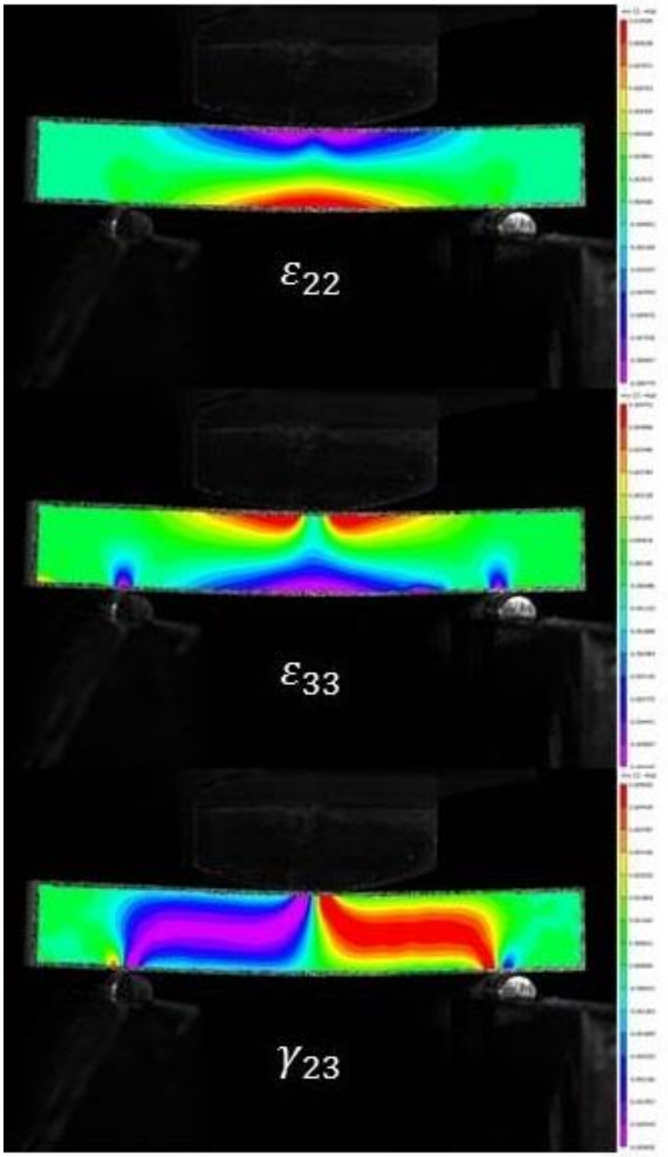

Figure 22. Full-field strain distributions for short-beam specimens loaded in the 2-3 principal material plane at 95% failure load.

The DIC algorithm also computes the confidence margins for the strain matching based on the covariance of the correlation function [29], which is used as a weighting factor in the optimization algorithm (see Section 4.1.1). The approximate covariance matrix is computed from the inverse of the Hessian matrix in the VIC 3D software and gives an indication as to the variability in the matching process. Whether a solution to the correlation function exists depends on whether the inverse of the Hessian matrix can be computed. For overly noisy or poor data, the Hessian matrix is not invertible and a solution cannot be found. Additionally, if the variance in the displacements is greater than 0.05 (i.e., outside the 95% confidence interval), the data is removed from the analysis procedure. The confidence interval (sigma, σ) in the DIC software represents one standard deviation, given in pixels. A representative contour plot of the confidence intervals is shown in Figure 23 for a short-beam specimen.

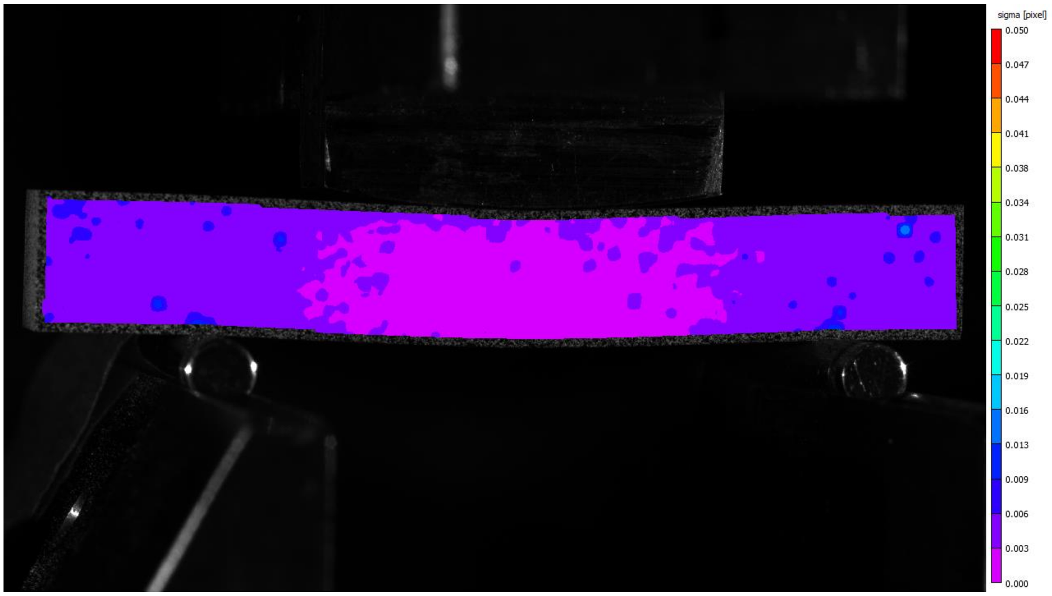

Figure 23. A contour plot of the confidence interval (in pixels) for a typical SBS specimen.

From Figure 23, it is evident by the low values of the variance that excellent correlation is found between undeformed and deformed subsets throughout the loading history. Points with lower confidence generally indicate a presence of noise within the data. Using the confidence interval data, we can construct a useful weighting factor based on the reliability of the DIC data at each point.

4.2.2 Small-Plate Torsion

Eleven small rectangular cross-section flat plate specimens were machined from a unidirectional IM7/8552 carbon/epoxy unidirectional tape panel cured at 350 degrees F per prepreg manufacturer's specifications [53]. A smaller specimen is used in this work, as compared with the specimens described in Chapter 3. This is done to verify the sensitivity of the test method to the size of the specimen and to ensure it does not affect the results of the material characterization, confirming the reliability of the material properties obtained using the stress update method. The specimen measure 1.0 in long x 1.0 in wide x 0.168 in thick (25.4 mm x 25.4 mm x 4.27 mm). Specimens are manufactured such that the top (and bottom) surfaces of the specimen coincide with the 1-2 plane; and the side surfaces are the 2-3 and 1-3 principal material planes, as show in Figure 24.

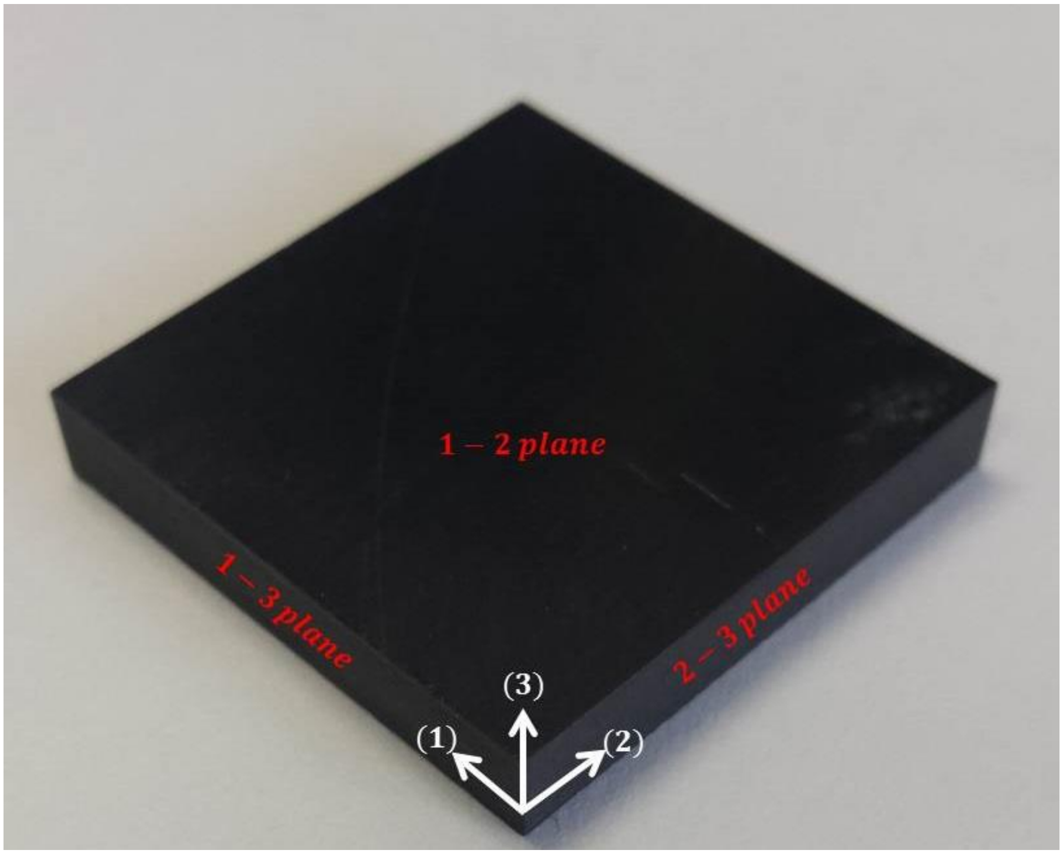

Figure 24. Principal material planes on the small-plate torsion specimen.

A smaller test fixture was designed to allow for simultaneous assessment of the shear stress-strain response in the in-plane (1-2), and interlaminar (2-3 and 1-3) principal material planes. The fixture, shown in Figure 2, consists of two loading points (top of fixture) and two support points (bottom of fixture), mounted to rigid cross-beams with a support length of 0.7 in (1.78 cm). The loading and support points are hemispherical in shape with a diameter of 0.25 in (6.35 mm).

The fixture is installed in a servo-hydraulic test frame. Specimens were loaded in a servo-hydraulic load frame at a constant 0.05 in/min (1.27 mm/min) crosshead displacement rate until failure. The tests were conducted at 72 degrees F room-temperature, ambient conditions.

DIC is used to assess the strain components on all principal material planes, simultaneously. Three synchronized 16-megapixel stereo camera systems monitored strains in the 1-2, 1-3, and 2-3 principal material planes. The cameras were triggered in tandem to ensure images were captured at the same load. The importance of this detail is realized during FEM analysis requiring strain data for each plane at the same load for comparison to FEM-predicted strains. Figure 2 shows a setup for simultaneously monitoring surface strain and typical engineering shear strain components. The strain analysis is performed in VIC-3D software [29] using a subset (data point) size of 35x35 pixels, corresponding to approximately 0.275 mm^2 for these particular tests. Data was obtained on 7 pixel centers, resulting in approximately 26,000 data points per load case.

The default coordinate system of the DIC data is defined based on the master camera with the origin at the center of the image, the positive x-axis directed along the horizontal to the right and the positive y-axis upward. Care is taken during experimental setup to align the length of the specimen (in the 1-3 and 2-3 planes) with the horizontal axis of the master camera so rotation of the DIC data is not required. The nature of the experimental setup does not allow for the cameras to be aligned with an edge of the specimen; therefore, during the post processing phase, the coordinate transformation tool is used in VIC 3D-7 to align the positive x-axis with the fiber direction of the small-plate torsion specimen. The 1-2 shear-strain field is shown in Figure 25 before (a) and after (b) coordinate system transformation.

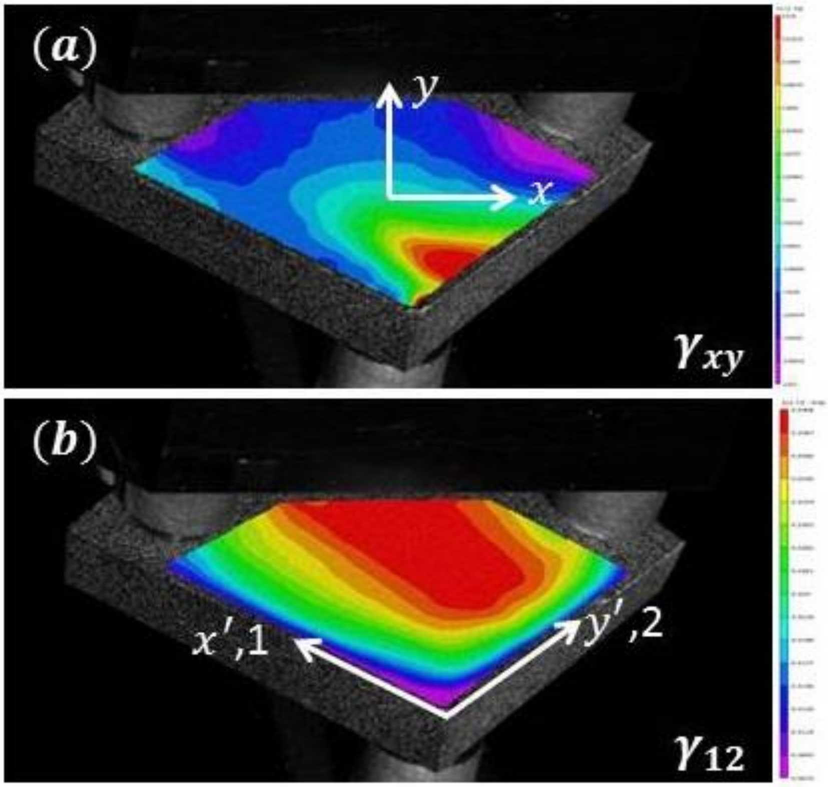

Figure 25. The shear-strain field for the 1-2 principal material plane before (a) and after (b) a coordinate transformation to align the DIC data coordinate system with the principal material directions.

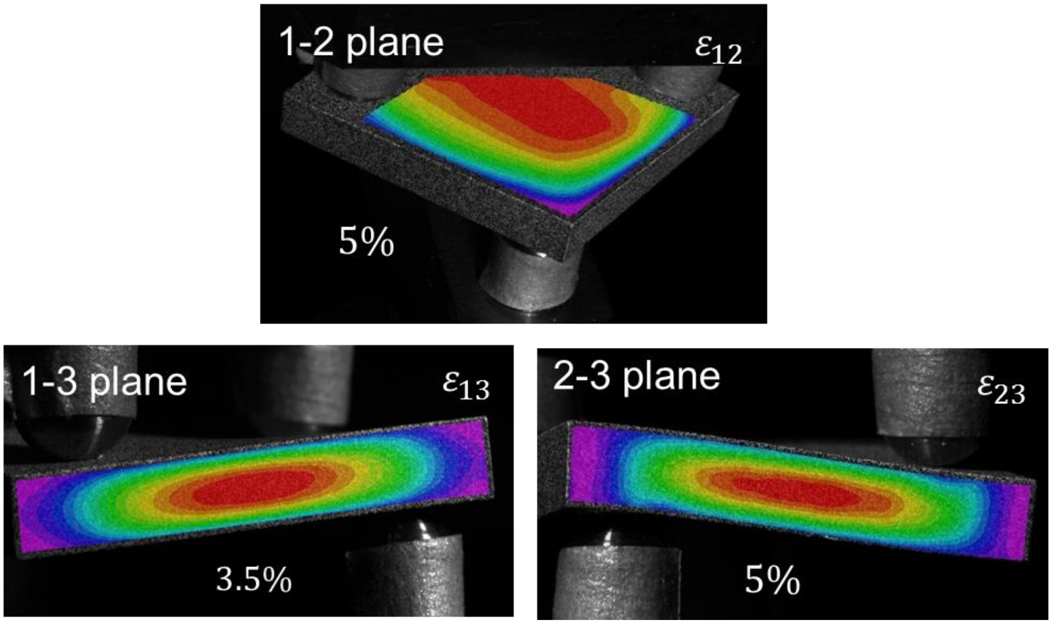

Figure 26. Maximum DIC shear strains measured in (a) 1-2 principal material plane, (b) 1-3 plane, and (c) 2-3 plane of the small-plate torsion specimen.

Figure 26 shows typical engineering shear strain components measured before failure using the DIC technique. Maximum in-plane and interlaminar shear strains greater than 5% are observed in both the 1-2 and 2-3 principal material planes, respectively and greater than 3% in the 1-3 principal material plane before failure. This demonstrates that this method allows for a simultaneous assessment of shear strains in highly nonlinear stress-strain regime for polymeric composites in all material planes.

4.3 Numerical Model

4.3.1 Short-Beam Shear

A three-dimensional solid FEM is developed using commercial FEM software ABAQUS [54] to determine the stresses in a SBS coupon. The model consists of 24,600 C3D8I elements, which are well-suited for the bending problem considered, is shown in Figure 27(a). Incompatible mode elements are well suited for the torsion/bending problems considered in this work, since the additional incompatible deformation modes, added to the element formulation, eliminate parasitic shear stresses and stiffening usually found in the bending response of regular first-order elements [54]. Symmetric boundary conditions are implemented at the mid-plane (z=0) to model the half-width of the specimen to reduce computation time. The FEM accounts for geometric nonlinearity, material nonlinearity and contact interaction. The loading nose and supports are modeled as rigid body cylindrical surfaces. The contact interaction between the loading nose and supports and the short-beam specimen is modeled using surface-to surface contact, which realistically approximates the loading configuration. The material constitutive model, including nonlinear shear behavior, is implemented using the user-defined subroutine UMAT (see Appendix A). The mesh, as shown in Figure 27(a) is refined in locations where the loading nose and supports contact the specimen to accurately capture stress gradients [12]. A concentrated loading condition is applied at the reference point for the loading nose. The FEM analysis is generated at the same load steps as the DIC full-field strain measurements were collected to enable comparison of the strain values.

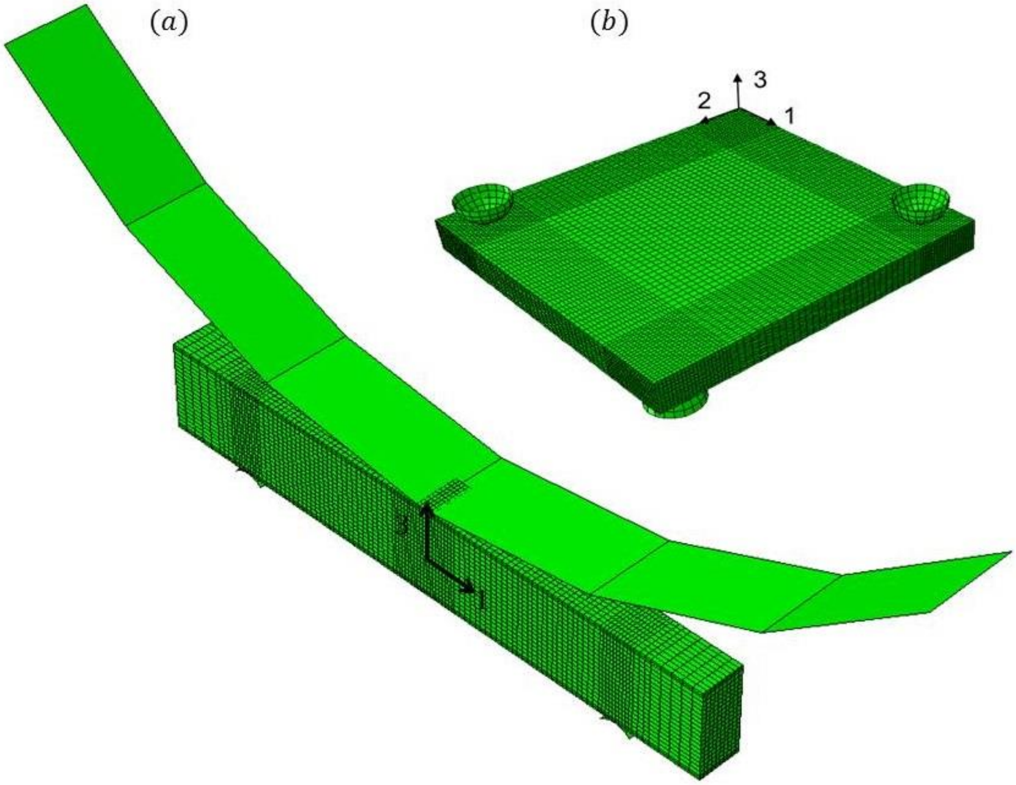

Figure 27. Three-dimensional FEMs for (a) a unidirectional short-beam shear specimen loaded in the 1-3 principal material plane and (b) a unidirectional small-plate torsion specimen.

4.3.2 Small-Plate Torsion

A three-dimensional FEM was developed for stress calculation in the small-plate torsion specimens using ABAQUS [54]. Figure 27(b) shows a typical finite element mesh including approximately 75,000 first-order, three-dimensional incompatible mode solid elements (C3D8I). The supports are assumed to be rigid and are modeled as rigid analytical spherical surfaces. Frictionless contact conditions are assigned between the specimen surfaces and the support points. A surface-to-surface contact formulation is selected in ABAQUS in order to avoid local indentation stresses at contact points. The FEM accounts for geometric nonlinearity; and the material constitutive model for IM7/8552 carbon/epoxy, including shear nonlinearity as defined in equation (5) is implemented via a user subroutine UMAT.

A mesh refinement sensitivity study was performed to ensure that proper stress convergence is achieved. It is worth nothing that at least 16 elements in the thickness direction were required to ensure convergence of the maximum shear stress and correctly capture strong stress gradients. The final converged FEM had approximately 1,150,000 degrees of freedom.

Chapter 5

Results of Three-Dimensional Material Characterization Based on Full-Field Measurements

The full-field strain Levenberg-Marquardt (L-M) optimization method presented in Chapter 4 is used to extract the parameters in the Ramberg-Osgood equations for the shear stress-strain relations for IM7/8552 composite material using DIC full-field shear strain measurements [55,56]. The Python [58] scripting capability of ABAQUS/CAE is used for implementation of the L-M algorithm.

5.1 Interpolation of DIC Strain Data on FEM Nodes

DIC-measured and FEM-computed strain values must be evaluated at the same spatial location for computation of the objective function and the Jacobian matrix used in the L-M algorithm. A set of FEM nodes on each material plane for surface strain measurements has been used for interpolation of element strain results and DIC strain data. Specimen edges are excluded from the analysis, as DIC measurements are typically less accurate at specimen boundaries. The observation windows containing the FEM nodes for interpolation of full-field strain data are illustrated in Figure 28 for the SBS and in Figure 29 for the small-plate torsion. Element C^0 shape functions are used for interpolation of FEM strains at the nodes. The natural neighbor interpolation method implemented in Python function *griddata* of module *SciPy* [59] is used for interpolation of the DIC strains on the nodes of the observation windows.

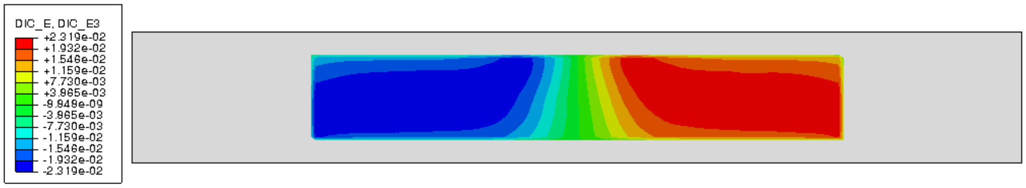

Figure 28. Observation window containing the FEM nodes for interpolation of the full-field strain data and contour plots of interpolated DIC shear strains at maximum load for the SBS specimens.

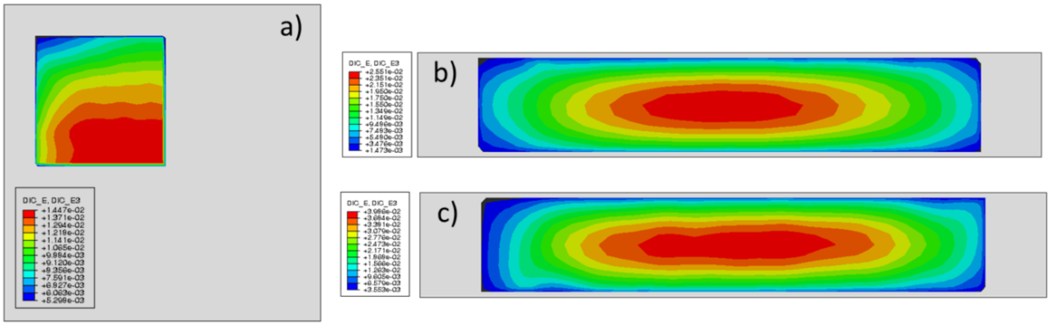

Figure 29. Observation windows containing the FEM nodes for interpolation of full-field strain data and contour plots of interpolated DIC shear strains for small-plate torsion specimens at maximum load in (a) 1-2 principal material plane, (b) 1-3 plane, and (c) 2-3 plane.

It is essential that the DIC data is aligned with respect to the FEM model. Different coordinate systems are used in VIC 3D-7 and ABAQUS and the coordinate transform must be determined to ensure that minimal error between DIC and FEM strains can be achieved. For SBS specimens, the horizontal and vertical positions of the DIC data are shifted to align the data with the loading nose, supports, and neutral axis in the FEM model. For torsion specimens, the DIC data is centered with respect to the surface. It would be advantageous to use artificial markers on the surface of the specimen, which are at a measurable distance from the specimen edge to ensure optimal alignment.

5.2 Initial Approximation of the Material Parameters from Short-Beam Shear Analysis

The optimization is performed for one principal material plane at a time for SBS coupons. A 0.1% maximum relative change in parameter update was used as a stopping criterion for the iterative L-M procedure, as defined in equation (18). An additional stopping criterion of a 0.5% relative change in objective function (equation 19) was introduced to stop the optimization if the relative change in strain state with updated parameters was minimal. The initial approximation of the material properties used in the FEM analysis is given in Table 1. Transverse isotropy has been assumed for the initial approximation of the shear modulus in the 2-3 principal material plane with $G_{23} = 0.433\ Msi\ (2.99\ GPa)$. The initial approximation for the 2-3 plane nonlinear material shear properties in this work is $K_{23} = K_{13} = 36.1$ ksi (0.249 GPa); and $n_{23} = n_{13} = 0.248$.

5.2.1 Interlaminar 1-3 Plane Material Properties

To generate the material properties in the 1-3 principal material plane, the shear modulus, G_{13}, secant intercept modulus, K_{13}, and exponent n_{13} are selected as the optimization variables, while all other material properties remain constant during the analysis. Four iterations were required to establish convergence of the optimization method for the SBS analysis for each specimen. Figure 30(a) shows the normalized objective function for each iteration for a typical SBS specimen tested in the 1-3 plane. The normalized objective function is defined as the ratio of the objective function given in equation (10) at the current iteration by the objective function at the first iteration (equation 19). Rapid decrease in the objective function is seen in the first iteration.

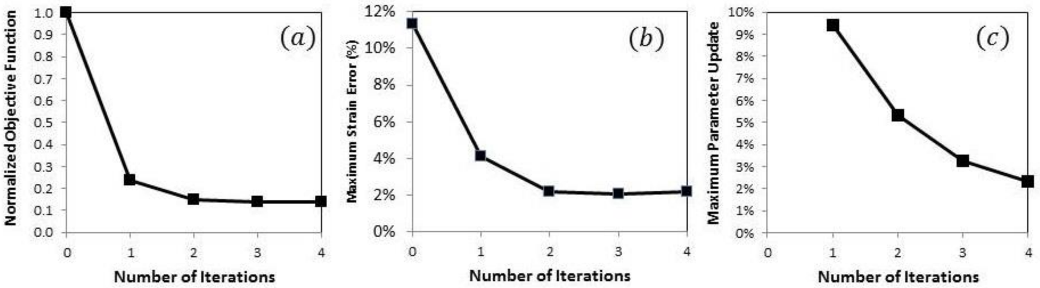

Figure 30. The (a) normalized objective function, (b) maximum RMS strain error, and (c) the maximum parameter update in each iteration for a typical material specimen tested in the 1-3 principal material plane.

Figure 30(b) shows the maximum strain error per iteration for a typical short beam specimen. The root mean square (RMS) normalized error in maximum shear strain is computed as:

$$\varepsilon_{RMS} = \sqrt{\frac{1}{N}\sum_{i=1}^{N}\left(\frac{\varepsilon_{max_i}^{DIC}-\varepsilon_{max_i}^{FEM}}{\varepsilon_{max_i}^{DIC}}\right)^2} \tag{21}$$

where $\varepsilon_{max_i}$are the maximum shear strain components for the 1-3 principal material plane for the *N* number of loading steps. The maximum RMS error is decreased from 16% to 4% for the converged material properties. The maximum update in the material parameters in each iteration is shown in Figure 30(c).

Figure 31 shows a typical comparison between the 1-3 FEM strains and DIC strains immediately before the specimen failure. Excellent agreement between the FEM-computed and the DIC-measured strains was found for all the specimens tested.

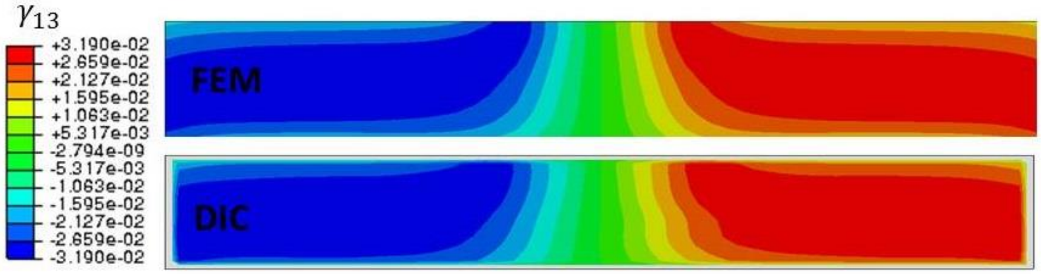

Figure 31. Comparison of the FEM-predicted and DIC-measured strains for a typical specimen loaded in the 1-3 principal material plane at 95% failure load.

Figure 32 shows the converged shear stress-strain curves for SBS specimens tested in the 1-3 principal material plane along with a comparison of the converged material properties with the initial approximation. The numerical values of the converged material properties are presented in Table 6. From Figure 32, it is evident that the nonlinear shear behavior is consistent within the sample of specimens tested. The converged material properties differ from the initial approximation mainly in the nonlinear regime. The linear shear modulus differs from the initial approximation by less than 2.5%, whereas the optimal K_{13} value for this set of data is 14% larger than the initial approximation. The value of the exponent n_{13} is only 1.24% higher.

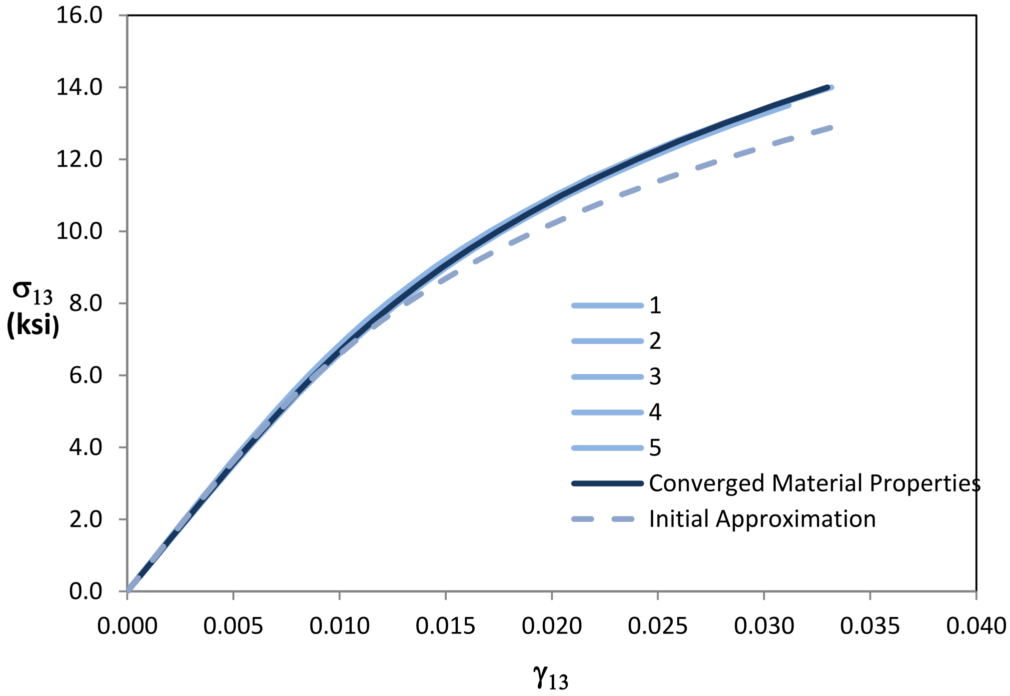

Figure 32. Converged stress-strain curves for the 1-3 principal material plane from SBS tests.

Table 6. Converged Material Properties for the 1-3 Principal Material Plane from SBS tests.

Specimens	G_{13}, Msi (GPa)	$K_{13,}$ ksi (MPa)	n_{13}
1	0.719 (4.96)	44.5 (307)	0.263
2	0.711 (4.90)	40.0 (276)	0.247
3	0.712 (4.91)	40.9 (282)	0.25
4	0.741(5.11)	39.4 (272)	0.244
5	0.709 (4.89)	41.5 (286)	0.252
AVG	**0.718 (4.95)**	**41.3 (285)**	**0.251**
COV	**1.63%**	**4.32%**	**2.70%**

5.2.2 In-Plane 1-2 Plane Material Properties

To generate the in-plane i.e., the shear modulus, G_{12}, secant-intercept modulus, K_{12}, and exponent n_{12} are selected as the optimization variables, while all other material properties remain constant during the analysis. Only two to three iterations are needed to establish convergence of the optimization method for the SBS analysis for each specimen. Very little reduction in the objective function (Figure 33(a)) and parameter update (Figure 33(c)) is observed in each iteration indicating that the initial approximation used in the SBS FEM analysis is near optimal. Note that the value of the initial objective function is of the order 10^2, whereas for the 1-3 plane, the initial objective function is of a higher order (typically 10^3). Very little change in maximum strain error (Figure 33(b)) in each iteration is also observed.

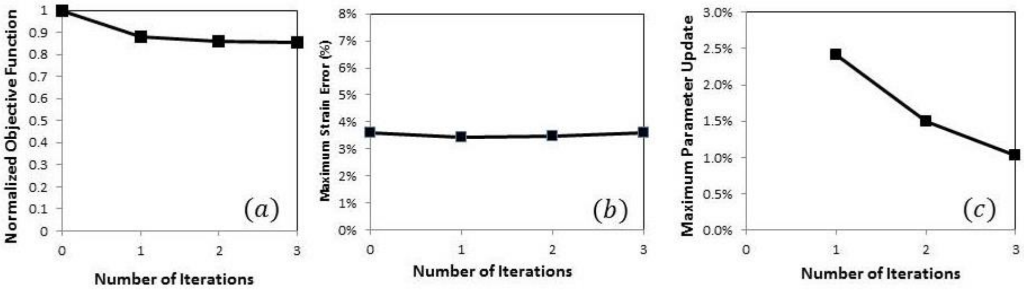

Figure 33**.** The (a) normalized objective function, (b) maximum RMS strain error, and (c) the maximum parameter update in each iteration for a typical material specimen tested in the 1-2 principal material plane.

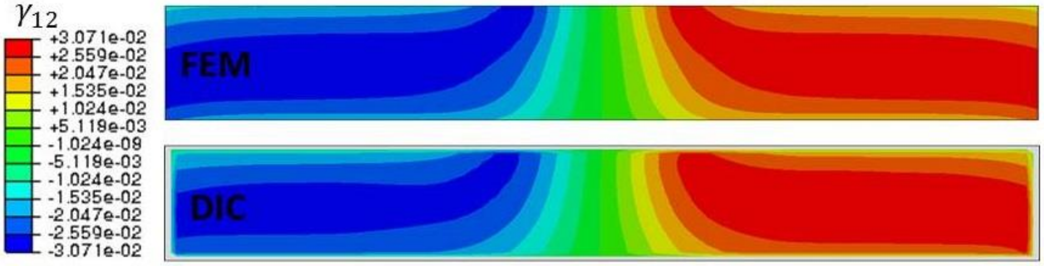

Figure 34. Comparison of the FEM-predicted and DIC-measured shear strain for a typical specimen tested in the 1-2 principal material plane at 67% failure load.

A typical comparison between the 1-2 FEM strains and DIC strains at 67% failure load is shown in Figure 34. Excellent agreement between the FEM-computed and the DIC-measured strains was found for all the specimens tested.

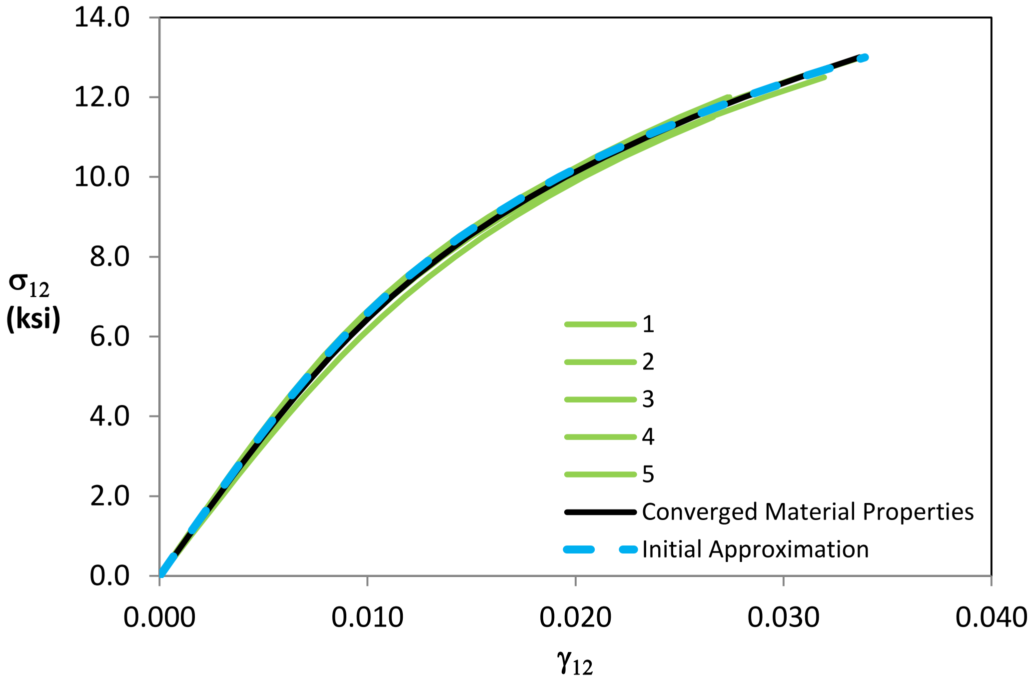

Figure 35. The converged shear stress-strain curves for the 1-2 principal material plane.

In Figure 35, the shear stress-strain curves for the 1-2 principal material plane are plotted versus the initial approximation of the material constitutive properties. It is evident that the optimal nonlinear behavior is very closely represented by the initial approximation used in the full-field FEM stress analysis. The converged material properties are presented in Table 7.

Table 7. Converged Material Properties for the 1-3 Principal Material Plane from SBS tests.

Specimens	G_{12}, Msi (GPa)	$K_{12,}$ ksi (MPa)	n_{12}
1	0.670 (4.62)	37.7(260)	0.255
2	0.750 (5.17)	36.7 (253)	0.252
3	0.713 (4.92)	38.5 (265)	0.256
4	0.726 (5.01)	36.8 (254)	0.256
5	0.714 (4.92)	38.8 (268)	0.258
AVG	**0.715 (4.93)**	**37.7 (260)**	**0.256**
COV	**3.62%**	**2.34%**	**0.75%**

5.2.3 Interlaminar 2-3 Plane Material Properties

Using the SBS method, only the linear shear modulus, G_{23} can be determined. In the optimization algorithm, G_{23} is selected as the optimization variable and all other material parameters are held constant. Two to three iterations are required to reach the optimal material relation. In Figure 36 (a) to (c), the normalized objective function, maximum RMS strain error and maximum parameter update are plotted for a typical 2-3 SBS full-field specimen.

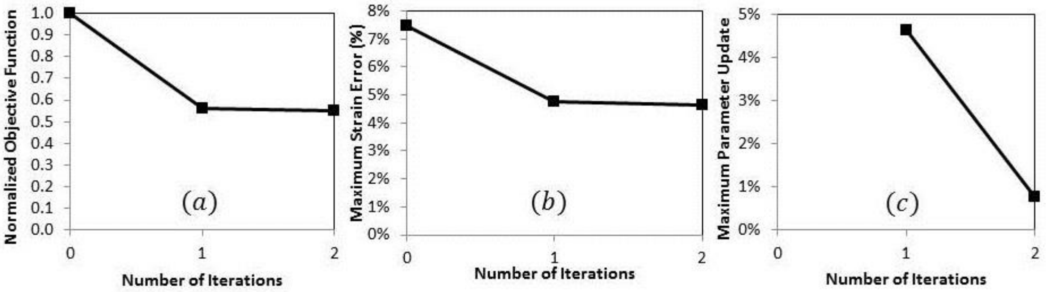

Figure 36. The (a) normalized objective function, (b) maximum RMS strain error, and (c) the maximum parameter update in each iteration for a typical material specimen tested in the 1-2 principal material plane.

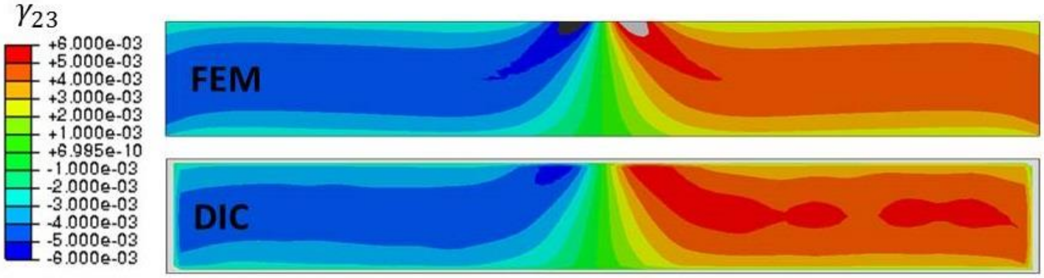

Figure 37. Comparison of the FEM-predicted and DIC-measured shear strain for a typical specimen tested in the 2-3 principal material plane at 95% failure load.

Figure 37 shows a typical comparison between the 2-3 FEM strains and DIC strains immediately before the specimen failure. Excellent agreement between the FEM-computed and the DIC-measured strains was found for all the specimens tested.

The converged shear stress-strain curves for the five specimens loaded in the 2-3 principal material plane are shown in Figure 38. The initial approximation of the linear shear model, as well as the average of the converged material properties, are shown for comparison. A summary of the linear shear modulus values for each specimen is given in Table 8. The average converged linear shear modulus found from the full-field FEM analysis differs from the initial guess by only 3.6%.

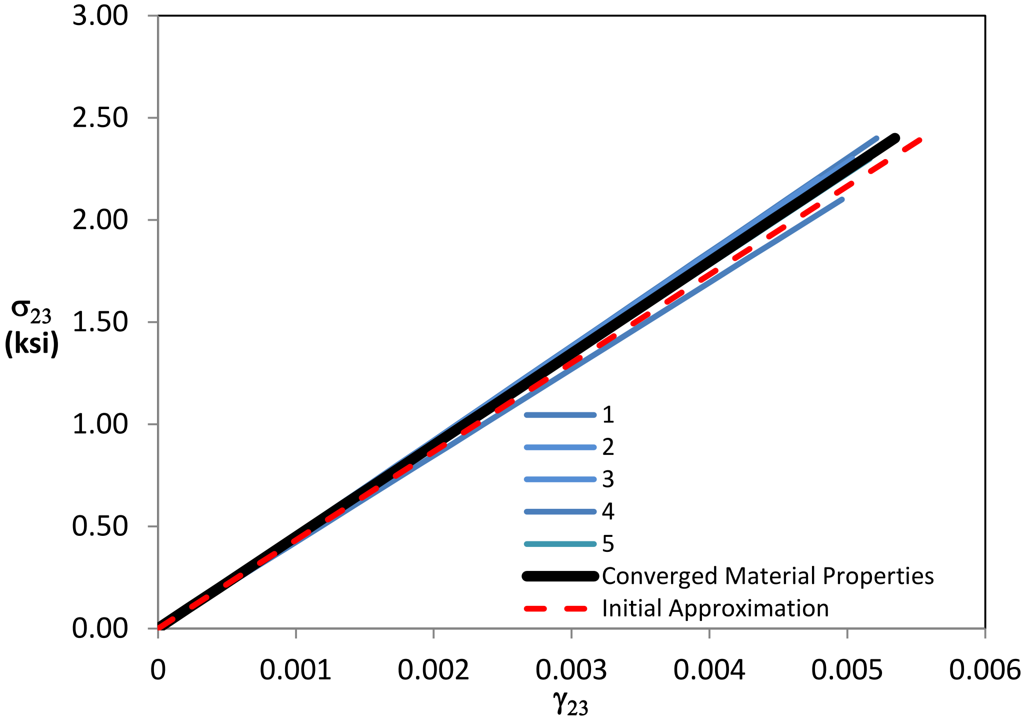

Figure 38. The converged stress-strain curves for the 2-3 principal material plane.

Table 8. Converged Material Properties for the 2-3 Principal Material Plane from SBS Tests

Specimens	G_{23}, Msi (GPa)
1	0.461 (3.18)
2	0.459 (3.16)
3	0.457 (3.15)
4	0.423 (2.92)
5	0.445 (3.07)
AVG	**0.449 (3.10)**
COV	**3.09%**

To complete the initial approximation of the material constitutive model for the nonlinear shear behavior for the FEM-based stress analysis of the small-plate torsion specimen, the secant-modulus K_{23}, and exponent, n_{23}, will initially be assumed to be the same as the 1-3 nonlinear parameters.

5.3 Material Characterization Using Small-Plate Torsion Specimens

The optimization is performed on each plane, simultaneously, for the small-plate torsion specimens. A 0.1% maximum relative change in parameter update was used as stopping criterion for the iterative L-M procedure, as defined in expression (18). Four or five iterations are typically required to establish convergence for the optimization model.

In Figure 39 (a) to (c), the values of the normalized objective function , the total RMS normalized error in maximum shear strain between DIC-measured and FEM-computed strains, and the maximum error in parameter update at each iteration of the full-field optimization for a typical torsion specimen are shown, respectively. The normalized objective function is defined as the ratio of the objective function given in equation (10) at the current iteration by the objective function at the first iteration (equation 19). The RMS normalized error in maximum shear strain is computed as in equation (22) for all three principal material planes together.

$$\varepsilon_{RMS} = \sqrt{\frac{1}{3N}\sum_{i=1}^{3N}\left(\frac{\varepsilon_{max_i}^{DIC}-\varepsilon_{max\,i}^{FEM}}{\varepsilon_{max_i}^{DIC}}\right)^2}. \qquad 22$$

The maximum error in parameter up date is defined in expression (18).

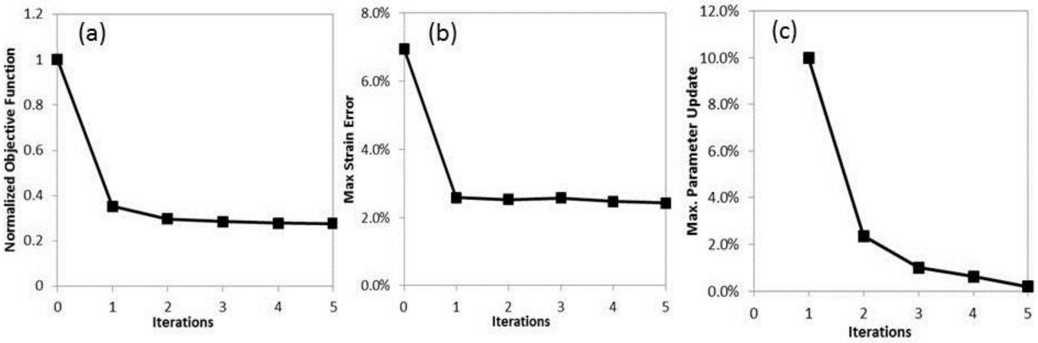

Figure 39. (a) The normalized objective function, (b) the maximum normalized strain error, and (c) the maximum error in parameter update at each iteration of the full-field L-M optimization procedure for a typical small-plate torsion specimen.

A rapid decrease of the objective function, maximum RMS strain error and the update in parameters has been demonstrated for the first iterations. The total RMS maximum strain error is reduced from 7% for the initial approximation of the material parameters to less than 2.5% for the converged constitutive properties. Figures 40 through 42 show the resulting update of the shear stress-strain relations in the three material planes for the typical specimen selected. It is shown that most of the reduction of the objective function and the error in maximum shear strain comes from the update of the shear properties in the 1-2 material plane, as the parameters are mostly unchanged from the initial approximation in the 1-3 and 2-3 material planes.

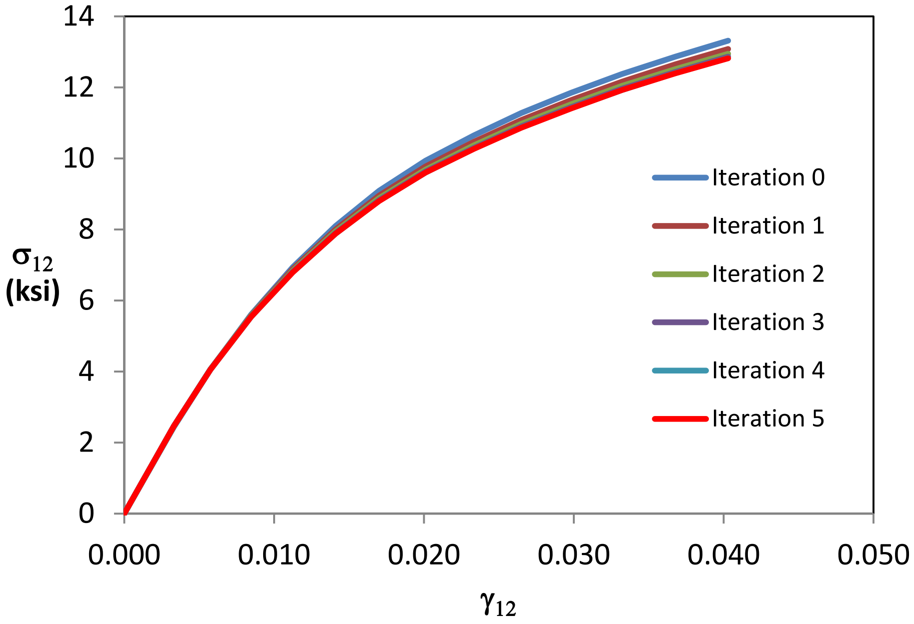

Figure 40. Full-field optimization of the shear stress-strain curves of a typical small-plate torsion specimen in the 1-2 principal material plane.

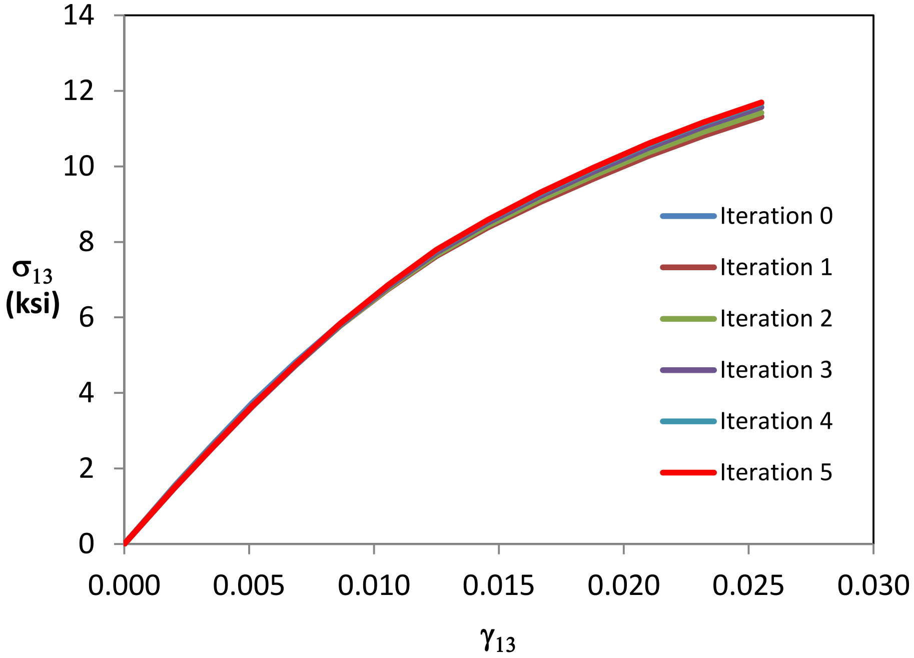

Figure 41. Full-field optimization of the shear stress-strain curves of a typical small-plate torsion specimen in the 1-3 plane principal material plane.

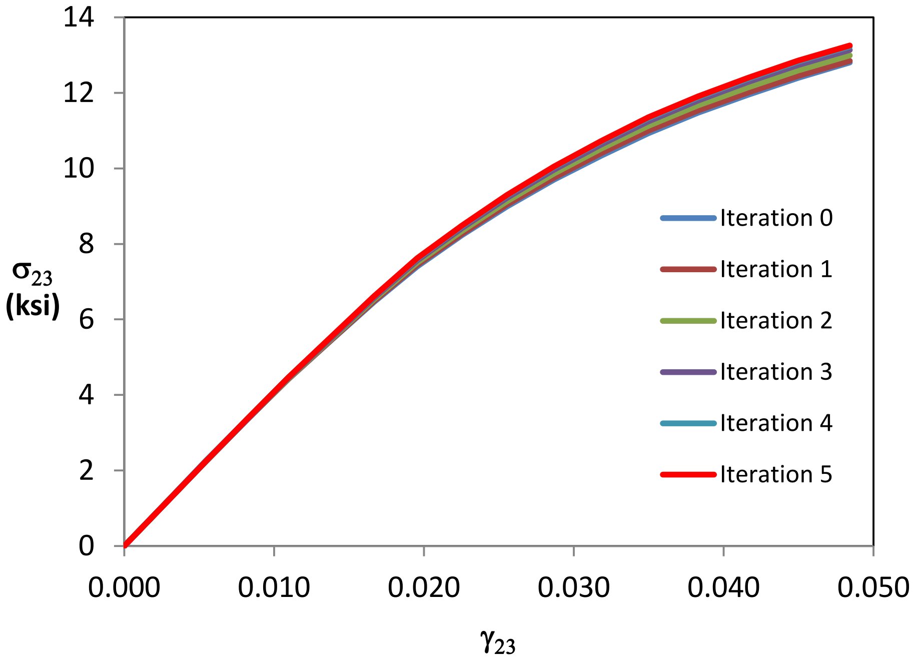

Figure 42. Full-field optimization of the shear stress-strain curves of a typical small-plate torsion specimen in the 2-3 principal material plane.

Convergence of the stress-strain curves with the number of load steps *N* at which DIC images are generated and used for full-field strain optimization is illustrated in Figure 43. Figure 43 shows the RMS normalized error in stress values for the stress-strain curves using different numbers of load steps,equally spaced throughout the loading history, compared to the converged response obtained using 20 load steps.

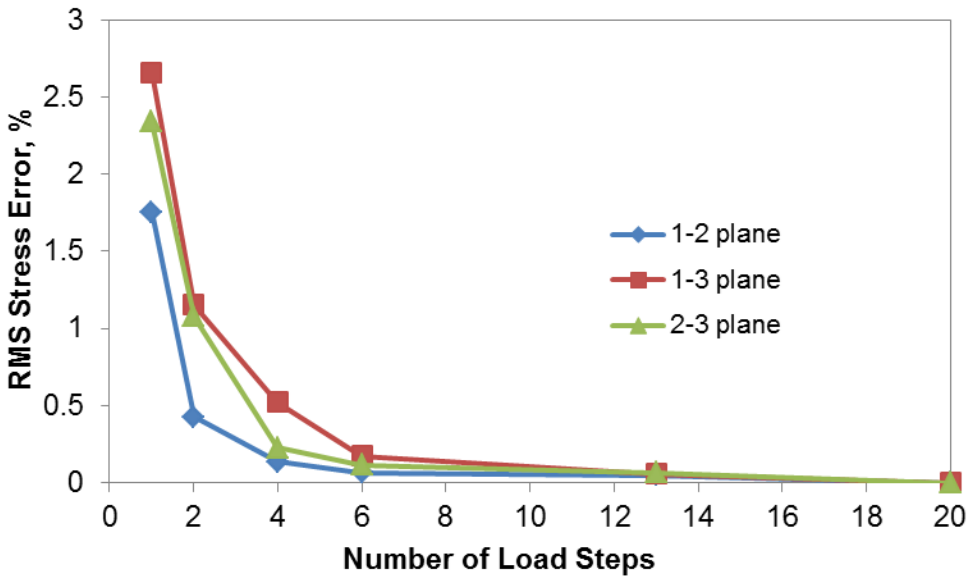

Figure 43. Convergence of the nonlinear shear stress-strain relations in the three principal material planes with the number of load steps used in the full-field optimization.

The maximum RMS error is only 2.7% when a single DIC image (corresponding to the maximum load) is used per plane and a rapid convergence is observed. This is related to the fact that a single full-field DIC-strain measurement at maximum load includes strain values spanning linear to fully nonlinear range as shown in Figure 26, which allows for simultaneous extraction of linear and nonlinear material parameters. Computational time until convergence of the inverse procedure using 20 DIC images is approximately 120 minutes using 12 processors for the FEM solver, whereas only 15 minutes are required when one DIC full-field measurement is used. The previous method developed in Chapter 3 was based on the measurement of the maximum shear strain only and therefore, required a significant number of DIC measurements for complete assessment of the nonlinear shear stress-strain material response.

The proposed method was verified by evaluating its robustness using different initial approximations of the nonlinear shear properties. Figures 44 through 46 show the converged stress-strain curves obtained for a typical specimen, starting from two different initial approximations A and B of the material parameters, as illustrated. For reference, approximations A and B are given in Table 9.

Table 9. Initial Approximations A and B of the Shear Nonlinear Constitutive Properties Used to Evaluate Robustness

Approximation A	$G_{12} = G_{13} = 0.590\ Msi\ (4.07\ GPa)$ $G_{23} = 0.347\ Msi\ (2.39\ GPa)$ $K_{12} = K_{13} = K_{23} = 32.5\ ksi\ (0.224\ GPa)$ $n_{12} = n_{13} = n_{23} = 0.248$
Approximation B	$G_{12} = G_{13} = 0.885\ Msi\ (6.10\ GPa)$ $G_{23} = 0.519\ Msi\ (3.58\ GPa)$ $K_{12} = K_{13} = K_{23} = 39.7\ ksi\ (0.274\ GPa)$ $n_{12} = n_{13} = n_{23} = 0.248$

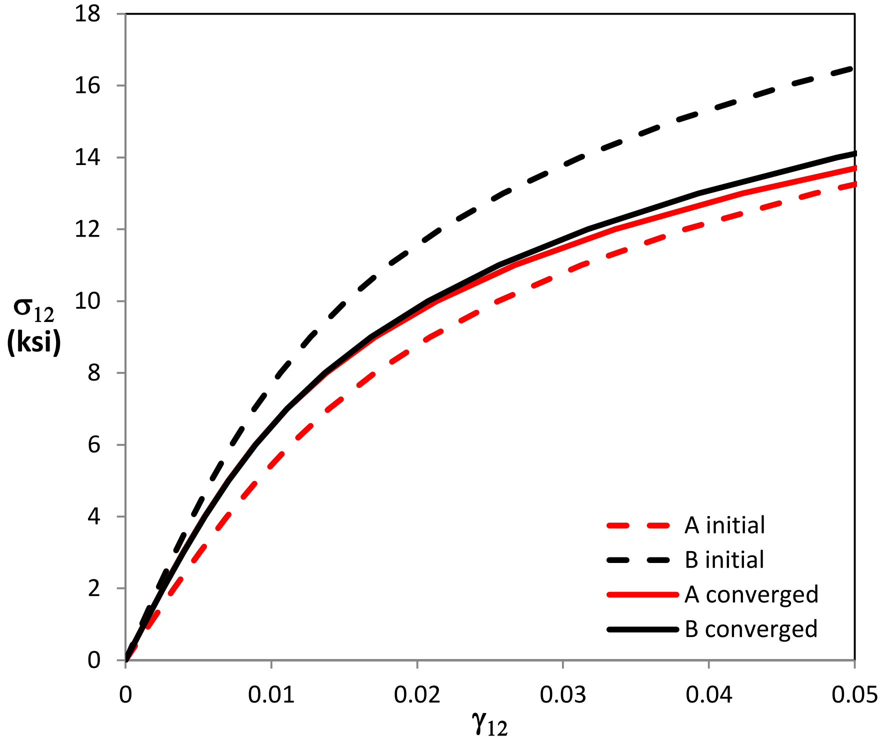

Figure 44. Converged shear stress-strain curves obtained from two different initial approximations A and B in 1-2 principal material plane.

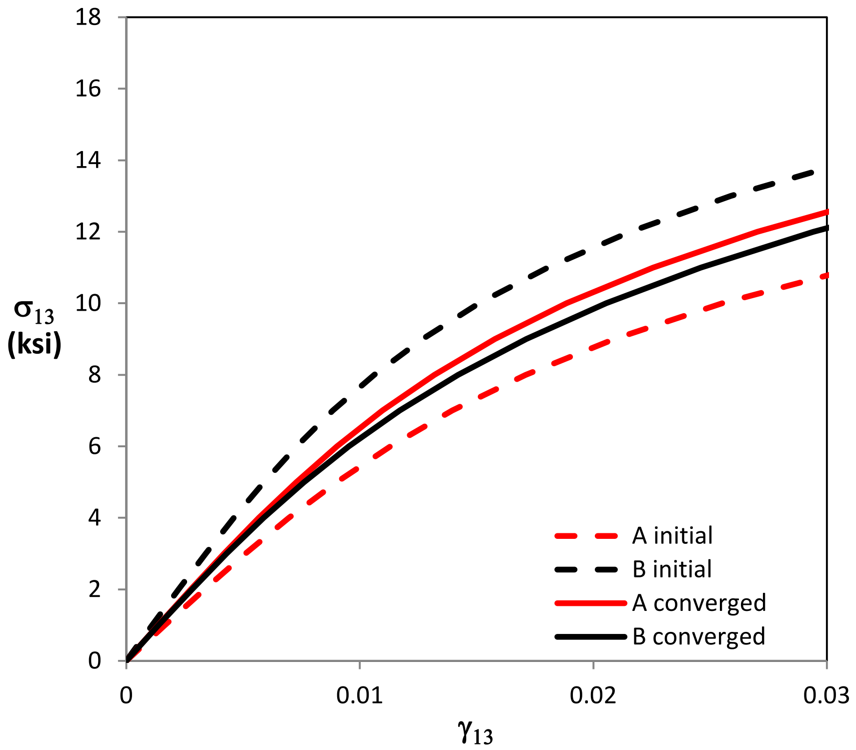

Figure 45. Converged shear stress-strain curves obtained from two different initial approximations A and B in the 1-3 principal material plane.

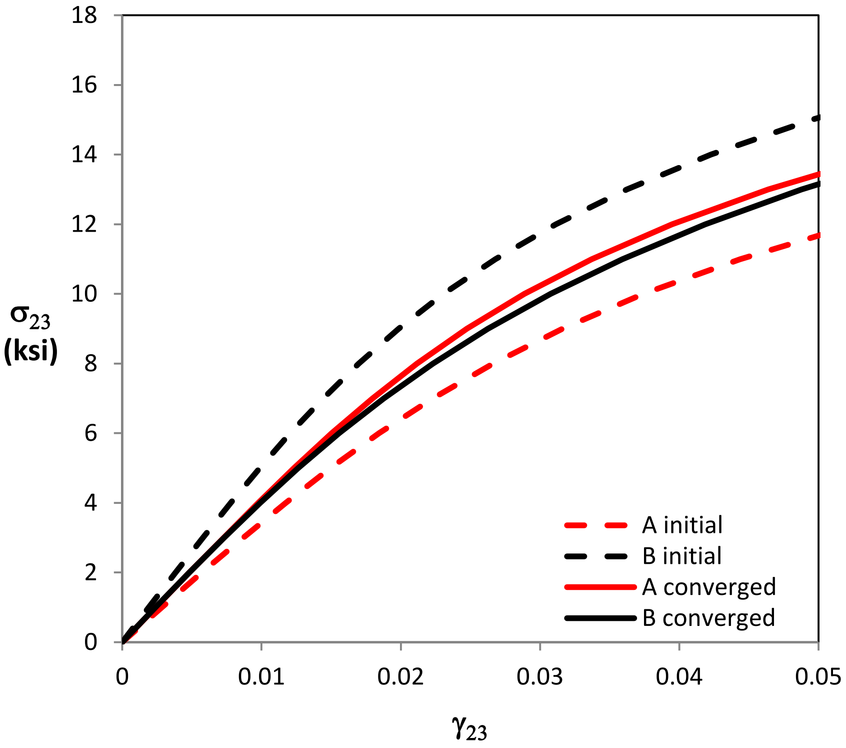

Figure 46. Converged shear stress-strain curves obtained from two different initial approximations A and B in the 2-3 principal material plane.

Convergence is obtained after five iterations for approximation A and six iterations for approximation B. The converged models for the nonlinear behavior in the three material planes obtained from both initial approximations are in very good agreement and also closely match the converged solution obtained from the SBS initial properties. The maximum RMS normalized error in stress values between the two converged solutions and with the converged model from the SBS initial approximation is less than 1.8% for the three planes.

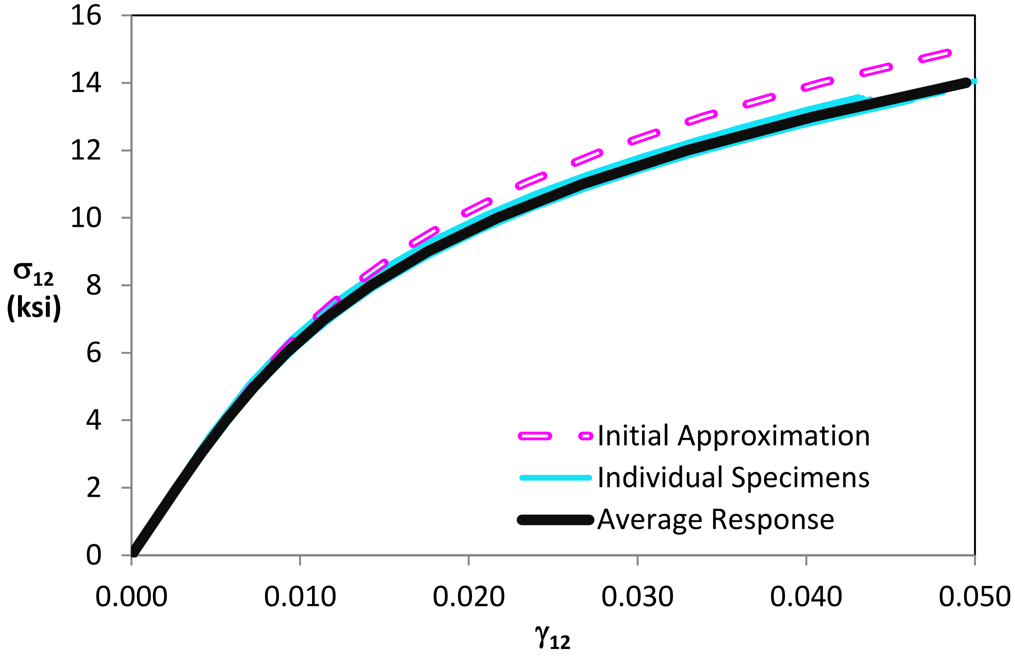

Figure 47. Initial approximation, individual stress-strain curves, and average response for the 11 IM7/8552 specimens in the 1-2 principal material plane.

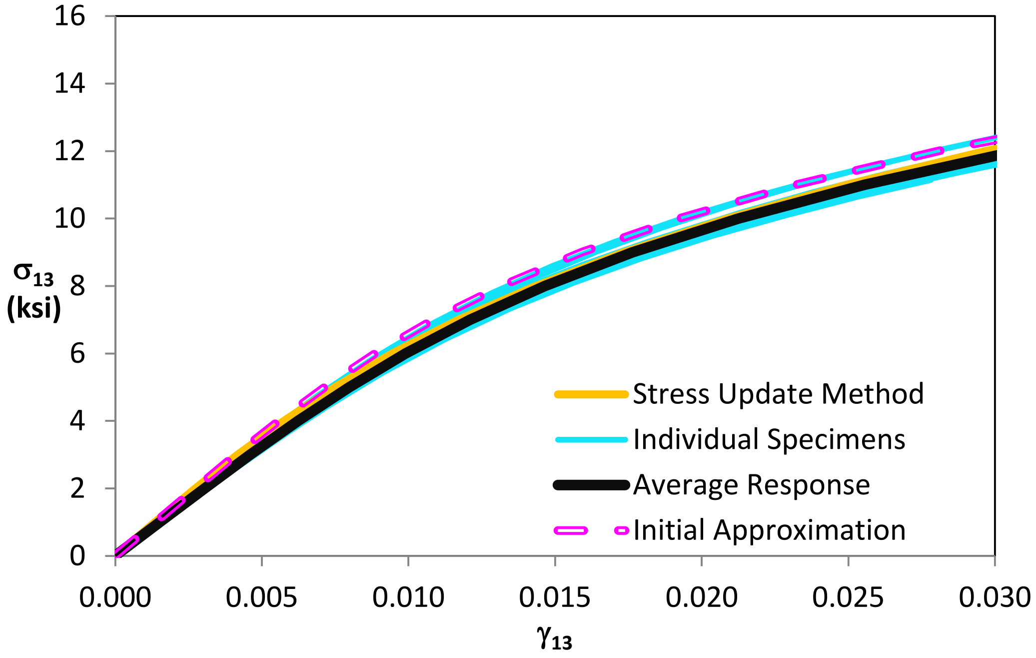

Figure 48. Initial approximation, individual stress-strain curves, and average response for the 11 IM7/8552 specimens in the 1-3 plane.

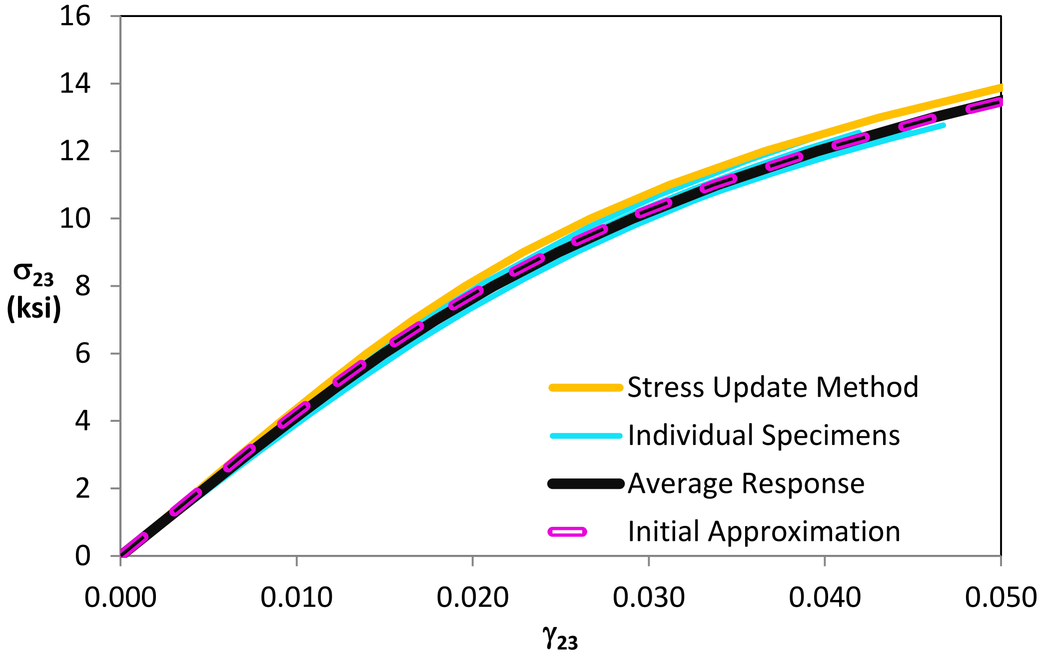

Figure 49. Initial approximation, individual stress-strain curves, and average response for the 11 IM7/8552 specimens in the 2-3 plane.

Table 10. Nonlinear Shear Properties for the Small-Plate Torsion Specimens

Specimen	G_{12}, Msi	K_{12}, ksi	n_{12}	G_{13}, Msi	K_{13}, ksi	n_{13}	G_{23}, Msi	K_{23}, ksi	n_{23}	Max strain error
1	0.747	34.4	0.255	0.685	36.8	0.246	0.421	36.0	0.247	2.20%
2	0.754	34.2	0.257	0.645	36.0	0.255	0.413	36.4	0.244	2.40%
3	0.732	33.9	0.258	0.702	35.7	0.253	0.424	35.4	0.249	2.00%
4	0.790	34.2	0.255	0.661	36.5	0.25	0.395	36.7	0.244	3.20%
5	0.759	34.2	0.256	0.638	35.7	0.255	0.424	36.0	0.247	1.50%
6	0.773	34.1	0.256	0.715	36.5	0.249	0.413	36.4	0.246	3.00%
7	0.728	34.1	0.258	0.650	35.8	0.251	0.419	36.1	0.244	2.10%
8	0.734	34.2	0.257	0.641	35.8	0.254	0.422	36.5	0.243	2.20%
9	0.716	35.0	0.254	0.635	36.7	0.248	0.429	36.8	0.24	2.60%
10	0.732	34.1	0.258	0.640	35.8	0.255	0.426	36.1	0.245	2.20%
11	0.730	34.4	0.257	0.645	35.7	0.254	0.425	36.3	0.244	2.20%
AVG	0.745	34.3	0.256	0.660	36.1	0.252	0.419	36.2	0.245	
COV	2.84%	0.74%	0.51%	4.03%	1.20%	1.21%	2.17%	1.06%	0.93%	

Converged shear stress-strain curves obtained for 11 IM7/8552 specimens are presented in Figures 47 through 49 and compared with the initial approximation of the shear response. For the 1-3 and 2-3 principal material planes, the average response determined by the stress update method in Chapter 3 are also plotted for comparison. Thirteen DIC images taken at load steps, equally spaced throughout the loading history, are used for extraction of the material properties. Nonlinear shear properties obtained for all specimens are summarized in Table 10 [55, 56]. Table 10 also lists the average value of the parameters with the associated COV and the RMS error between DIC and FEM strains at the maximum shear strain location for all planes.

The scatter in the log-linear parameters *G,K,* and *n* is small for the three principal planes, as indicated by lower than 4.03% COV, with the maximum variability in the G_{13} shear modulus. Excellent agreement between FEM-strains for the converged solution and DIC-strains is demonstrated by lower than 3.2% total RMS error for the maximum shear strains in each material plane.

It is found that the linear portion of the shear stress-strain response in the 1-2 plane agrees well with the initial approximation from SBS results, with less than 1% error on the average shear modulus value. As strains become larger, the converged small-plate torsion, stress-strain response deviates from SBS results in the nonlinear regime, with about 6.5% relative error in average shear stress at maximum strains. The deviation of the nonlinear shear response in the nonlinear regime for the 1-2 principal material plane might be due to the effects of material coupling in the nonlinear stress-strain regime [7], which will be discussed in the next chapter. Reasonable agreement is found between the SBS approximation and the shear stress-strain curve obtained from the full-field optimization method for the 1-3 interlaminar plane, with less than 5% of relative stress error at maximum strain between the average response and the SBS approximation. The error mostly comes from the shear modulus G_{13}, with an average modulus about 9.6% lower than the results of the SBS. Note that the SBS and small-plate torsion specimens were manufactured years apart by different companies from different batches of prepreg. Therefore, the difference in the SBS results could be attributed to the effects of the material process variabilities. The average converged shear stress-strain curve obtained for the 2-3 plane closely matches the initial approximation and exhibits low scatter. This is an interesting result, suggesting that the nonlinear shear stress-strain response in the 2-3 plane can be accurately assessed by using the transverse isotropy approximation for the shear modulus and the *K* and *n* parameters obtained from characterization of the shear nonlinear behavior in the 1-3 plane.

Shear stress-strain relations are in close agreement with the results obtained in the work for carbon/epoxy IM7/8552 material and were used in a recent work by Seon et al for FEM-based predictions of static and fatigue failure in a 68-plies thick laminated structural element [60]. Accurate representation of the shear stress-strain nonlinearity was critical for prediction of delamination initiated by large interlaminar shear-stress gradients present at the location of seeded manufacturing defects. Further validation of the shear constitutive material properties generated in this work for IM7/8552 was shown by the excellent correlation between FEM failure predictions and experimental data in Reference [60].

5.4 Comparison of Nonlinear Shear Models

The log-linear Ramberg-Osgood model has been used as it is a relatively simple expression that can model the nonlinearity in stress-strain relations with good accuracy and flexibility. It is important to note that the Ramberg-Osgood equation is widely accepted for characterizing nonlinear behavior in composite materials [30]; however other material response approximations such as higher order polynomial [61] or piece-wise linear fit of the data could also be used [62]. In Figures 50 through 52, the converged stress-strain curves obtained using the Ramberg-Osgood model are compared with a 3rd order polynomial and a 5th order polynomial.

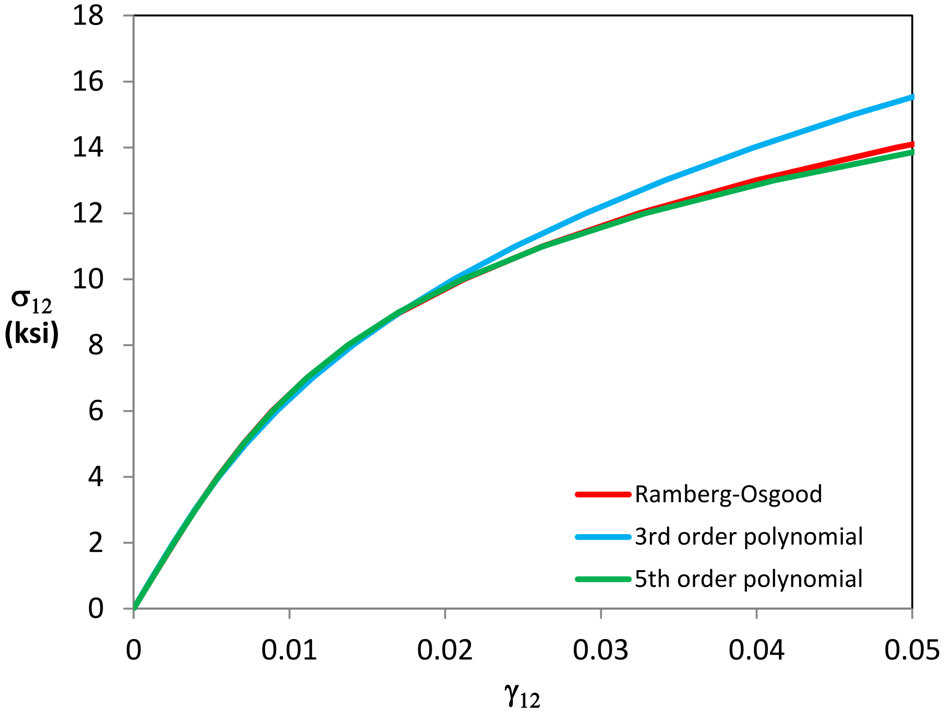

Figure 50. Converged stress-strain curves using different approximations of the shear stress-strain behavior for the 1-2 plane.

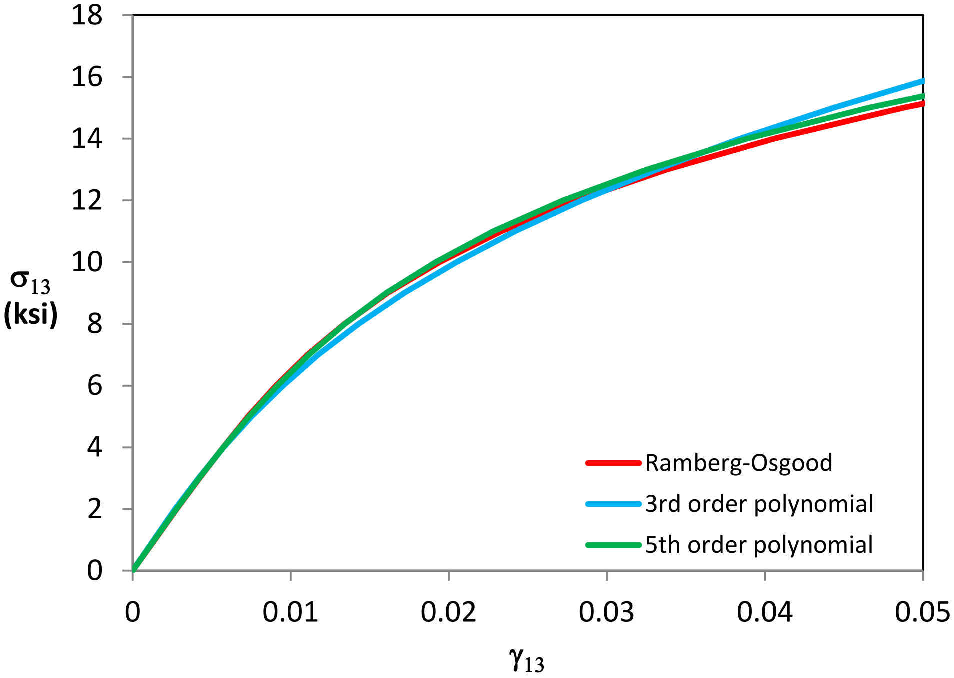

Figure 51. Converged stress-strain curves using different approximations of the shear stress-strain behavior for the 1-3 plane.

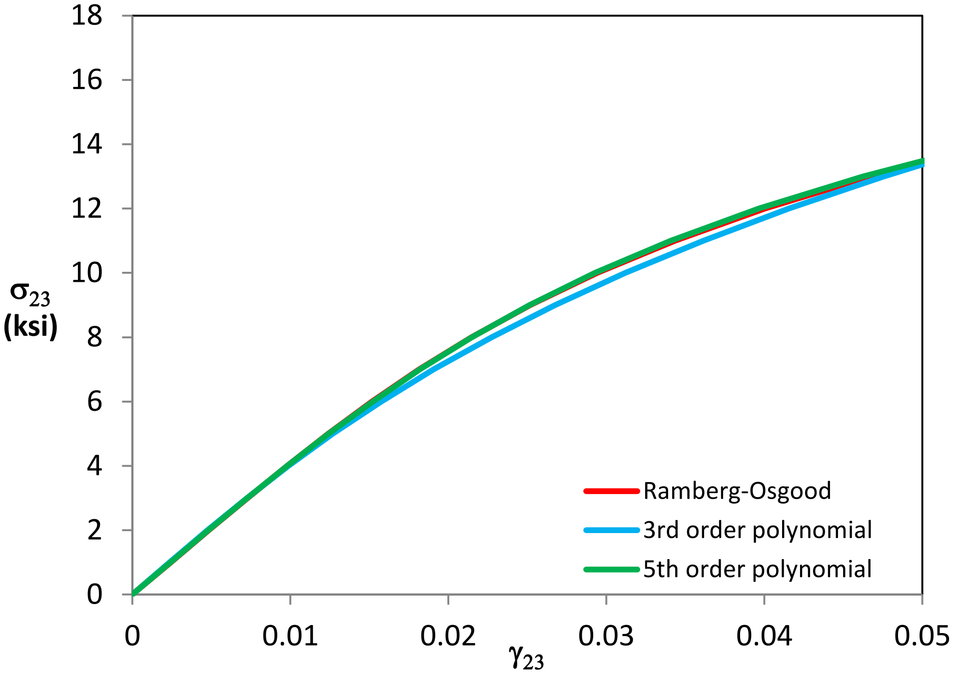

Figure 52. Converged stress-strain curves using different approximations of the shear stress-strain behavior for the 2-3 plane.

As shown in Figures 50 through 52, the stress-strain curves in all material planes obtained using the 5th order polynomial model are almost identical to the results from the Ramberg-Osgood model. For the 3rd order polynomial approximation, a maximum deviation of approximately 9% in stress values at maximum strain is found in the 1-2 plane. Less deviation is found in the other planes; however a discrepancy is visible in the nonlinear regime.

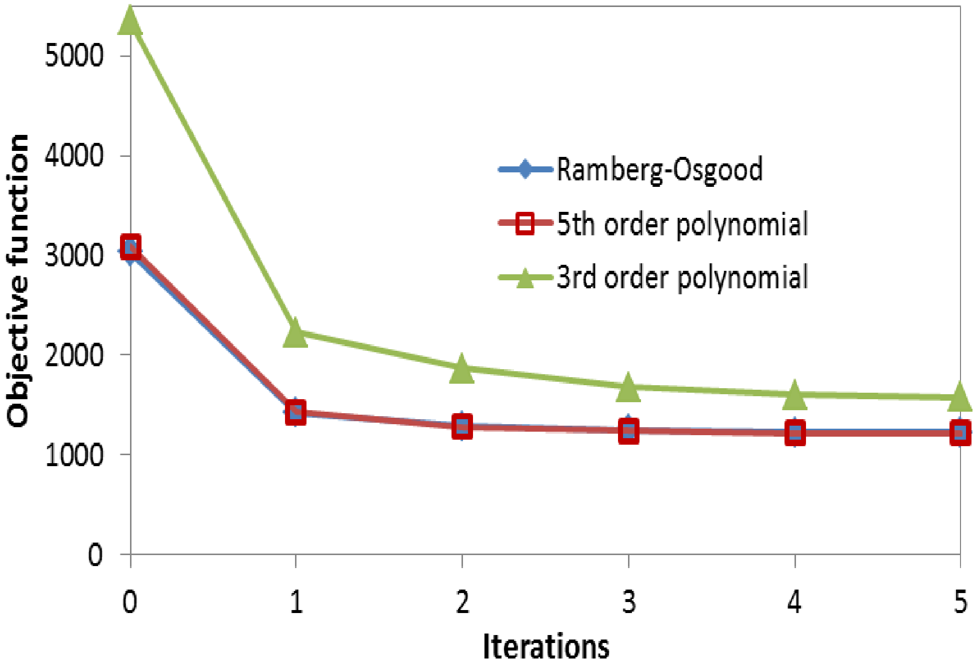

Figure 53. Evolution of the objective function for different approximations of the nonlinear shear stress-strain behavior.

In Figure 53, the values of the objective function for the 3 models at each iteration have been plotted. As expected the Ramberg-Osgood and 5th order polynomial models lead to similar values of the objective function; however, the 3rd order polynomial approximation gives a higher value of the objective function. That is, the Ramberg-Osgood and the 5th order polynomial are better approximations of the material behavior, allowing for better correlation with DIC-measured strains. The excellent agreement in stress-strain curves between the Ramberg-Osgood and 5th order polynomial model give confidence that the curve represents the actual material response and is not the product of a curve-fitting exercise.

Physics-based models, if available, should always be preferred to simple curve-fitting expressions, as they ensure that the model is not dependent on the test configuration. In the case of composite materials, it is well known that the stress-strain response is linear elastic at low strains. Other useful approximations in linear regime include orthotropic and transverse isotropic behavior, due to the intrinsic properties of composites. The Ramberg-Osgood model includes a linear term for the representation of the shear response at lower strains. However, limited knowledge is available for the description of the nonlinear behavior of composites at larger strains, including the nonlinear shear behavior. Complex phenomena such as microfailures, creep, or material couplings for which underlying physics are not yet fully understood, might occur. When a physics-based model is not available, a simple expression with enough flexibility to fit the data with acceptable accuracy should be considered. The Ramberg-Osgood model meets the requirements for simplicity and flexibility. It allows for accurate representation of the shear behavior, as demonstrated by excellent agreement between FEM-strains for the converged solution and DIC-strains, with lower than 3.2% total RMS error for maximum shear strains in each material plane. Finally, very good agreement was found between the SBS test results and the small-plate torsion method using Ramberg-Osgood model for the shear response in the 1-3 principal material plane, proving that the Ramberg-Osgood approximation is not test configuration dependent. These arguments are the basis to justify the use of the Ramberg-Osgood expression for representation of the shear behavior of carbon/epoxy composite material considered in this work.

The derivation of the most accurate constitutive model without any *ad hoc* assumptions for representation of the material behavior up to failure, including nonlinearity and couplings, is not addressed in this work and is the subject of ongoing research by researchers at the Advanced Materials and Structures Laboratory at the University of Texas at Arlington.

Chapter 6

Material Coupling

One of the main advantages of a full-field strain measurement method is that all components of strain are measured within the area-of-interest. This coupled with three-dimensional FEM results in the opportunity to investigate the interactions between all stress components and the shear relations.

In developing the failure criterion for matrix cracking due to a combined transverse tensile load and in-plane shear, Camanho et al [63], recognize the effect of transverse stresses on the shear stress-strain curves, first discussed by Puck and Schürmann [7]. The usual assumption is that the in-plane shear stress-strain curve will be unaffected by the superposition of axial stress, σ_{11}, transverse normal stress, σ_{22}, and in-plane shear stress, σ_{12}; however, experimental results show that the addition of transverse tensile stresses of the same order as the in-plane shear have noticeable effects on the shape of the shear stress-strain curve. The microdamage within the matrix caused by a tensile σ_{22} leads to a reduction in the shear stress-strain curve as shown in Figure 54, whereas a compressive σ_{22} leads to a slight stiffening in the large nonlinear strain regime. Figure 54 is a reproduction of data published in Ref [7].

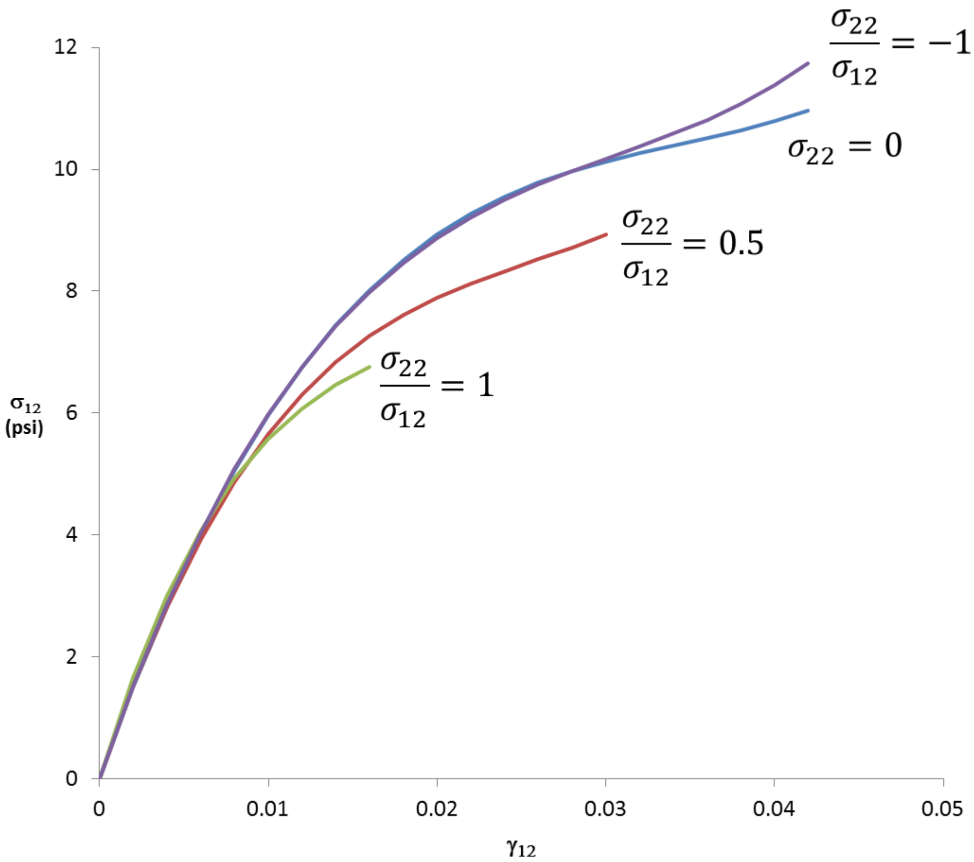

Figure 54. The effect of transverse tension and compression on the in-plane shear stress-strain curve as investigated Puck and Schürmann [7].

It is recognized in both works that in order to accurately understand the material behavior, this interaction between transverse stresses and in-plane shear needs to be accounted for in the constitutive model [7, 63]. It was found in [61] that failure to account for this coupling led to errors in predicting crack initiation.

In this work, full-field plots of the shear stress-strain behavior can be used to investigate couplings in the nonlinear shear range. Previous works have focused only on the 1-2 in-plane shear coupled with transverse tension and compression. SBS specimens exhibit high compressive stresses as well as high shear stresses in regions under the loading nose or above the supports. Despite the strong evidence that couplings exist [61], they have not been accounted for in the material model. Determining the constitutive model to generalize the stress-strain data may be challenging because the relationship describing the effect of transverse compression on the shear may not be obvious.

Figure 55 shows the full-field, shear stress-strain curves for SBS specimens tested in the 1-2 principal material plane. The points on the curve are colored according to the value of the axial,(a) σ_{11}, and transverse compressive, (b) σ_{22}, stresses at that point. Minimal scatter is observed in the full-field stress-strain curves. In regions exhibiting high transverse compression, there is little to no effect on the stress-strain curve as compared to regions with negligible transverse compression. Likewise, little effect on the shear stress-strain curve can be attributed to regions of high axial stresses (either tension or compression).

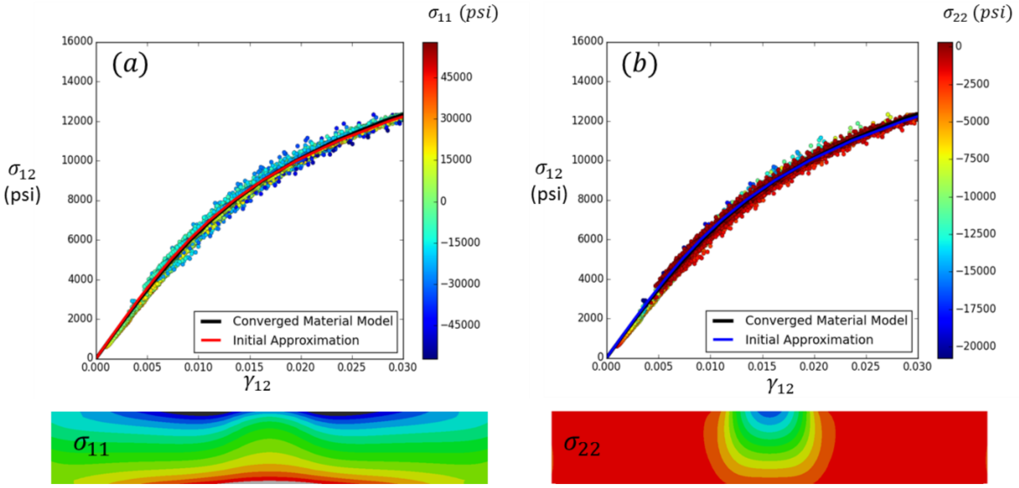

Figure 55. Color plots of the in-plane shear stress-strain data obtained from FEM-calculated stresses and DIC-measured strains using the axial (a) and transverse (b) normal stress distribution for an SBS specimen tested in the 1-2 plane.

For specimens tested in the 1-3 interlaminar principal plane, the full-field plots exhibit much more scatter than those tested in the 1-2 plane. Figure 56 shows the full-field, shear stress-strain plots for the 1-3 plane with the points colored according to the axial, (a) σ_{11}, and through-thickness stresses,(b) σ_{33}, at that location. Some noise in the DIC data is expected, but strong correlation between high values of σ_{11} and σ_{33} lead researchers to believe that this cannot only be attributed to noise. Regions corresponding to the midpoint between the loading nose and support fall directly along the curve corresponding to the “Converged

Material Properties”, whereas points underneath the loading nose move away from the average response curve. Correlation with regions of high compressive, σ_{11}, is also observed.

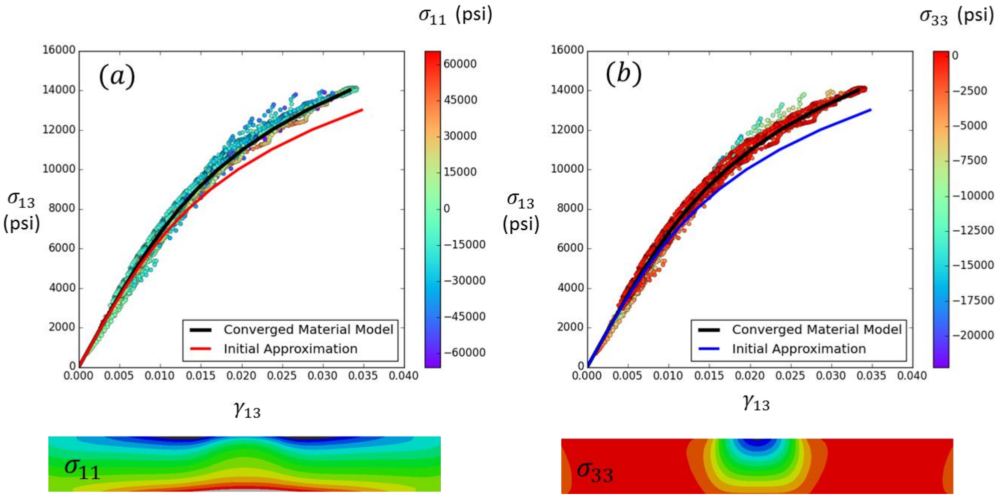

Figure 56. Color plots of the shear stress-strain data obtained from FEM-calculated stresses and DIC-measured strains using the axial (a) and through-thickness (b) normal stress distribution for an SBS specimen tested in the 1-3 plane.

By varying the span-to-thickness ratio, loading nose/support diameter, and specimen dimensions for an SBS specimen, all failure modes (tension, compression, and shear) can be achieved and a full range of strain components can be generated up to material failure. Specifically, looking at specimens that fail in compression should exhibit higher levels of through-thickness compressive stresses before failure and would generate more information to assess the effect of through-thickness normal stress on the shear stress.

Multi-axial stress distribution on the top surface of the small-plate torsion specimen is due to the combination of twist and bending deformation. Such distribution allows for investigation of material coupling among shear, axial, and transverse modes in the nonlinear regime by using the full-field strain measurement capability of the DIC technique and FEM-based stress calculation.

Typical in-plane shear, axial and transverse stress fields on the observation window of the 1-2 principal material plane of the small-plate torsion specimen at maximum load before failure (around 540 lb (2,400 N)) are shown in Figure 57. As illustrated, high transverse and axial stress gradients due to bending are observed in the region corresponding to the support contact surface on the other side. In-plane shear stress distribution is uniform over most of the surface and rapidly reaches the nonlinear regime, around 30% of the failure load.

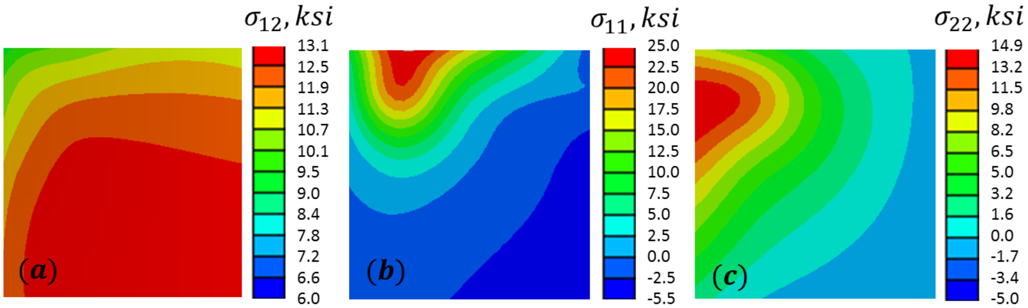

Figure 57. Stress distribution in the observation window of the 1-2 principal material plane of the small-plate torsion test specimens for (a) σ_{12}, (b) σ_{11}, and (c) σ_{22} stresses at maximum load before failure.

In the two other principal material planes (1-3 and 2-3 planes), axial and transverse stresses are negligible in regions with high shear stress. Therefore, investigation of material coupling in this shear response is limited to the 1-2 principal material plane for the test configuration considered in this work.

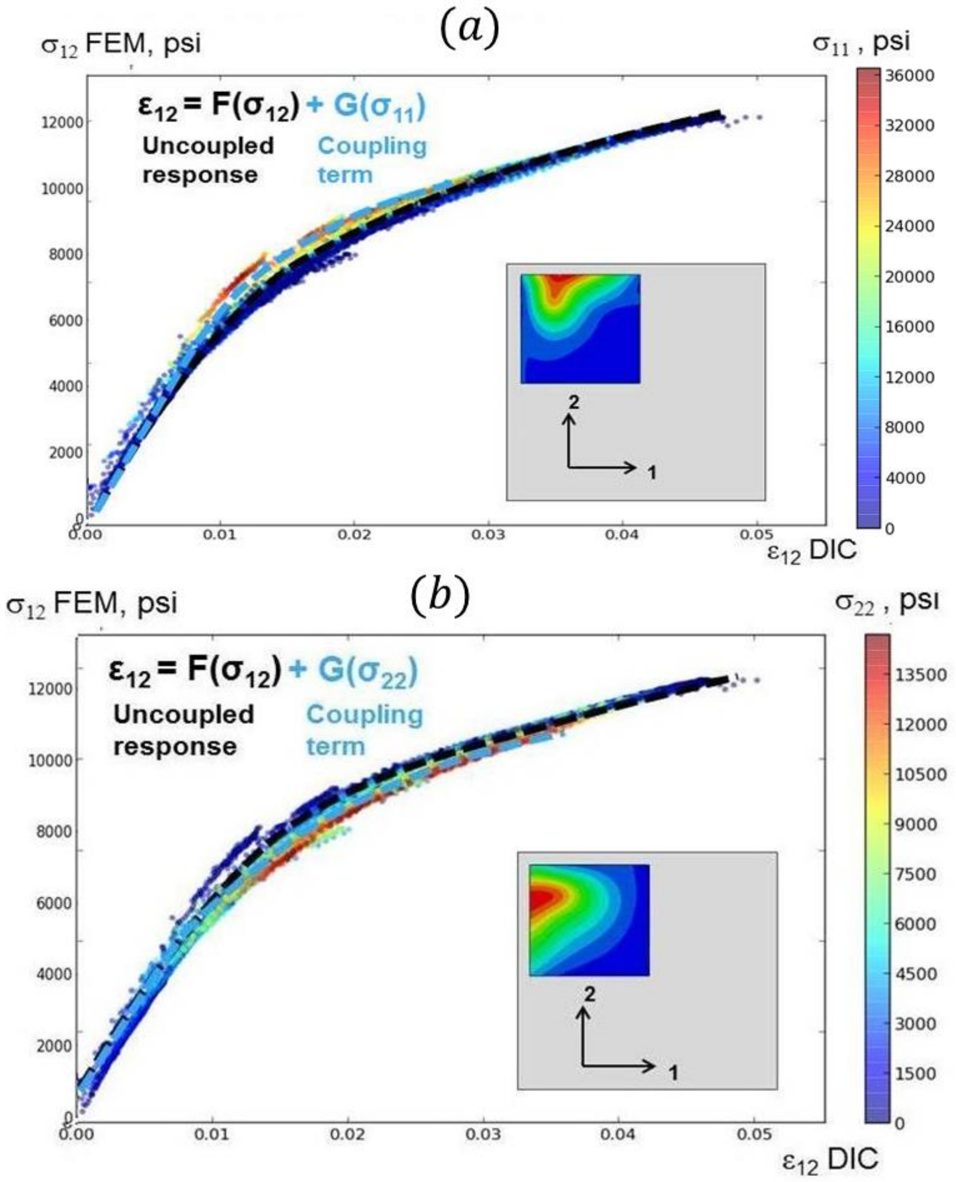

Figure 58. Color plots of the in-plane, shear stress-strain data obtained from FEM-calculated stresses and DIC-measured strains using the axial (top) and transverse (bottom) normal stress distribution in the observation window for the 1-2 principal material plane.

In Figure 58, FEM-based, in-plane shear stress data for each node in the observation window is plotted versus the corresponding DIC-interpolated strain data for a typical specimen after full-field optimization of the shear material properties in all material planes. The stress-strain data points are colored based on the value of the axial and transverse stress component in the top and bottom charts, respectively, of Figure 58. For illustrative purposes, data from only five DIC images taken throughout the loading are presented. The shear stress-strain curve obtained from the full-field strain optimization model in the 1-2 plane is also plotted. Note that this model does not include any material coupling.

Scatter in the stress-strain data plotted in Figure 58 is expected, due to strain measurement errors. A total RMS error of 8.6% is found by comparing the stress-strain data from experimental strain measurement to the converged stress-strain curve of the optimization model. However, the scatter in shear strain is unlikely to be attributed to random measurement noise alone, as it appears to be spatially correlated with the axial stress distribution. It is shown that in areas with high-tensile axial stresses (Figure 58(a)), DIC-measured shear strains in the nonlinear regime are higher than expected from the uncoupled model. Such trend suggests the presence of material coupling among in-plane shear response and axial tensile stresses. It is shown in Figure 58(b) that data points corresponding to high-transverse tensile stress locations are lower than for the uncoupled shear stress-strain response of data points, consistent with the observations of Puck and Schürmann [7] for a ratio of transverse stress to shear stress equal to one. Therefore, it is suggested that a dependency exists between the in-plane shear response and transverse tensile stresses.

Chapter 7

Conclusions and Future Work

This work introduces a new method based on a small-plate torsion test which advances the state of the art of measuring 3D stress-strain material properties of composites, including the nonlinear stress-strain relations, using a single specimen. The method relies on DIC-based strain measurement and FEM-based stress analysis. A stress update method is first introduced, which determines the optimal material properties based on the convergence of the maximum FEM-based stress versus DIC-based strain curves. This method uses small regions of the full-field corresponding to the location of maximum stress/strain to determine the interlaminar properties. The interlaminar principal material planes are considered separately in this analysis method. The nonlinear shear stress-strain curves for the 1-3 plane closely matched those obtained from short-beam shear tests. To the best of the author’s knowledge this is the first characterization of the nonlinear shear stress-strain behavior of a unidirectional composite in the 2-3 material plane at all strain levels, including large shear strain.

A full-field optimization method is then developed, which takes complete advantage of the full-field measurement capability of DIC for a simultaneous assessment of nonlinear shear stress-strain relations for composites in all three principal material planes of a small-plate torsion specimen. This method advances the ability to measure 3D material properties compared to the stress update methodology that was able to use only small regions of the specimen surfaces approaching line segments or points. The resulting material stress-strain constitutive models rely on the DIC data including in-plane and out-of-plane strain components and on iterative FEM-based stress calculation with initial material property values generated from full-field SBS data. Results include the in-plane and two interlaminar stress-strain curves simultaneously captured for an IM7/8552 carbon/epoxy tape system.

Very good agreement was found between results obtained with the full-field optimization method and data generated from SBS tests in the 1-3 interlaminar plane. The linear-elastic material response in the 2-3 principal material plane confirm the accuracy of the transverse isotropic approximation for the 2-3 interlaminar shear modulus; and a practical approximation suitable for evaluation of the nonlinear shear properties in the 2-3 principal material plane was proposed. Investigation of material coupling in the 1-2 principal material plane suggested strong evidence of dependency of in-plane shear response on axial and transverse stresses. The slight deviation found between full-field strain optimization and SBS reference data in the 1-2 principal material plane might be explained if these material couplings were considered in the material model formulation. Further verification and identification of the coupling properties will be the focus of future work.

The complexity of the three-dimensional deformation exhibited by the small-plate torsion specimen and the ability of the method to capture multiple basic nonlinear, matrix-dominated, stress-strain properties in a single experiment advocate for assessing accurate 3D stress-strain relations for composites and verifying various simplifying assumptions. This method has a strong potential for becoming a platform for deriving basic nonlinear, stress-strain material, constitutive properties in three dimensions using a single specimen configuration and employing synchronized full-field strain measurement in three principal material planes.

After further developments, not only material properties for specific material systems, but also the material model formulation itself, can potentially be derived using an iterative updating process involving FEM-based simulations and DIC measurements. This would yield the most accurate constitutive model without any *ad hoc* assumptions for representation of the material behavior up to failure, including nonlinearity and couplings. Such methodology would enable accurate and efficient full three-dimensional characterization of nonlinear material properties of composites, using the minimum number of experiments, thus reducing the amount of material testing to understand complex properties governing deformation and failure.

The small-plate torsion method could be viewed as an extension of the short-beam method. The same unidirectional panel could be utilized to machine both specimen types; and both methods rely on DIC to measure deformation. Also, the stress-strain relations generated based on the short-beam shear method and supplemented with the transverse isotropic assumption fully expand the material constitutive model for FEM-based stress analysis of the small-plate torsion coupons to determine accurate nonlinear interlaminar material properties, including 2-3 shear stress-strain curve. A toolbox of DIC-based methods capable of assessing the fundamental material 3D stress-strain relations and the matrix-dominated strength characteristics using specimens machined from a single small unidirectional panel could be extremely useful for advancing the understanding of complex deformation and failure mechanisms of composites and improving the efficiency of characterizing material behavior.

While the small-plate torsion method has the ability to verify the accuracy of the transverse isotropic material assumptions (including nonlinear stress-strain behavior) for certain types of composite materials, it may not always be necessary to use this method for material characterization in addition to the short-beam method. The short-beam method uses less material and requires simpler stress analysis compared to the small-plate torsion method. Furthermore, a standardized test method should not involve complex FEM stress calculations as it is not practical for most test labs. Rather, this method should be used to establish the 3D material constitutive model and simplifying assumptions, which will lead to more efficient material characterization.

The current work has been focused on determining the 3D material constitutive model for IM7-carbon/8552 epoxy composite material system, and establishing a trend of nonlinear properties in the 2-3 plane related to the 1-3 plane. Such a trend has yet to be investigated for other composite material systems.

Appendix A

Implementation of a Nonlinear Constitutive Model in UMAT

The material constitutive model considered in this work for characterization of IM7/8552 carbon/epoxy composite material is derived in the framework of elasticity. Elastic stress-strain relations for linear orthotropic material are modified to account for shear nonlinearity. Without restricting generality of the stress-strain response formulations, this work follows nonlinear shear stress-strain relations in a form of log-linear, Ramberg-Osgood type equations [A.1] with three material parameters (*G,K,n):*

$$\gamma_{ij} = \frac{\tau_{ij}}{G_{ij}} + \left(\frac{\tau_{ij}}{K_{ij}}\right)^{\frac{1}{n_{ij}}} \qquad 23$$

where γ_{ij} is the shear strain, τ_{ij} is the shear stress, G_{ij} is the linear shear modulus, and K_{ij}, n_{ij} are the secant-intercept modulus and the exponent material constants characterizing the shear nonlinearity in the composite material. The subscript ij is representative of the principal material plane of interest, namely 12, 13, or 23.

Nonlinear shear stress-strain relations are assigned for all three principal material planes for IM7/8552 and the constitutive model can be expressed as follows:

$$\begin{bmatrix} \varepsilon_{11} \\ \varepsilon_{22} \\ \varepsilon_{33} \end{bmatrix} = \begin{bmatrix} \frac{1}{E_{11}} & Symmetric & \\ \frac{-\upsilon_{12}}{E_{11}} & \frac{1}{E_{22}} & \\ \frac{-\upsilon_{13}}{E_{11}} & \frac{-\upsilon_{23}}{E_{22}} & \frac{1}{E_{33}} \end{bmatrix} \begin{bmatrix} \sigma_{11} \\ \sigma_{22} \\ \sigma_{33} \end{bmatrix}$$

$$\begin{aligned} \gamma_{12} &= \frac{\tau_{12}}{G_{12}} + \left(\frac{\tau_{12}}{K_{12}}\right)^{\frac{1}{n_{12}}} \\ \gamma_{13} &= \frac{\tau_{13}}{G_{13}} + \left(\frac{\tau_{13}}{K_{13}}\right)^{\frac{1}{n_{13}}} \\ \gamma_{23} &= \frac{\tau_{23}}{G_{23}} + \left(\frac{\tau_{23}}{K_{23}}\right)^{\frac{1}{n_{23}}} \end{aligned} \qquad 24$$

with the fiber direction denoted as 1 (zero-degree), the in-ply transverse direction as 2 (90-degree), and the laminate-thickness direction as 3 (the interlaminar principal material direction).

In the commercially available finite element analysis software ABAQUS [54] a user-defined subroutine, UMAT, can be used when the built-in material models fail to accurately describe the material behavior.

The UMAT provides the Jacobian (sensitivity) matrix, $\left[\frac{\partial \Delta\sigma_{ij}}{\partial \Delta\varepsilon_{ij}}\right]$, for the constitutive model and updates the stresses at the end of the time increment, $t + \Delta t$.

Equation (24) for the 3D material model, including the Ramberg-Osgood model of nonlinear shear, can be condensed into the following notation. The first term describes the linear elastic material behavior and the second term describes the nonlinear shear behavior.

$$
\begin{Bmatrix}\varepsilon_{11}\\ \varepsilon_{22}\\ \varepsilon_{33}\\ \gamma_{12}\\ \gamma_{13}\\ \gamma_{23}\end{Bmatrix} = \begin{bmatrix} \frac{1}{E_{11}} & \frac{-v_{12}}{E_{11}} & \frac{-v_{13}}{E_{11}} & 0 & 0 & 0\\ & \frac{1}{E_{22}} & \frac{-v_{23}}{E_{22}} & 0 & 0 & 0\\ & & \frac{1}{E_{33}} & 0 & 0 & 0\\ & & & \frac{1}{G_{12}} & 0 & 0\\ & & & & \frac{1}{G_{13}} & 0\\ & \mathit{Symmetric} & & & & \frac{1}{G_{23}}\end{bmatrix} \begin{Bmatrix}\sigma_{11}\\ \sigma_{22}\\ \sigma_{33}\\ \tau_{12}\\ \tau_{13}\\ \tau_{23}\end{Bmatrix}
$$

$$
+ \begin{bmatrix} 0 & 0 & 0 & 0 & 0 & 0\\ & 0 & 0 & 0 & 0 & 0\\ & & 0 & 0 & 0 & 0\\ & & & \frac{1}{K_{12}}\left(\frac{\tau_{12}}{K_{12}}\right)^{\frac{1}{n_{12}}-1} & 0 & 0\\ & & & & \frac{1}{K_{13}}\left(\frac{\tau_{13}}{K_{13}}\right)^{\frac{1}{n_{13}}-1} & 0\\ & & & & & \frac{1}{K_{23}}\left(\frac{\tau_{23}}{K_{23}}\right)^{\frac{1}{n_{23}}-1}\end{bmatrix} \begin{Bmatrix}\sigma_{11}\\ \sigma_{22}\\ \sigma_{33}\\ \tau_{12}\\ \tau_{13}\\ \tau_{23}\end{Bmatrix} \qquad 25
$$

In order to derive the Jacobian matrix, we first obtain the incremental constitutive equation by differentiating equation (25).

$$\begin{Bmatrix} \Delta\varepsilon_{11} \\ \Delta\varepsilon_{22} \\ \Delta\varepsilon_{33} \\ \Delta\gamma_{12} \\ \Delta\gamma_{13} \\ \Delta\gamma_{23} \end{Bmatrix} = \begin{bmatrix} \frac{1}{E_{11}} & \frac{-\upsilon_{12}}{E_{11}} & \frac{-\upsilon_{13}}{E_{11}} & 0 & 0 & 0 \\ & \frac{1}{E_{22}} & \frac{-\upsilon_{23}}{E_{22}} & 0 & 0 & 0 \\ & & \frac{1}{E_{33}} & 0 & 0 & 0 \\ & & & \frac{1}{G_{12}} & 0 & 0 \\ & & & & \frac{1}{G_{13}} & 0 \\ & Symmetric & & & & \frac{1}{G_{23}} \end{bmatrix} \begin{Bmatrix} \Delta\sigma_{11} \\ \Delta\sigma_{22} \\ \Delta\sigma_{33} \\ \Delta\tau_{12} \\ \Delta\tau_{13} \\ \Delta\tau_{23} \end{Bmatrix}$$

$$+ \begin{bmatrix} 0 & 0 & 0 & 0 & 0 & 0 \\ & 0 & 0 & 0 & 0 & 0 \\ & & 0 & 0 & 0 & 0 \\ & & & \frac{1}{n_{12}}\frac{1}{K_{12}}\left(\frac{\tau_{12}}{K_{12}}\right)^{\frac{1}{n_{12}}-1} & 0 & 0 \\ & & & & \frac{1}{n_{13}}\frac{1}{K_{13}}\left(\frac{\tau_{13}}{K_{13}}\right)^{\frac{1}{n_{13}}-1} & 0 \\ & & & & & \frac{1}{n_{23}}\frac{1}{K_{23}}\left(\frac{\tau_{23}}{K_{23}}\right)^{\frac{1}{n_{23}}-1} \end{bmatrix} \begin{Bmatrix} \Delta\sigma_{11} \\ \Delta\sigma_{22} \\ \Delta\sigma_{33} \\ \Delta\tau_{12} \\ \Delta\tau_{13} \\ \Delta\tau_{23} \end{Bmatrix} \qquad 26$$

Inverting the equation (26) gives the Jacobian Matrix:

$$[J] = \begin{bmatrix} \frac{E_{11}{}^2(E_{22} - E_{33}v_{23}{}^2)}{\Theta} & \frac{E_{11}E_{22}(E_{22}v_{12} + E_{33}v_{12}v_{23})}{\Theta} & \frac{E_{11}E_{22}E_{33}(v_{13} + v_{12}v_{23})}{\Theta} & 0 & 0 & 0 \\ & \frac{E_{22}{}^2(E_{11} - E_{33}v_{13}{}^2)}{\Theta} & \frac{E_{22}E_{33}(E_{22}v_{12}v_{13} + E_{11}v_{23})}{\Theta} & 0 & 0 & 0 \\ & & \frac{E_{22}E_{33}(E_{11} - E_{22}v_{12}{}^2)}{\Theta} & 0 & 0 & 0 \\ & & & \frac{G_{12}}{1 + \frac{G_{12}}{n_{12}}\left(\frac{\tau_{12}}{K_{12}}\right)^{\frac{1}{n_{12}}-1}} & 0 & 0 \\ & & & & \frac{G_{13}}{1 + \frac{G_{13}}{n_{13}}\left(\frac{\tau_{13}}{K_{13}}\right)^{\frac{1}{n_{13}}-1}} & 0 \\ & Symmetric & & & & \frac{G_{23}}{1 + \frac{G_{23}}{n_{23}}\left(\frac{\tau_{23}}{K_{23}}\right)^{\frac{1}{n_{23}}-1}} \end{bmatrix} \tag{27}$$

where

$$\Theta = E_{11}\left(E_{22} - E_{33}v_{23}{}^2\right) - E_{22}\left(E_{22}v_{12}{}^2 + E_{33}v_{13}(v_{13} + 2v_{12}v_{23})\right)$$

References

1. Davila, C.G., Camanho, P.P, and Rose, C.A. (2005) Failure Criteria for FRP Laminates. *Journal of Composite Materials.,* 39 (4), 323-345.
2. Makeev, A. and, Nikishkov, Y. (2011) Fatigue Life Assessment for Composite Structures. ICAF 2011 Structural Integrity Influence of Efficiency and Green imperatives. Komorowski, J., editor; New York: Springer; 119-135.
3. Makeev, A., He, Y., Shonkwiler, B., Lee, E., Schreier, H., and Nikishkov, Y. (2011) A Method for Measurement of Three-Dimensional Constitutive Properties for Composite Materials. 18th International Conference on Composite Materials, Jeju, Korea, August 21-26, 2011..
4. MIL-HDBK-17-1F. (2002) Composite Materials Handbook, Vol 1. Polymer Matrix Composites Guidelines for Characterization of Structural Materials. U.S. Department of Defense.
5. Makeev, A., Ignatius, C., He, Y., Shonkwiler, B. (2009) A Test Method for Assessment of Shear Properties for Thick Composites, *Journal of Composite Materials.* 43 (25), 3091-3105.
6. Dobyns, A., Rousseau, C. Q., and Minguet, P. (2000) Helicopter applications and design. In: Kelly, A., and Zweben C., eds.

Comprehensive composite materials. Design and applications, Vol. 6. Amsterdam: Elsevier, 223–242.

7. Puck, A. and Schürmann, H. (1998) Failure Analysis of FRP Laminates by Means of Physically Based Phenomenological Models. *Composites Science and Technology.* 58, 1045-1067.
8. Cui, W.C. and Wisnom, M.R. (1992) Contact Finite Element Analysis of Three- and Four-Point Short-Beam Bending of Unidirectional Composites. *Composites Science andTechnology.* 45, 323-334.
9. He, Y. and Makeev, A. (2014) Nonlinear Shear Behavior and Interlaminar Shear Strength of Unidirectional Polymer-Matrix Composites: A Numerical Study. *International Journal of Solids and Structures.* 51 (6), 1263-1273.
10. Jones, R. and Morgan, H. (1977) Analysis of Nonlinear Stress-Strain Behavior of Fiber-Reinforced Composite Materials. *AIAA Journal.* 15 (12), 1669-1676.
11. Camanho, P.P. *et al*. (2006) Prediction of In Situ Strengths and Matrix Cracking in Composites Under Transverse Tension and In-Plane Shear. *Composites: Part A,* 37, 165-176.

12. He, Y. (2010) Matrix-Dominated Constitutive Laws for Composite Materials. *PhD Dissertation,* Georgia Institute of Technology, U.S.A.

13. Makeev, A., Seon, G., and Lee, E. (2010) Failure Predictions for Carbon/Epoxy Tape Laminates with Wavy Plies. *Journal of Composite Materials.* 44 (1), 95-112.

14. Sutton, M.A., Orteu, J.J., and Schreier, H.W. (2009) Image Correlation for Shape, Motion and Deformation Measurements. New York: Springer.

15. Totry, E., Molina-Aldareguía, J., González, C., and LLorca, J. (2010) Effect of Fiber, Matrix and Interface Properties on the In-Plane Shear Deformation of Carbon-Fiber Reinforced Composites. *Composites Science and Technology.* 70, 970-980.

16. Makeev, A., He, Y., Carpentier, P., Shonkwiler, B. (2012) A Method for Measurement of Multiple Constitutive Properties for Composite Materials. *Composites: Part A.* 43 (12), 2199–2210.

17. ASTM Standard D 2344/D2344M. (2006) Standard Test Method for Short-Beam Strength of Polymer Matrix Composite Materials and Their Laminates. *ASTM International*.

18. Makeev, A., Carpentier, P., and Shonkwiler, B. (2014) Methods to Measure Interlaminar Tensile Modulus of Composites, *Composites: Part A*, 56, 256-261.

19. Makeev, A., Seon, G., Cline, J., and Shonkwiler, B. (2014) In Quest of Methods for Measuring 3D Mechanical Properties of Composites, *Composites Science and Technology.* 100, 105-112.

20. Makeev, A., He, Y., and Schreier, H. (2013) Short-Beam Shear Method for Assessment of Stress-Strain Curves for Fiber-Reinforced Polymer-Matrix Composite Materials. *Strain*, 49, 440-450.

21. Makeev, A., Nikishkov, Y., Seon, G., and Armanios E. (2013) Methods for Assessing Interlaminar Tensile Properties in Composite Materials. In: Proceedings of American Society for Composites 28th technical conference, State College, PA, September 9-11, 2013.

22. Wisnom, M.R. (1994) Modeling of Stable and Unstable Fracture of Short Beam Shear Specimens. *Composites.* 25, 394-400.

23. Xie, M. and Adams, D.F. (1994) Contact Finite Element Modeling of the Short Beam Test for Composite Materials. *Computers and Structures.* 57 (2), 183-191.

24. Xie, M. and Adams, D.F. (1995) Study of Three- and Four-Point Shear Testing of Unidirectional Composite Materials. *Composites.* 26, 653-659.

25. Cui, W.C., Wisnom, M.R. and Jones, M. (1992) Failure Mechanisms in Three and Four Point Short Beam Bending Tests of Unidirectional Glass/Epoxy. *Journal of Strain Analysis.* 27, 235-243.

26. Cui, W.C. and Wisnom. M.R. (1992) Contact Finite Element Analysis of Three- and Four-Point Short-Beam Bending of Unidirectional composites. *Composites Science and Technology.* 45, 323-334.

27. Cui, W.C., Wisnom, M.R., and Jones, M. (1994) Effect of Specimen Size on Interlaminar Shear Strength of Unidirectional Carbon Fibre-Epoxy. *Composites Engineering.* 4, 39-307.

28. ASTM Standard D 5379/D 5379M. (2005) Standard Test Method for Shear Properties of Composite Materials by the V-Notched Beam Method. *ASTM International*.

29. VIC-3D Digital Image Correlation Version 7.2.4. *Correlated Solutions.* 2014.

30. Ramberg, W.A. and Osgood, W.R. (1943) Description of Stress-Strain Curves by Three Parameters. *National Advisory Committee for Aeronautics.* Technical Note No. 902, July.

31. He Y., Makeev, A., and Shonkwiler, B. (2012) Characterization of Nonlinear Shear Properties for Composite Materials Using Digital Image Correlation and Finite Element Analysis. *Composites Science and Technology.* 73 (1), 64–71.

32. Makeev, A. (2013) Interlaminar Shear Fatigue Behavior of Glass/Epoxy and Carbon/Epoxy Composites. *Composites Science and Technology.* 80, 93–100.

33. Carpentier, P., Makeev, A., Liu, L., and Shonkwiler, B. (2016) An Improved Short-Beam Method for Measuring Multiple Constitutive Properties for Composites. *Journal of Testing And Evaluation.* 44 (1), 1-12.

34. ASTM Standard D3044-76. (2011) Standard Test Method for Shear Modulus of Wood-Based Structural Panels. *ASTM International.*

35. ISO 15310. (1999) Fibre-Reinforced Plastic Composites – Determination of the In-Plane Shear Modulus by the Plate Twist Method. International Organization for Standardization, Geneva, Switzerland.

36. Yoshihara, H. (2012) Shear Modulus and Shear Strength Evaluation of Solid Wood by a Modified ISO 15310 Square-Plate Twist Method. *Drvna Industrija.* 63 (1), 51-55.

37. Tsai, S.W. (1965) Experimental Determination of the Elastic Behavior of Orthotropic Plates. *Journal off Engineering for Industry*. 315-318.

38. Hennessey, J.M., Whitney, J.M., and Riley, M.B. (1965) Experimental Methods for Determining Shear Modulus of Fiber-Reinforced Composite Materials. *AFML-TR-65-42,* AFML R&T Div, AF Systems Command, WPAFB, OH, Sept. 1965.

39. Sims, G.D., Nimmo, W., Johnson, A.F. and Ferriss, D.H. (1994) Analysis of Plate-Twist Test for In-Plane Shear Modulus of Composite Materials. *NPL Report DMM(A)54*,* National Physical Laboratory.

40. Broughton, W.R., Nimmo, W., and Sims, G.D. (1994) Plate Twist and V-Notched Beam – Complementary Test Methods for Shear Properties. European Conference on Composites Testing and Standardization. Hamburg, Germany, 341-349.

41. Morais, A.B., Cardoso, C.M., and Pereira, A.B. (2013) Evaluation of In-Plane Ply Shear Properties from Unidirectional Plate Torsion Tests. *Composites: Part A*. 53 (13), 2199–2210

42. Avilés, F. et al. (2011) Experimental Determination of Torsion and Shear Properties of Sandwich Panels and Laminated Composites by the Plate Twist Test. *Composite Structures.* 93, 1923-1928.

43. Farshad, M., and Flüeler, P. (1998) Investigation of Mode III Fracture Toughness Using an Anti-Clastic Plate Bending Method. *Engineering Fracture Mechanics.* 60 (5-6), 597-603.

44. Gommers, B., Verpoest, I., and Van Houtte, P. (1996) Further Developments in Testing and Analysis of the Plate Twist Test for In-Plane Shear Modulus Measurements. *Composites: Part A.* 27A, 1085-1087.

45. Bonnet, M. and Constantinescu, A. (2005) Inverse Problems in Elasticity. *Inverse Problems.* 21**,**1-50.

46. Grediac, M. (2004) The Use of Full-Field Measurement Methods in Composite Material Characterization: Interest and Limitations, *Composites: Part A.* 35 (7), 751-751.

47. Avril, S., et al. (2008) Overview of Identification Methods of Mechanical Parameters Based on Full-Field Measurements, *Experimental Mechanics.* 48, 381-402.

48. Genovese, K., Lamberti, L., and Pappalettere, C. (2004) A New Hybrid Technique for In-Plane Characterization of Orthotropic Materials, *Experimental Mechanics.* 44 (6), 584-592.

49. Molimard, J., Le Riche, R., Vautrin, A., and Lee, J.R. (2005) Identification of the Four Orthotropic Plate Stiffnesses Using a Single Open-Hole Tensile Test. *Experimental Mechanics.* 45 (5), 404-411.

50. Lecompte, D., Smits, A., Sol, H., Vantomme, J., and Van Hemelrijck, D. (2007) Mixed Numerical-Experimental Technique for Orthotropic Parameter Identification Using Biaxial Tensile Tests on Cruciform Specimens. *International Journal of Solids & Structures.* 44 (5), 1643-1656.

51. Chalal, H., et al. (2006) Experimental Identification of a Nonlinear Model for Composites Using the Grid Technique Coupled to the Virtual Fields Method. *Composites: Part A.* 37, 315-325.

52. Avril, A. and Pierron, F. (2007) General Framework for the Identification of Constitutive Parameters from Full Field Measurement in Linear Elasticity. *International Journal of Solids and Structures.* 44, 4978-5002.

53. http://www.hexcel.com/Resources/DataSheets/Prepreg-Data-Sheets/8552_us.pdf.

54. ABAQUS® version 6.11. Analysis User's Manual. Providence: Dassault Systèmes Simulia Corp.

55. Seon, G., Makeev, A., Cline, J. and Shonkwiler, B. (2015) Assessing 3D Shear Stress-Strain Properties of Composites Using Digital Image Correlation and Finite Element Analysis Based Optimization. *Composites Science and Technology.* (Forthcoming) Doi: 10.1016/j.compscitech.2015.07.011.

56. Seon, G., Makeev, A., Cline, J. and Armanios, E. (2015) Assessing 3D Mechanical Properties of Composites Based on Digital Image Correlation. Proceedings of the 20th International Conference on Composite Materials. Copenhagen, Denmark, July 19-24, 2015.

57. Marquardt, D.W. (1963) An Algorithm for Least-Squares Estimation of Nonlinear Parameters, *Journal of Society for Industrial & Applied Mathematics.* 11(2), 431-441.

58. https://www.python.org/

59. http://www.scipy.org/

60. Seon, G., Nikishkov, Y., and Makeev, A. (2015) Structures Perspective for Strength and Fatigue Prognosis in Composites with Manufacturing Irregularities. *Journal of the American Helicopter Society.* 60 (1), 1-10.

61. Hahn, H.T. and Tsai, S.W. (1973) Nonlinear Elastic Behavior of Unidirectional Composite Laminae. *Journal of Composite Materials.* 7, 102-118.

62. Cui, W.C., Wisnom, M.R. and Jones, M. (1992) Failure Mechanisms in Three and Four Point Short Beam Bending Tests of Unidirectional Glass/Epoxy. *Journal of Strain Analysis.* 27, 235-243.

63. Camanho, P. et al. (2006) Prediction of In Situ Strengths and Matrix Cracking in Composites Under Transverse Tension and In-Plane Shear. *Composites: Part: A.* 37, 165-176.

Biographical Information

Julia graduated with honors from Harry Ainlay Composite High School (Edmonton, Canada) in June 2004 with International Baccalaureate certificates in History, French and Mathematics. She received the Alexander Rutherford Scholarship and the University of Alberta Academic Excellence Scholarship for her achievements.

Julia began her undergraduate career at the University of Alberta in the September 2004, where she was a member of Kappa Alpha Theta Women's Fraternity. She graduated with a Bachelor of Science degree specializing in Astrophysics in June 2008. After graduation, she moved to Texas to pursue her graduate studies in Aerospace Engineering at The University of Texas at Arlington. She earned a Master of Science degree in August 2011 and continued her studies in pursuit of a doctoral degree.

She began working with Dr. Andrew Makeev at the Advanced Materials and Structures Laboratory in April 2013 in the area of composite materials characterization. In the spring of 2015, Julia received the Office of Graduate Studies Dissertation Writing Fellowship.